



**National Library
of Canada**

**Bibliothèque nationale
du Canada**

Canadian Theses Service

Service des thèses canadiennes

**Ottawa, Canada
K1A 0N4**

NOTICE

The quality of this microform is heavily dependent upon the quality of the original thesis submitted for microfilming. Every effort has been made to ensure the highest quality of reproduction possible.

If pages are missing, contact the university which granted the degree.

Some pages may have indistinct print especially if the original pages were typed with a poor typewriter ribbon or if the university sent us an inferior photocopy.

Reproduction in full or in part of this microform is governed by the Canadian Copyright Act, R.S.C. 1970, c. C-30, and subsequent amendments.

AVIS

La qualité de cette microforme dépend grandement de la qualité de la thèse soumise au microfilmage. Nous avons tout fait pour assurer une qualité supérieure de reproduction.

S'il manque des pages, veuillez communiquer avec l'université qui a conféré le grade.

La qualité d'impression de certaines pages peut laisser à désirer, surtout si les pages originales ont été dactylographiées à l'aide d'un ruban usé ou si l'université nous a fait parvenir une photocopie de qualité inférieure.

La reproduction, même partielle, de cette microforme est soumise à la Loi canadienne sur le droit d'auteur, SRC 1970, c. C-30, et ses amendements subséquents.

UNIVERSITY OF ALBERTA

SEISMIC WAVE PROPAGATION IN VERTICALLY INHOMOGENEOUS
AND ANELASTIC MEDIA

by

LAWRENCE HUAN TRONG LE

A THESIS

SUBMITTED TO THE FACULTY OF GRADUATE STUDIES AND RESEARCH
IN PARTIAL FULFILLMENT OF THE REQUIREMENTS FOR THE DEGREE
OF DOCTOR OF PHILOSOPHY
IN
GEOPHYSICS

DEPARTMENT OF PHYSICS

EDMONTON, ALBERTA

Spring 1991



**National Library
of Canada**

**Bibliothèque nationale
du Canada**

Canadian Theses Service Service des thèses canadiennes

**Ottawa, Canada
K1A 0N4**

The author has granted an irrevocable non-exclusive licence allowing the National Library of Canada to reproduce, loan, distribute or sell copies of his/her thesis by any means and in any form or format, making this thesis available to interested persons.

The author retains ownership of the copyright in his/her thesis. Neither the thesis nor substantial extracts from it may be printed or otherwise reproduced without his/her permission.

L'auteur a accordé une licence irrévocable et non exclusive permettant à la Bibliothèque nationale du Canada de reproduire, prêter, distribuer ou vendre des copies de sa thèse de quelque manière et sous quelque forme que ce soit pour mettre des exemplaires de cette thèse à la disposition des personnes intéressées.

L'auteur conserve la propriété du droit d'auteur qui protège sa thèse. Ni la thèse ni des extraits substantiels de celle-ci ne doivent être imprimés ou autrement reproduits sans son autorisation.

ISBN 0-315-66798-2

UNIVERSITY OF ALBERTA
RELEASE FORM

NAME OF AUTHOR Lawrence Huan Trong Le
TITLE OF THESIS SEISMIC WAVE PROPAGATION IN VERTICALLY
 INHOMOGENEOUS AND ANELASTIC MEDIA

DEGREE FOR WHICH THESIS WAS PRESENTED Doctor of Philosophy
YEAR THIS DEGREE GRANTED Spring 1991

Permission is hereby granted to THE UNIVERSITY OF ALBERTA LIBRARY to reproduce single copies of this thesis and to lend or sell such copies for private, scholarly or scientific research purposes only. The author reserves other publication rights, and neither the thesis nor extensive extracts from it may be printed or otherwise reproduced without the author's written permission.

(SIGNED) 


PERMANENT ADDRESS:

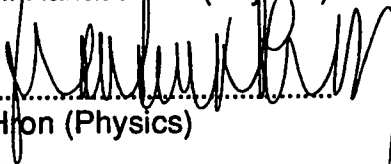
RR2 Portland
Ontario
K0G 1V0

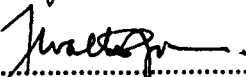
DATED February 11, 1991

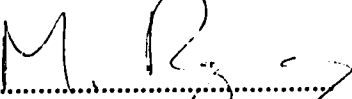
THE UNIVERSITY OF ALBERTA
FACULTY OF GRADUATE STUDIES AND RESEARCH

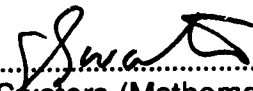
The undersigned certify that they have read, and recommend to the Faculty of Graduate Studies and Research, for acceptance, a thesis entitled SEISMIC WAVE PROPAGATION IN VERTICALLY INHOMOGENEOUS AND ANELASTIC MEDIA submitted by LAWRENCE HUAN TRONG LE in partial fulfillment of the requirements for the degree of DOCTOR OF PHILOSOPHY in GEOPHYSICS.

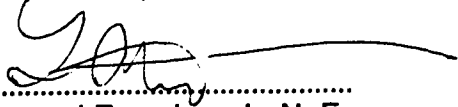

.....
Supervisor
E. R. Kanasevich (Physics)


.....
F. Hon (Physics)


.....
W. Jones (Physics)


.....
M. Razavy (Physics)


.....
G. Swaters (Mathematics)


.....
External Examiner, L. N. Frazer
(Geophysics, University of Hawaii)

Date : January 17, 1991

... Forgetting what is behind and straining toward what is ahead

Philippians 3:13

It is strange to say that there are some significant incidents which left no piece of memory in my mind. My happy childhood and family's depression after my father's death seem no longer to be in reminiscence. In their place, there exists my terrible experience forming a concrete, never-forgotten image inside me. That is my escape.

... Yet there lies ahead of me an inscrutable future. As a stray, I am wandering pointlessly. Nostalgic feeling always fills up my mind.

*from My Escape (Lawrence Le, 1980, Grade 13,
Rideau District High School, Elgin, Ontario)*

Since I came to Canada as a refugee, eleven years have passed by. Many people have thought that I have accomplished a great deal, of course, with lots of struggle and hardships. Indeed, there has been so much blessing. I am very proud that I have done it in a righteous way. However, my accomplishments can not be achieved without the support of many people around me. I fully understood my mother's feeling and sacrifice when she said: 'I don't think we will have a chance to see each other again.' Doris always said to me: 'Le, this is your family and please do come back if you need any help.' Simple words of thanks can not express my gratitude to the Crowe's family. I owe Doris and Marshall so much for their continuous encouragement and support. I am grateful to Jenny and George Neilson for their caring all these years. Also, my wife, Ping, has had so much confidence on me since we first met.

This thesis is dedicated to

my parents and my sisters

who have sacrificed themselves for my way to freedom,

my Canadian parents, Doris and Marshall Crowe,

who have given me a chance for better education

and

my wife, Ping,

who has been standing by me all these years.

ABSTRACT

The basic theory and numerical implementation of P - SV wave propagation in an anelastic layered half-space due to a point P -source is presented using the Fourier-Bessel representation. The formalism allows the inhomogeneity of the medium to take any form along the depth axis with homogeneous discrete layers as a special case. The displacements for a set of receivers located on the free surface are expressed as a linear combination of factors involving the source term and the 2nd order minors governing the contribution of the P - and S -wave type in the inhomogeneous layer. These terms can be obtained by integrating directly the 4th order differential system for P - SV waves and the 6th order differential system for the 2nd order minors using a Runge-Kutta integration method.

Utilizing the Cagniard-de Hoop method, the particle velocity from an impulsive line source for transmitted SH -waves through a boundary separating two homogeneous and solid half-spaces is derived. With a series of examples the properties of the evanescent wave, such as their equivalent ray path and the decay with depth, are displayed.

Computations of two elastic and anelastic half-spaces problem for an SH line source have been performed using an improper ω - k double integral. Attenuation does not radically change the physical picture seen in the elastic case but rather modifies it: there is continuous variation with dispersion and attenuation. For viscoelastic media, the seismograms present features due to the non-planar wavefronts propagating from a line source. Such features cannot be explained by inhomogeneous plane wave theory.

Synthetic results for the case of a layer overlying a half-space compare favorably with computations based on the Cagniard-Pekeris-de Hoop method for a similar case. Numerical sections for four simple models simulating crustal and shallow structures with low velocity and velocity gradient zones show results which conform to those predicted by

ray tracing. Study of the numerical results from the multilayered "Cold Lake" structures indicates that there are significant changes in seismic signatures due to changes in Poisson's ratio. These changes can be detected if far-offset recording is employed.

ACKNOWLEDGEMENTS

This thesis would certainly have been inconceivable without the guidance and suggestions of my advisors, Drs. E. R. Kanasewich and F. Abramovici. Specifically, I would like to thank Dr. E. R. Kanasewich for his suggestions especially in the work on evanescent wave given in Chapters 2 and 3. His excellent knowledge on experimental and practical geophysics has guided me through the steps to analyse the synthetic seismograms. I am very grateful to him for his arrangement of my study with Dr. F. Abramovici and his generous support of my trips to conferences especially my period of stay in the Department of Mathematical Sciences of the Tel Aviv University, Israel.

To Professor F. Abramovici, I owe many thanks. It was my extreme good fortune and privilege to be able to work with him for three and a half years. Most of the work presented in this thesis was a direct collaboration with Professor F. Abramovici. Thank you very much Flavian, for your patience and understanding as a good teacher. You have also introduced me to the field of numerical analysis and applied mathematics. I greatly appreciated the time we have spent together.

This work would not have been completed without the generous financial supports in the form of fellowships from Natural Sciences Research and Engineering Council (4 times), Alberta Oil Sands Technology and Research Authorities (4 times), Graduate fellowships by the University of Alberta (4 times) and Canadian Society of Exploration Geophysicists (4 times). I am grateful to the *Andrew Stewart Graduate Prize* in recognition of my research works.

I would like to thank the Department of Physics for creating a warm atmosphere for my period of stay. My colleague, Sotiris Kapotas is greatly thanked for his excellent knowledge in the *Myrias* computers. Besides, we have been friends and colleagues for seven years. Franco Calacci is appreciated for his advice in various aspects of using the

Myrias. Discussion with NanXun Dai is always a pleasure. Pauly Wong is thanked for her help in displaying the figures in the thesis.

Occasional discussions with Drs. A. Capri, E. Nyland, D. Schmitt and T. Spanos are very helpful. I would like to thank them all. I also thank the committee members for their comments.

Continuous encouragement and support all these years from the Crowe and Neilson's families are immeasurable. I also appreciated the Van's family for their moral support.

Being a student's wife is not easy since due to the nature of the study, I have been away from home for most of the time. I want to extend my gratitude to my wife, *Ping* who has been so understanding and willing to bear the total responsibility of the family during my absence.

TABLE OF CONTENTS

CHAPTER	PAGE
1. INTRODUCTION.....	1
1.1 Ray and Wave Theoretical Approaches in Solving Elastic Wave Propagation Problems	2
1.2 Outline of the Thesis	9
2. THE EVANESCENT WAVE IN CAGNIARD'S PROBLEM FOR A LINE SOURCE GENERATING <i>SH</i>-WAVES	11
2.1 Introduction	11
2.2 Theory	12
2.3 Derivation of the Evanescent Wave Path	22
2.4 Numerical Examples	27
2.5 Conclusion	35
3. THE SOLUTION OF CAGNIARD'S PROBLEM FOR AN <i>SH</i> LINE SOURCE IN ELASTIC AND ANELASTIC MEDIA, CALCULATED USING THE ω-k INTEGRALS	36
3.1 Introduction	36
3.2 The Source Solution	37
3.3 The Solution in Two Half-Spaces	41
3.4 Attenuation	43
3.5 The Numerical Integration	44
3.6 Discussion of Results	48
3.7 Conclusion	52
4. SEISMOGRAMS USING THE ω-k INTEGRALS FOR A POINT <i>P</i>-SOURCE	

IN A VERTICALLY INHOMOGENEOUS ANELASTIC MODEL:	
THEORY AND COMPUTATIONAL ASPECTS	56
4.1 Introduction	56
4.2 The Mathematical Problem and its Formal Solutions	58
4.2.1 The Problem	58
4.2.2 The Solution in Homogeneous Media	63
4.2.3 The Boundary Conditions	65
4.2.4 The Source	66
4.2.5 The Free Surface Conditions and the Solutions	67
4.2.6 The Second-Order Minors	69
4.3 Numerical Considerations And Computational Methods	71
4.3.1 The Theoretical Model	72
4.3.2 The Numerical Integration of the Differential Systems	72
4.3.3 The k -Integral	75
4.3.4 The ω -Integral	78
5. SEISMOGRAMS USING THE ω - k INTEGRALS FOR A POINT P -SOURCE	
IN A VERTICALLY INHOMOGENEOUS ANELASTIC MODEL:	
NUMERICAL RESULTS	79
5.1 The Theoretical Model	79
5.2 The Two-Layered Crustal Model	86
5.3 The Cold Lake Model	90
5.4 Conclusion	110
6. CONCLUDING REMARKS	112
REFERENCES	116

LIST OF FIGURES

Figure		Page
2.1	Geometry of the model.	13
2.2	(a) The path γ traversed by the complex variable ζ in the complex (ζ)-plane. The branch cuts are shaded. (b) The corresponding path Γ traversed by the complex variable τ in the complex (τ)-plane where ζ and τ are related by equation (2.8) in the text. (c) The change of integration path from contour C to one along the positive real semi-axis.	16
2.3	The derivative of a Gaussian time function with $\sigma = 5 \cdot 10^4$ ($f_d = 50$ Hz, $t_d = 0.03$): (a) the time-variation and (b) the amplitude spectrum.	21
2.4	(A) Pressure responses for an acoustic model: $\alpha_1:\alpha_2 = 1.33$, $\rho_1:\rho_2 = 1.2$, receiver depth = 100 m, $x = 500$ m. The source heights z_0 are respectively (a) 1 m, (b) 7.5 m, (c) 30 m above the interface. This result is similar to Figure 4 of Drijkoningen and Chapman (1988); (B) the time derivative of the convolution of the pressure pulses in (A) with the Gaussian source function. The transmitted and evanescent arrivals are denoted as t and e .	28
2.5	(A) Pressure responses for an acoustic model: $\alpha_1:\alpha_2 = 2.0$, $\rho_1:\rho_2 = 2.0$, receiver depth = 100 m, $x = 250$ m. The source heights z_0 are respectively (a) 1 m, (b) 7.5 m, (c) 30 m above the interface. This result is similar to Figure 5 of Drijkoningen and Chapman (1988); (B) the time derivative of the convolution of the pressure pulses in (A) with the Gaussian source function. The transmitted and evanescent arrivals are denoted as t and e .	29
2.6	Synthetic seismograms for a horizontal array of receivers located below the interface for either the two cases depicted in insets (A) and (B). The transmitted and evanescent arrivals are denoted as t and e . For	

- case (A), the velocities are 1 km/s and 2 km/s for the upper and lower half-spaces, respectively; for case (B), the high velocity half-space is above the low velocity one with a reversed source/receivers configuration. The rays show the paths of propagation and energy leakage for the postcritical event in each case. A scale factor S , equal to the basic scale factor \bar{l} for length, was applied to the graph in both cases. 30
- 2.7 (A) The synthetic seismograms of a vertical seismic profile (VSP) for an elastic model. Only seismograms for "odd" receivers are shown. The direct, reflected, head waves, transmitted and evanescent arrivals are, respectively, denoted as d , r , h , t and e ; (B) the model used in (A) with 47 receivers. The source is indicated by a star (*) ; (C) a magnified VSP for the ten traces below the interface. Each of the seismic profiles is magnified by the indicated scale factor. 33
- 2.8 Logarithmic amplitudes of transmitted and evanescent waves versus depth. The results were obtained graphically from enlarged plot similar to 5C with 21 subsurface receivers. The first receiver is at 0.3 m below the interface while the second one is 1 m away from the interface and all the other receivers are located further down at 2 m spacing. The slope of the dashed line having angle ϕ_2 ($\approx 31^\circ$, $f_d = 123$ Hz) with respect to depth axis, is given by $[2\pi(\sin^2\gamma - (\beta_1/\beta_2)^2)^{1/2}]/\lambda_d$ where λ_d is obtained at the peak frequency. The other two limits, ϕ_1 ($\approx 46^\circ$, $f_1 = 208$ Hz) and ϕ_3 ($\approx 15^\circ$, $f_3 = 55$ Hz), are obtained at frequencies with respect to two-thirds of the peak spectral value. Note that the slope for ϕ_3 corresponds to the leakage of the evanescent wave at greater depths (> 30 m). 34
- 3.1 A line source of unit length along the y-axis generating SH -waves and the geometry of the model. 39
- 3.2 The behavior of the integrand P_I given by the expression (3.15) at 5 Hz for the elastic model in Figure 3.4e with the receiver being at the same level as the source. \bar{k} is the dimensionless horizontal wavenumber. 46
- 3.3 A flow-chart of the computer code LA.SHCAG. 47
- 3.4 Comparison of results from two methods: (a) Synthetic seismograms of a vertical seismic profile (VSP) for an elastic structure using the ω - k method.

The direct, reflected, head waves, transmitted and evanescent arrivals are denoted, respectively, as d , r , h , t and e . (b) The same VSP calculated using the Cagniard's method. Profiles (a) and (b) are individually normalized by the biggest absolute amplitude in that profile. (c) Synthetic seismograms of a VSP for an anelastic structure using the ω - k method. The profile is normalized by the same scale factor as obtained in (a). (d) A VSP for the five traces below the interface on plot (c), magnified by a factor of 10. (e) The model used in all calculations.

49

- 3.5 Comparison of results using two methods: (a) Synthetic seismograms for a horizontal array of receivers located below the interface for an elastic structure using the ω - k method. The transmitted and evanescent arrivals are denoted as t and e . (b) The same section calculated using the Cagniard's method. Profiles (a) and (b) are individually normalized by the biggest absolute amplitude in that profile. (c) Synthetic seismograms for the same receiver configuration for an anelastic structure using the ω - k method. The profile is normalized by the same scale factor as obtained in (a). (d) The model used in all calculations.

50

- 3.6 Comparison of results from two methods for an elastic structure: Cagniard (solid line) and ω - k (dashed line). (a) The receiver is in the same half-space as the source ($z_o = -100$ m, $x = 250$ m, $z = -100$ m). (b) The receiver is in the other half-space ($z = 3$ m). The direct, reflected, head waves, transmitted and evanescent arrivals are, respectively, denoted as d , r , h , t and e . (*) denotes the source and (∇) denotes the receiver. The seismogram calculated by the ω - k method is normalized by the same factor of the corresponding seismogram obtained by the Cagniard's method.

51

- 3.7 Comparison of elastic (solid line) and anelastic (dashed line) results. The elastic results are calculated by the Cagniard's method. (a) The receiver is in the same half-space as the source ($z_o = -100$ m, $x = 250$ m, $z = -100$ m) with $Q_1 = Q_2 = 100$. (b) The receiver is in the other half-space ($z = 3$ m) with $Q_1 = Q_2 = 100$. The direct, reflected, head waves, transmitted and evanescent arrivals are, respectively, denoted as d , r , h , t and e . (c) Same as (a) but $Q_1 = Q_2 = 50$; (d) same as (b) but $Q_1 = Q_2 = 50$. (*) and (∇) symbolize the source and the receiver. The seismogram calculated by the ω - k method is normalized by the same scale factor of the

	corresponding seismogram obtained by the Cagniard's method.	53
3.8	Comparison of elastic (solid line) and anelastic (dashed line) results. The elastic results are calculated by the Cagniard's method. (a) The receiver is in the same half-space as the source ($z_o = -100$ m, $x = 250$ m, $z = -100$ m) with $Q_1 = \infty$ and $Q_2 = 50$. (b) The receiver is in the other half-space ($z = 3$ m) with $Q_1 = \infty$ and $Q_2 = 50$. The direct, reflected, head waves, transmitted and evanescent arrivals are, respectively, denoted as d, r, h, t and e . (c) Same as (a) but $Q_1 = 50$ and $Q_2 = \infty$; (d) same as (b) but $Q_1 = 50$ and $Q_2 = \infty$. (*) and (∇) symbolize the source and the receiver. The seismogram calculated by the ω - k method is normalized by the same scale factor of the corresponding seismogram obtained by the Cagniard's method.	54
4.1	The geometry of the model. The source layer is bounded by z_{j+1s} and z_{js}	59
4.2	A flow-chart of the computer code LA.PSVLAYER.	73
4.3	Plots of real part of the reflectivity functions at three different source depths and four different frequencies for the theoretical model. The same source depth is used along the column and the same frequency applies along the row. The arrows point to the location of the real parts of the branch points for the square roots K_α and K_β . The first two are from the P -wave velocities and the last two are from the S -wave velocities.	76
5.1	The triangular pulse with $\Delta = 0.1$: (a) the time-variation and (b) the Fourier counterpart.	80
5.2	Comparison of synthetic seismograms obtained using two different methods: (a) the Cagniard-Pekeris-de Hoop method, (reproduced from the A-paper) (b) the ω - k method. The model is a 1 km-layer overlaying a half-space with $z_j = 0.9H$ and $r = 5H$. The arrows in (b) mark the arrival time of each phase while those in (a) are shifted by Δ .	82
5.3	Comparison of synthetic seismograms obtained using two different methods: (a) the Cagniard-Pekeris-de Hoop method, (reproduced from	

- the A-paper) (b) the ω - k method. The model is a 1 km-layer overlaying a half-space with $z_s = 0.5H$ and $r = 5H$. The arrows in (b) mark the arrival time of each phase while those in (a) are shifted by Δ . 83
- 5.4 Comparison of synthetic seismograms obtained using two different methods: (a) the Cagniard-Pekeris-de Hoop method, (reproduced from the A-paper) (b) the ω - k method. The model is a 1 km-layer overlaying a half-space with $z_s = 0.1H$ and $r = 5H$. The arrows in (b) mark the arrival time of each phase while those in (a) are shifted by Δ . 84
- 5.5 Synthetic displacement sections for a 1 km-layer model. The source is midway in the layer and has a triangular time-function: (a) vertical component and (b) horizontal component. The arrows point to the approximated locations of the indicated phases. The subscript denotes the type multiplicity. 87
- 5.6 Parameter profiles for a two-layered crustal model. σ is the Poisson's ratio. 88
- 5.7 Synthetic velocity sections for a two-layered model. The source acts at 50 m below the surface and has a Gaussian time-variation: (a) vertical component and (b) horizontal component. The arrows mark the approximated arrivals of the indicated phases. The superscript denotes the multiplicity of the ray traversing the layer indicated by the subscript. 89
- 5.8 Two simplified "Cold Lake" models with a low velocity zone: (A) 7 discrete homogeneous layers and (B) 4 layers with a velocity gradient. 93
- 5.9 Plots of the real parts of the reflectivity functions at four different frequencies for (A) 7 discrete homogeneous layers and (B) 146 layers. The arrows point to the location of the real parts of the branch points for the square roots K_α and K_β . The first two are from the P - and S -wave velocities of the half-space and the last two are from the P - and S -wave velocities of the source layer. 94
- 5.10 Plot of real parts of the branch points versus frequency. These are a function of the P -wave velocity in the half-space (line 1), S -wave

	velocity in the half-space (line 2), P -wave velocity within the source layer (line 3) and S -wave velocity within the source layer (line 4). Line 5 delineates the boundary (or upper limit) of the k -integral for results shown in Figure 5.11 and the shaded area denotes the coverage.	95
5.11	Synthetic velocity sections for the 7-layered "Cold Lake" model with Rayleigh wave included. (a) vertical component and (b) horizontal component. The arrows mark the approximated arrivals of the indicated phases. The superscript denotes the multiplicity of the ray traversing the layer indicated by the subscript.	96
5.12	Synthetic velocity sections for the 7-layered "Cold Lake" model with Rayleigh wave excluded. (a) vertical component and (b) horizontal component. The arrows mark the approximated arrivals of the indicated phases. The superscript denotes the multiplicity of the ray traversing the layer indicated by the subscript..	97
5.13	Synthetic velocity sections for the 4-layered "Cold Lake" model with a velocity gradient. (a) vertical component and (b) horizontal component. The arrows mark the approximated arrivals of the indicated phases. The superscript denotes the multiplicity of the ray traversing the layer indicated by the subscript.	99
5.14	Multilayered "Cold Lake" models: (A) an undisturbed model; (B) expanded portion of an undisturbed model; (C) expanded portion of a steam model with a zone of low Poisson's ratio; (D) expanded portion of a condensation model with a zone of high Poisson's ratio. σ is Poisson's ratio, ρ is density and the same Q applies for Q_α and Q_β	100
5.15	Synthetic vertical velocity sections for the multilayered "Cold Lake" models: (A) <i>undisturbed state</i> , (B) <i>steam state</i> and (C) <i>condensation state</i> .	102
5.16	Synthetic horizontal velocity sections for the multilayered "Cold Lake" models: (A) <i>undisturbed state</i> , (B) <i>steam state</i> and (C) <i>condensation state</i> .	103
5.17	Amplitude spectrum of the vertical components for the three traces:	

- the closest, the middle and the farthest in Figure 5.15. (A) *Undisturbed state* , (B) *steam state* , (C) *condensation state* and (D) difference between *steam* and *condensation states*. 105
- 5.18 Amplitude spectrum of the horizontal components for the three traces: the closest, the middle and the farthest in Figure 5.16. (A) *Undisturbed state* , (B) *steam state* , (C) *condensation state* and (D) difference between *steam* and *condensation states*. 106
- 5.19 Vertical sections of differences for the multilayered "Cold Lake" models. Difference between (A) *undisturbed-steam states*, (B) *undisturbed- condensation states* and (C) *steam-condensation states*. The fingers indicate the *steam-zone event* and the *half-space event*. 108
- 5.20 Horizontal sections of differences for the multilayered "Cold Lake" models. Difference between (A) *undisturbed-steam states*, (B) *undisturbed- condensation states* and (C) *steam-condensation states*. The fingers indicate the *steam-zone event* and the *half-space event*. 109

CHAPTER 1

INTRODUCTION

In solid earth geophysics and earthquake engineering, synthetic seismograms are basic tools to predict the kinematic and dynamic properties of elastic waves propagating through the Earth. Improvements in numerical techniques and advances in high speed computers in the past decades have made feasible the computation of theoretical seismograms for realistic models. Starting with the mid-fifties, more and more such seismograms were computed and analysed. The first models were very crude so that comparisons with records were not very successful but later on, especially during the seventies, the calculated seismograms resembled field seismic records, at least in some time-intervals, so that they could serve in the interpretation of the data. However, due to the heterogeneity of the real Earth, no simple analytic solutions of the elastic wave equation exist. Many approximate methods based on geometrical ray theory such as ART (Hron and Kanasewich, 1971), WKBJ theory (Chapman, 1978), to mention a few, are fast, but have limitations in representing a variety of phenomena, notably caustics, attenuation and guided-waves (Foster and Huang, 1990). Fundamentally, most of these methods give incomplete results. Kerner (1990) points out that the full understanding of the complexity in the seismograms can only be achieved through the use of total wave field modeling.

Many numerical schemes such as finite-differences (FD) have been employed to generate seismograms in extremely complicated structures and dispersion relation and stability criterion are difficult to specify except in simple media (Mora, 1990). The results thus produced present various kinds of errors, thus prohibiting a reliable convergence to a valid solution. Analysis of FD schemes also indicate that conservation of energy does not guarantee numerical stability (Mora, 1990). The seismograms are, therefore, trustworthy

only if the limitations of the numerical schemes are well understood. One way to find out these limitations is to check the numerical results obtained by purely numerical algorithms against exact numerical seismograms obtained by numerical computations of analytic solutions. However, analytic solutions or closed form solutions of the elastic wave equations are known only for simple structures such as the ones dealt in this thesis. Nevertheless, the *fundamental* study of these simple models should not be overlooked and should proceed in parallel with the improvement of the purely numerical solutions since from both the practical and theoretical viewpoints their solutions provide us with references and quantitative checks against various approximate and purely numerical methods. From such studies, one may find the conditions under which the numerical methods are valid and understand features, such as evanescent waves, whose solution can not be easily predicted or even obtained by any approximate means. The purpose of the thesis is to provide some exact solutions for the cases where two half-spaces are in welded contact and a half-space is layered.

1.1 Ray and Wave Theoretical Approaches in Solving Elastic Wave Propagation Problems

One of the basic approximations frequently used to simulate the structure of the solid crustal mantle is the *layer-cake model* in which there is an inhomogeneous layer welded on top of a homogeneous half-space. This multilayered model appears to be very simple with no allowance for geoidal curvature, lateral variation of the medium and anisotropy, etc. Synthetic seismograms generated from such a medium have been used successfully to guide the determination of bounds on crustal structures and to interpret actual records of elastic waves for earthquake and artificial sources (Helmberger, 1968; Helmberger and Wiggins, 1971; Fuchs and Müller, 1971; Vered and Ben-Menahem, 1974

and Braile and Smith, 1975). When sphericity of the medium is considered, an earth-flattening transformation can be used to approximately transform the spherical layers into plane layers (Gilbert and Helmberger, 1972; Chapman, 1973 and Müller, 1985). For decades, a substantial amount of research effort has been devoted to finding means to obtain exact solutions to the physical problem of wave propagation in such a medium due to an impulsive disturbance occurring internally or on the free surface. The absence of the computing power and powerful analytical tools has so far restricted the solution to approximate type or models with simple structures which are approximations to the real Earth.

One of the common features of early synthetic seismograms was that they were based not on the double Fourier integral, but were obtained by means of the Laplace transform and its inversion using the so-called Cagniard-Pekeris-de Hoop method. The concept that the double Fourier-Bessel integral cannot lead to a practical way of calculating numerically the disturbance, while the inversion of the Laplace transform can, stressed by Pekeris (1960) in the opening stages of this period, was motivated by the *number-crunching* power of electronic computers. Although this power increased steadily, the scalar computers of the sixties and seventies were indeed inadequate for the task. Nowadays, this concept begins to lose its grip, due to the appearance of vector and parallel machines and an accelerated pace of progress in computer technology. As a result, what seemed impossible thirty years ago becomes manageable today, if not on a routine basis, at least experimentally. For our purposes there are two main theories to compute the complete response of a layered structure due to point source, i.e. *generalized ray theory* (using the Cagniard-Pekeris-de Hoop method) and *full wave theory* (using the ω - k method).

In *generalized ray theory*, there are two approaches as classified by Abramovici and Gal-Ezer (1978): *analytic* and *synthetic*. In the *analytic* approach (Spencer, 1960; Helmberger, 1968 and Gilbert and Helmberger, 1972), each physical ray is represented by

an integral whose integrand consists of a product of generalized plane-wave reflection and transmission coefficients (Spencer, 1960) of the interfaces that the ray encounters and a phase factor accounting for the source and receiver configuration. In the *synthetic* approach, the solution represented by an integral is obtained from the wave equation associated with the assigned boundary conditions. The integral is expressed in closed algebraic form and is then expanded in a series (Abramovici and Gal-Ezer, 1978). In this manner, an individual ray cannot be identified but there is a group of rays of the same type. By using the *synthetic* approach, Pekeris et al. (1965) and Abramovici (1970) managed to obtain the vertical and horizontal displacements due to an explosive point P -source in an elastic one-layered half-space.

In either approach, one has to invert the Laplace transform for the integrals representing the rays or group of rays. The method of inversion was devised almost at the same time by Cagniard (1939 and 1962) and Pekeris (1940). The first treated the case of a point source of P -waves acting causally in a model consisting of two homogeneous half-spaces, while the second considered the case of a point torque-source acting on the surface of a homogeneous half-space. Later on, de Hoop (1958) presented a modified version of the method which is more amenable to numerical evaluations. During the sixties and the seventies, the method was extended to more complicated structures, the extension being based on one of the following versions: Gilbert and Helmberger (1972) and independently Ben-Menahem and Vered (1973) extended the de Hoop's version to a multilayered structure, while a similar extension based on the original Cagniard formulation was presented by Abramovici (1978). The essence of the method involves some legitimate change of variables (thus change of integration contours) so as to bring the integral to a recognized form of a Laplace integral transform over a real path with a Laplace kernel. The integrand besides the kernel is the Green's function of the problem. Recently, Abramovici (1978) gave a generalization of the method for more complex integrals arising from different source types and time-dependence.

However, the computation of the method is prohibitively time-consuming since one has to sum up many rays to have a complete physical picture even though there is a finite sum of rays within a finite time-interval. Usually, rays of small amplitude are neglected to reduce computation time. Another drawback of the theory is the inability to consider absorption by the medium. Helmberger (1973) attempted to incorporate the effects of anelasticity by convolving the solution with an average Q operator being constant for a particular ray characterized by the arrival time. However, for rays with the same arrival time but different ray paths, this is certainly erroneous. Kelamis et al. (1983) made some improvement by Fourier transforming each generalized ray, incorporating absorption in the transformed domain and performing an inverse FFT to the spectrum to give an attenuated ray.

There are phenomena for which the ray interpretation is not adequate. For example, in the ray expansion individual rays have tails of growing amplitude rather than decreasing amplitude (Kelamis et al., 1983). In this case only groups of rays yield a physical solution (Abramovici and Gal-Ezer, 1978; Kelamis et al., 1983). A second example is the occurrence of the evanescent event in both elastic (Abramovici, Le and Kanasewich, 1989) and anelastic media (Abramovici, Le, Kanasewich, 1990). The evanescent wave is better explained by the interaction of the curved wavefront with the boundary (Brekhovskikh, 1980; Richards, 1984). Consequently *full wave* interpretation of the wave equation becomes necessary.

In *full wave theory*, which is the main subject of this thesis, the physical problem is treated as a boundary value problem in which the wave equation is solved in the Fourier transformed domain, i.e the frequency-wavenumber (ω - k) domain or its variant, the frequency-slowness (ω - p) domain. The solution corresponding to a monochromatic plane wave of angular frequency ω with horizontal wavenumber k ($k = \omega p_x$ where p_x is the horizontal slowness) satisfies all the boundary conditions, which consist of the

continuity conditions at the velocity discontinuities of the medium, stress-free condition on the free surface and the source condition at the level of the source. By superposition, the total solution can then be expressed as an improper double integral over ω and k . Given the computer power to perform the integration, the solution gives a *complete response* within a frequency-wavenumber window and the formalism allows a natural implementation of intrinsic attenuation by making the velocities of the medium complex. Usually, the evaluation of the integral can be performed by (1) direct numerical integration of the k -integral and then a FFT inversion of the ω -integral or (2) a combination of the methods of residues and stationary phase. A brief account of some of the published works in this field was given recently by Abramovici (1990) and a complete account would take a full book. The compromise is to turn the reader to an excellent textbook on theoretical seismology such as Aki and Richards (1980).

The first representation of solutions to seismic problems by Fourier integrals was given in a classical paper by Lamb (1904) in which the displacements due to concentrated forces acting on a homogeneous half-space were expressed as a double infinite integral over frequency, ω , and wavenumber, k . This representation can be used for analyzing the solution and the waves related to it, but can also provide numerical evaluations of the disturbance, by approximating the double integrals. Lamb applied both these procedures. Since Lamb's fundamental paper, theoreticians have followed the first of these avenues, extending Lamb's analysis in every possible direction, discovering various types of waves and building new and sophisticated methods to treat them. As these methods were usually related to the physical characteristics of wave propagation in various media, they were able, even with the limited means of the precomputer era, to learn much about the properties of the earth in various regions and even of the earth as a whole.

In work immediately following Lamb, theoretical seismograms were given only for the simple case of a half-space overlaid by a layer. Pekeris (1948) first treated a point

source problem in a layered liquid by reducing the internal k -integral to a sum of normal propagating modes, each being approximated by the saddle-point method. Recently, Panza (1985) employed the modal approach to calculate synthetic seismograms for a multilayered anelastic structure. The normal mode calculation is valid for moderate to long ranges and at lower frequencies. For small ranges, the contribution of the branch-line integrals which are neglected in the normal modal approach are important (Abramovici, 1968a). For a multilayered case, the results were mostly restricted to the dispersion curves calculation by using a Thomson-Haskell propagation matrix approach (Thomson, 1950 and Haskell, 1953). Synthetic seismograms were not obtained routinely until recently by various methods due to the excessive amount of computation time required.

A first attempt at carrying out a direct integration of the improper k -integral was performed by Fuchs (1968) in an original version of the reflectivity method. Later, Fuchs and Müller (1971) extended the method to include transmission losses and time delays due to overburden on top of the reflectivity zone. Previously, Gilbert and Backus (1966) laid down the basic theory for wave propagation in a layered medium of which the Thomson-Haskell based algorithm is a special case. The reflectivity method has now been modified in various matrix formulations based on the Thomson-Haskell algorithm and with different source and receiver structures by Kind (1979 and 1985), Stephen (1977), Wang and Herrmann (1980), Franssens (1983), Kennett (1983), Schmidt and Tango (1986), Mallick and Frazer (1988) and others. Chin et al. (1984) recently summarized and compared some of the matrix methods in a review paper. The intrinsic assumption of the reflectivity formalism lies in its consideration of any vertically inhomogeneous zone as a stack of homogeneous sublayers. For flat and homogeneous media, the method gives exact results. However many thin homogeneous sublayers are usually taken to approximate the inhomogeneous zone as closely as possible. This *homogenization* process is necessary to make use of the Thomson-Haskell algorithm since the eigenfunctions for a homogeneous medium can be determined more easily than for inhomogeneous medium. However, it is

well known that, due to the factors such as compaction of overburden, closure of pore spaces at great depth and chemical alterations, the velocity increases continuously with depth.

To speed up the reflectivity approach, Mallick and Frazer (1987) incorporated inhomogeneous layers using a nonuniform WKBJ formulation. By solving a second order hyperbolic system of elastic wave equation, Alekseev and Mikhailenko (1980) have developed a wavenumber summation approach which combines a finite-difference calculation with a finite Hankel integral transformation. The FD implementation is necessary to simulate the response from the inhomogeneous zone. Kerner (1990) has modified the method by finding a solution to a first-order system of elastodynamic equations and has developed a code which has less numerical dispersion and anisotropy than the Alekseev and Mikhailenko's algorithm (1980) and is claimed to be not sensitive to Poisson's ratio. With the advent of powerful computers, the computation of synthetic seismograms can now be carried out practically by many different methods, each having some approximation in one way or the other. Richards (1979) and Müller (1985) summarized these methods.

Abramovici (1968a and b) reformulated the eigenvalue problem associated with the layered half-space and derived closed form solutions for both displacement and stress components without assuming homogeneity of the layers. For each $(\omega-k)$ pair, the evaluation of the integrand requires integrating directly the governing differential systems using a Runge-Kutta method. For a study of surface waves, this has been considered a much better and more accurate way for obtaining the response from inhomogeneous zones (Takeuchi and Saito, 1972). Unlike the reflectivity method, the theory provides a simpler algorithm without keeping track of the upgoing and downgoing waves. Results using such a numerical integration approach have been presented by Le, Abramovici and Kanasevich (1990a and b).

1.2 Outline of the Thesis

The Thesis consists of six chapters.

In Chapter 1 a brief overview of the ray and wave theoretical approaches in studying wave propagation in layered structures has been given together with the contents of the thesis.

In chapter 2 the transmission term for a *SH*-line source problem with two half-spaces in welded contact (Cagniard's problem) is solved using the Cagniard-de Hoop method. In addition to the arrivals predicted by geometrical acoustics, an evanescent wave shows up as part of the solution. The properties of the evanescent wave are discussed and demonstrated using synthetic sections with horizontal and vertical arrays of receivers.

In Chapter 3 a different solution of the same Cagniard's problem discussed in Chapter 2 is derived using the frequency and wavenumber (ω - k) double integral. Direct numerical integration of the k -integral is performed using Euler's transformation. Anelasticity of the medium is considered and the behavior of the evanescent wave and all the arrivals including incident, head wave, reflected and transmitted waves are studied. Inhomogeneous plane wave theory cannot be used to explain the findings in this chapter since curvature of the wavefront generated by a line source cannot be neglected.

In Chapter 4 the mathematical formulation of wave propagation in a layered anelastic solid half-space due to a point *P*-source is given. In this problem, the displacement-stress vector satisfies the causality property, the discontinuity at the source and the boundary conditions consisting of the vanishing of the stresses on the free surface and the continuity of displacements and stresses on each interface. A system of equations of order 6 is used to partly overcome the order-of-magnitude (stiffness) difficulty. Implementation of the algorithm and numerical evaluation of the Fourier-Bessel integrals is discussed. The rationale used in choosing the numerical parameters such as f_{\max} and the

frequency increment and the use of cosine-tapers in ω - k space are also given.

In Chapter 5 numerical experiments are presented. Synthetic seismograms from a layer over a half-space obtained by the ω - k method and the Cagniard-Pekeris-de Hoop method are compared. A crustal two-layered half-space with large ranges is given to establish the ability of the method in crustal modeling. Shallow exploration models simulating the Cold-Lake area in Alberta with different Poisson's ratio are used to produce synthetic results simulating *pre*- and *post-steam* injection.

Chapter 6 summarizes the work presented in the thesis and concludes the thesis with some remarks on future directions.

CHAPTER 2

THE EVANESCENT WAVE IN CAGNIARD'S PROBLEM FOR A LINE SOURCE GENERATING *SH*-WAVES

2.1 Introduction

The existence of evanescent (otherwise called pseudo-surface or tunneling) waves has long been established both on earthquake records (Oliver and Major, 1960) and in controlled source experiments either in the laboratory (Gilbert and Laster, 1962) or, more recently, in underwater acoustics (Stephen and Bolmer, 1985). The theoretical aspects of evanescent waves generated by a point source in two fluid half-spaces have been given by Brekhovskikh (1980) using an asymptotic approach. For a line source in two fluid half-spaces similar phenomena have been studied by Drijkoningen and Chapman (1988) using the Cagniard-de Hoop method. It is well known that the evanescent waves are distinguishable only under certain conditions related to the physical properties of the structures involved and to the location of source and receiver.

This chapter deals with a structure consisting of two homogeneous and elastic half-spaces in welded contact having, in the upper half-space, an impulsive line source generating *SH*-waves (case 1b of Drijkoningen and Chapman, 1988 and Abramovici, Le and Kanasewich, 1989). Particularly, it is only concerned with the calculation of the particle displacement or velocity for receivers located in the lower half-space since the responses for receivers located in the same half-space as the source have been discussed in standard references like Aki and Richards (1980). The particle velocity for an arbitrary time-variation is obtained by convolving the Green's function with the time-derivative of a delayed Gaussian function of relatively high frequency. Apart from the main transmitted

wave arrival, the evanescent wave shows up in the numerical output.

2.2 Theory

A general procedure presented by Cagniard (1939, 1962) was followed. Let a right-handed Cartesian coordinate system be oriented so that the positive z -axis faces downward (Figure 2.1). Two elastic, homogeneous and isotropic half-spaces, characterized by densities ρ_i and shear moduli μ_i ($i=1,2$) are welded along the (x,y) -plane. A line source generating SH -waves is located along the y -axis at a height $-z_o$ ($z_o > 0$). The problem is two-dimensional in (x,z) and the only displacement component v is in the y -direction, satisfying the inhomogeneous wave equation

$$\rho \frac{\partial^2 v}{\partial t^2} - \mu \nabla^2 v = \delta(x) \delta(z+z_o) f(t) . \quad (2.1)$$

Here $f(t)$ represents the time-variation of the source, measuring the strength of the external body force acting in the y -direction and having the physical dimension of force per unit length. In addition to equation (2.1), the solution v must obey the initial (I.C.) and boundary (B.C.) conditions as follows:

- (I.C.) the displacement, velocity and other physical quantities that depend on time must be zero for $t < 0$ (causality property);
- (B.C.) a. displacement and stress are continuous along the interface,
- b. the radiation condition, i.e., no energy comes from infinity.

Instead of applying Fourier transform to the space-time variables (Drijkoningen and Chapman, 1988), the Laplace transform was used in our approach. The Laplace transform

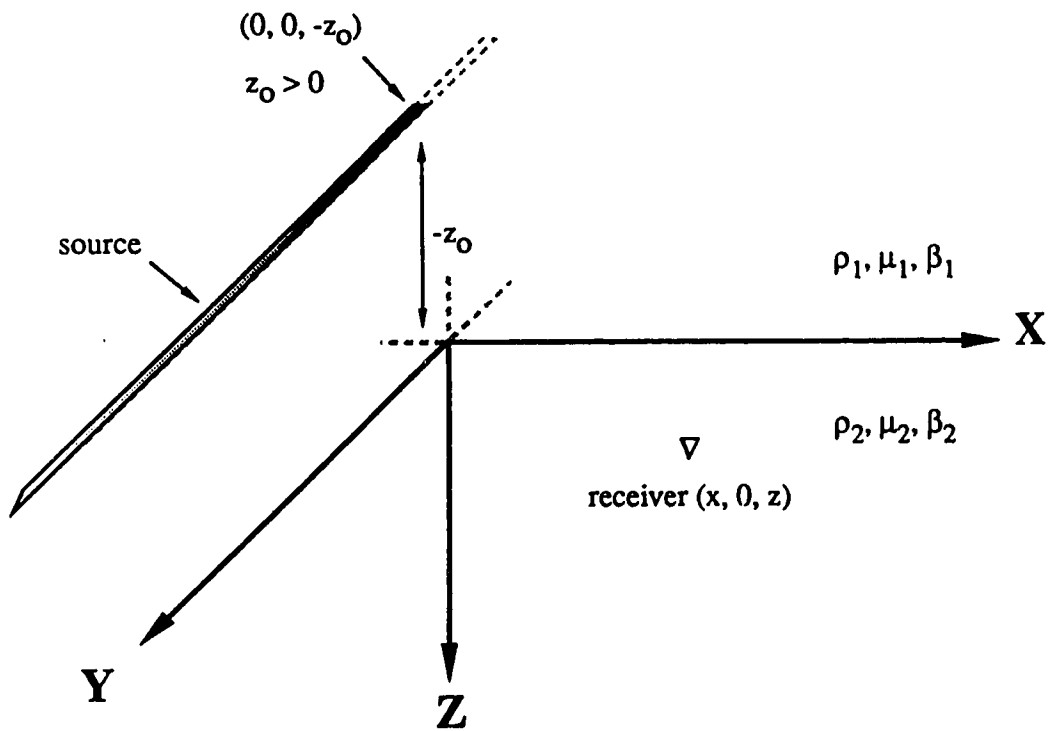


Figure 2.1: Geometry of the model.

$$\bar{v}_t = \int_0^{\infty} v_t(x, z, t) e^{-pt} dt \quad (2.2)$$

of the particle displacement for the transmitted wave that satisfies the transformed wave equation (2.1)

$$\nabla^2 \bar{v}_t - \frac{p^2}{\beta_2^2} \bar{v}_t = 0 \quad (2.3)$$

with the shear wave velocities

$$\beta_i = \sqrt{\frac{\mu_i}{\rho_i}} \quad (i = 1, 2) \quad (2.4)$$

is obtained by taking a bilateral Laplace transform with respect to x of (2.3), coupled with the boundary conditions of the problem and by inverting the result to the space domain (de-Hoop, 1960). The result is

$$\bar{v}_t = \frac{\bar{f}(p)}{2\pi\mu_1} \operatorname{Im} \int_0^{i\infty} \frac{T}{\eta_1} e^{p(\zeta x - \eta_1 z_0 - \eta_2 z)} d\zeta \quad (2.5)$$

where $\operatorname{Im}[\dots]$ and $\operatorname{Re}[\dots]$ denote the imaginary and real part of a complex quantity, $\bar{f}(p)$ is the Laplace transform of the source time function, T is the transmission coefficient

$$T = \frac{2\mu_1\eta_1}{\mu_1\eta_1 + \mu_2\eta_2} \quad (2.6)$$

and

$$\eta_i = \sqrt{\frac{1}{\beta_i^2} - \zeta^2} \quad , \quad \text{Re}(\eta_i) \geq 0 \quad (i = 1, 2). \quad (2.7)$$

The problem is, therefore, to invert (2.5) into the time-domain by bringing the integral to a form which is an obvious Laplace transform, allowing us to read off the original time-function. Such would be the case if the coefficient of p in the exponent was the time-variable and the integration was taken with respect to this variable from 0 to ∞ . In order to have such a case, we consider the formal change of variables

$$\tau = \varphi(\zeta) = -\zeta x + \eta_1 z_o + \eta_2 z \quad . \quad (2.8)$$

It can be shown (see Cagniard, 1939, 1962; Longman, 1961 and Abramovici, 1978) that expression (2.8) is a genuine change of variables, i.e., it is one-to-one, if: (1) the (ζ) -plane is cut in order to define uniquely the square roots η_1 and η_2 , e.g., we take branch cuts along the semi-axes from $1/\beta_2$ and $1/\beta_1$ to infinity going right and from $-1/\beta_2$ and $-1/\beta_1$ to infinity going left respectively (Figure 2.2a); (2) the square roots η_i ($i=1,2$) are defined to have non-negative real parts; (3) the (τ) -plane is cut along the real axis between τ_c given by

$$\tau_c = \frac{x}{\beta_2} + z_o \sqrt{\frac{1}{\beta_1^2} - \frac{1}{\beta_2^2}} \quad (2.9)$$

and $\tau_o = \varphi(\zeta_o)$ (Figure 2.2b), where ζ_o is the real number between $-1/\beta_2$ and $1/\beta_2$ for which φ' is zero. The proof is based on the *argument principle* in complex analysis (Copson, 1960) and is similar to other cases when the Cagniard method is used (Abramovici, 1978).

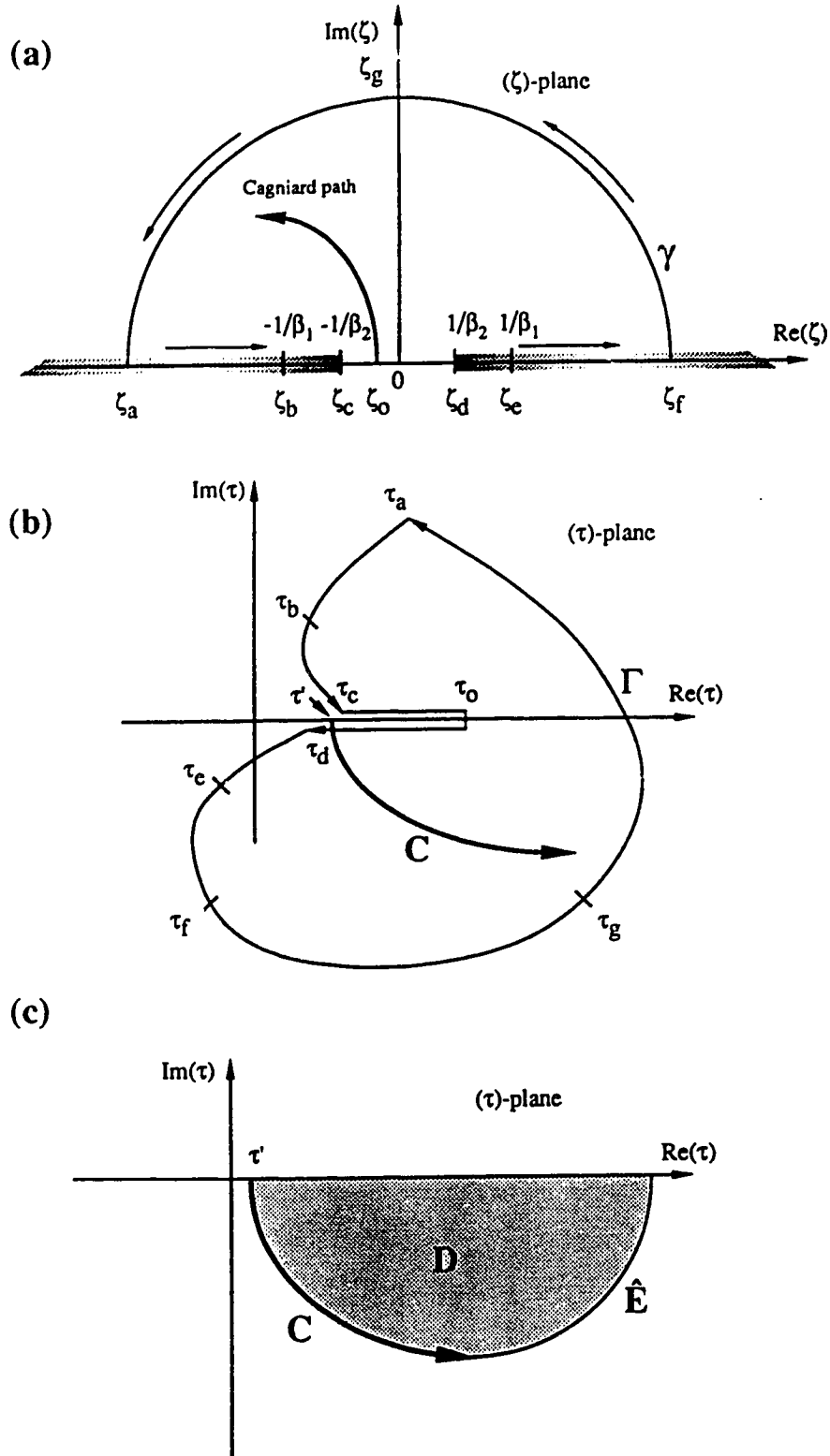


Figure 2.2: (a) The path γ traversed by the complex variable ζ in the complex (ζ) -plane. The branch cuts are shaded; (b) the corresponding path Γ traversed by the complex variable τ in the complex (τ) -plane where ζ and τ are related by equation (2.8) in the text; (c) the change of integration path from contour C to one along the positive real semi-axis.

A brief proof is given that the change of variables τ and ζ related by the expression (2.8) is one-to-one. The case $\beta_1 < \beta_2$ will be treated below since the other case $\beta_1 > \beta_2$ is similar and the result is the same. In order to define the square roots of η_i ($i = 1, 2$) with the non-negative real parts, the cuts are defined in the complex (ζ)-plane to be the real semi-axes running from $1/\beta_2$ to $+\infty$ and from $-1/\beta_2$ to $-\infty$ (see Figure 2.2a). As the point in the complex (ζ)-plane traverses the closed path γ along $\zeta_a \zeta_b \zeta_c \zeta_o 0 \zeta_d \zeta_e \zeta_f \zeta_g \zeta_a$ {along the real axis above the cuts and along the semicircular arc in the upper half-plane [$\text{Im}(\zeta) \geq 0$]}, the corresponding point in the complex (τ)-plane follow the closed path Γ ($\tau_a \tau_b \tau_c \tau_o \tau_d \tau_e \tau_f \tau_g \tau_a$) in Figure 2.2b. The real axis is cut from τ_c to τ_o in order to define the correspondence of the variables one-to-one.

Now we consider the function

$$\tau - \hat{\tau} = -\zeta x + \eta_1 z_o + \eta_2 z - \hat{\tau} \quad (2.10)$$

with $\hat{\tau}$ being any point in the complex (τ)-plane corresponding to ζ ($\zeta = i\zeta_I$) purely imaginary going from 0 to $i\infty$. The image C of the imaginary axis in the (ζ)-plane is located in the fourth quadrant of the (τ)-plane (Figure 2.2c), starts from $\tau' = z_o/\beta_1 + z/\beta_2$ and goes to infinity in the direction given by

$$\tau = \zeta_I [(z_o + z) - ix] \quad (2.11)$$

Obviously, the point in the complex ($\tau - \hat{\tau}$)-plane corresponding to ζ traversing the path γ will move on the path obtained by translating Γ through $\hat{\tau}$. The conclusion is that the argument of $\tau - \hat{\tau}$ changes by exactly 2π when the original variable ζ goes around the path γ once. According to the *argument theorem*, the transformation (2.8) is one-to-one and the integral given by equation (2.5) is then rewritten as

$$\int_C \left\{ \frac{T}{\eta_1} \frac{d\zeta}{d\tau} \right\}_\tau e^{-p\tau} d\tau \quad (2.12)$$

which is a line integral along the contour C . If we connect the contour C with the positive real axis with an arc, say \hat{E} , of large radius (Figure 2.2c), it can be easily shown that the integrand of (2.12) is analytic on and inside the domain D and the integral along \hat{E} does not contribute since the integrand is a rational function and the exponential term vanishes for large τ . Therefore, by the Cauchy theorem, we can change the integration path from C to the positive real axis. Denoting the real part of τ by t and $H(t)$ as the Heaviside step function, we have

$$\bar{v}_t = \frac{\bar{f}(p)}{2\pi\mu_1} \text{Im} \int_0^\infty H \left\{ t - \left(\frac{z_0}{\beta_1} + \frac{z}{\beta_2} \right) \right\} \left\{ \frac{T}{\eta_1} \frac{d\zeta}{d\tau} \right\}_{\tau=t} e^{-pt} dt. \quad (2.13)$$

For $\bar{f}(p) = 1$, i.e., for an impulse as time-function, the inversion into time-domain is read off as

$$v_t = \frac{1}{2\pi\mu_1} H \left\{ t - \left(\frac{z_0}{\beta_1} + \frac{z}{\beta_2} \right) \right\} \text{Im} \left\{ \frac{T}{\eta_1} \frac{d\zeta}{d\tau} \right\}_{\tau=t}. \quad (2.14)$$

The quantity $(z_0/\beta_1 + z/\beta_2)$ represents the minimum possible travel time of a wave traveling vertically from the source to the interface and vertically from the interface to the receiver. A more careful analysis shows, however, that $v_t(x, z, t)$ is zero until the arrival of the so-called transmitted wave at $t = t_0$. More precisely, equation (2.14) can be written as

$$v_t = -\frac{1}{2\pi\mu_1} H(t-t_o) \operatorname{Im} \left\{ \frac{T}{\eta_1} \frac{1}{x + z_o \zeta / \eta_1(\zeta) + z \zeta / \eta_2(\zeta)} \right\}_{\tau=t} \quad (2.15)$$

where ζ is the solution of the implicit equation (2.8) given $\tau = t$ and denotes the Cagniard path in the second quadrant of the (ζ) -plane (Figure 2.2a), for $\tau \geq t_o$. The arrival time t_o of the transmitted wave is given by the expression (2.8) at $\zeta = \zeta_o$ where ζ_o is the negative root of the equation

$$\frac{z_o \zeta_o}{\eta_1(\zeta_o)} + \frac{z \zeta_o}{\eta_2(\zeta_o)} = -x \quad (2.16)$$

The particle velocity \dot{V}_t for an arbitrary time-variation of the source is obtained by taking the time-derivative of the convolution between the source time-function $f(t)$ and the Green's function

$$\dot{V}_t = \int_{t_o}^t \dot{f}(t-\tau) v_t(\tau) d\tau \quad (2.17)$$

where the dot denotes the derivative with respect to the whole argument. We found it convenient to perform a change of variables from τ to ζ using expression (2.8). Upon changing the integration variable, we get

$$\dot{V}_t = \frac{1}{2\pi\mu_1} H(t-t_o) \operatorname{Im} \int_{\zeta_o}^{\zeta(t)} \dot{f}(t-\tau) \frac{T}{\eta_1} d\zeta \quad (2.18)$$

In order to simulate realistic sources that satisfy also the above assumption of

causality, we consider a Gaussian time-variation (Alford et al., 1974) with a small time delay $t_d = (2/\sigma)^{1/2}$:

$$f(t) = H(t) e^{-\sigma(t - t_d)^2} . \quad (2.19)$$

The derivative of this time function (Figure 2.3a) has the frequency-domain representation (Figure 2.3b):

$$\hat{f}(\omega) = i\omega \sqrt{\frac{\pi}{\sigma}} e^{-\omega^2/4\sigma - \omega t_d i} \quad (2.20)$$

and, therefore, the damping parameter σ controls the dominant radian frequency $\omega_d = (2\sigma)^{1/2}$ of this pulse, i.e., the larger σ , the higher the dominant frequency. The energy of this signal is contained mostly in a narrow band around ω_d . For numerical purposes, we restricted $f(t)$ to the interval $(t_d - t_m, t_d + t_m)$ containing the main contribution in the time domain if t_m is chosen conveniently. Thus, if

$$t_m = \sqrt{m \frac{\ln(10)}{\sigma}} , \quad (2.21)$$

the relative height $|f(t)/f(t_d)|$ of the source function drops by m decades outside the mentioned interval, e.g., it is practically zero for $m = 5$. The integration limits of the integral (2.18) are affected by the described restriction as follows: the integral has the lower limit ζ_o only for $t < t_o + t_d + t_m$, whereas for $t \geq t_o + t_d + t_m$, the lower limit is $\zeta = \zeta(t - (t_d + t_m))$ obtained by solving (2.8) with $\tau = t - (t_d + t_m)$; the upper limit is $\zeta = \zeta(t)$ for $t_d < t_m$ and $\zeta = \zeta(t - t_d + t_m)$ for $t_d \geq t_m$.

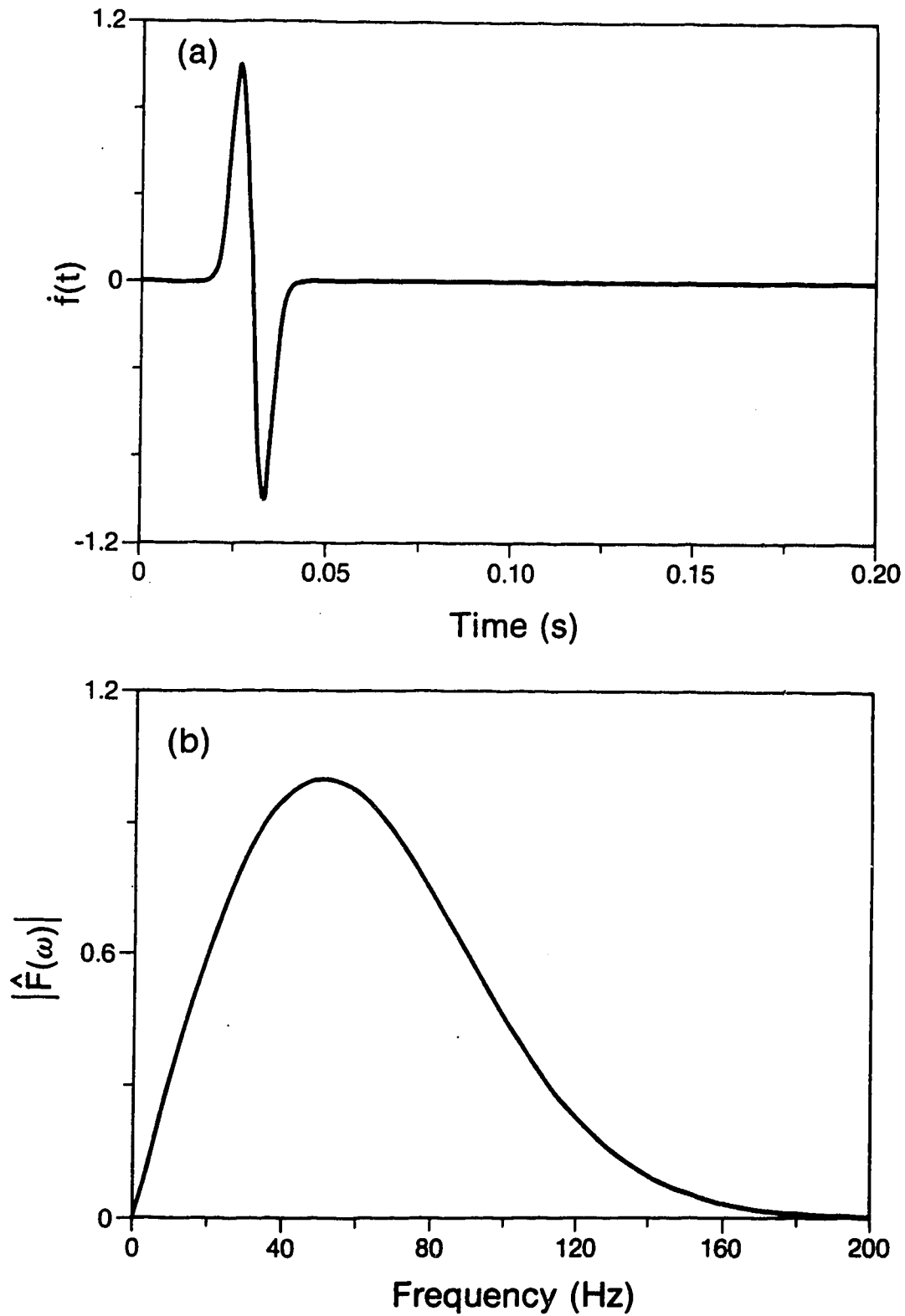


Figure 2.3: The derivative of a Gaussian time function with $\sigma = 5 \cdot 10^4$ ($f_d = 50$ Hz, $t_d = 0.03$): (a) the time-variation and (b) the amplitude spectrum.

2.3 Derivation of the Evanescent Wave Path

The particle velocity for the transmitted wave can be written as a Fourier integral

$$\dot{V}_t(x, z, t) = \frac{1}{4\pi\mu_1} \int_{-\infty}^{\infty} F(\omega) e^{i\omega t} V_t d\omega, \quad (2.22)$$

where $F(\omega)$ is the Fourier transform of the source time function defined by (2.19) and

$$V_t(\omega) = \frac{i\omega}{2\pi} \int_{-\infty}^{\infty} \bar{T} e^{-i\bar{k}x - K_1 z - K_2 z} d\bar{k}, \quad (2.23)$$

$$\bar{T} = \frac{2\mu_1}{\mu_1 K_1 + \mu_2 K_2} \quad \text{and} \quad K_j = \sqrt{\bar{k}^2 - \frac{\omega^2}{\beta_j^2}} \quad (j=1,2). \quad (2.24)$$

We note the similarity between (2.23) and (2.5).

Making further the change of variables

$$\bar{k} = k_1 \sin \theta_1 \quad \text{with} \quad k_1 = \frac{\omega}{\beta_1} \quad (2.25)$$

where θ_1 is the incident angle and allowing the new integration variable θ_1 to take also complex values, which is always the case in Weyl's representation for point sources (Aki and Richards, 1980), we find that (2.25) can be made one-to-one if we split (2.23) into two integrals, one from $-\infty$ to 0 and the other from 0 to ∞ . Denoting $\theta_1 = \theta_1' + i\theta_1''$, we find that for $-\infty < \bar{k} \leq 0$,

$$\theta_1 = \begin{cases} \theta_1' & \text{for } -\frac{\pi}{2} \leq \theta_1' \leq 0 \\ -\frac{\pi}{2} + i\theta_1'' & \text{for } 0 \leq \theta_1'' < \infty \end{cases} \quad (2.26)$$

and for $0 \leq \bar{k} < \infty$

$$\theta_1 = \begin{cases} \theta_1' & \text{for } 0 \leq \theta_1' \leq \frac{\pi}{2} \\ \frac{\pi}{2} - i\theta_1'' & \text{for } 0 \leq \theta_1'' < \infty \end{cases} \quad (2.27)$$

We have also used the following expressions for K_j

$$K_j = ik_j \cos \theta_j \quad (j=1,2) \quad (2.28)$$

with $k_j = \omega/\beta_j$ and the incident angle θ_1 and refracted angle θ_2 are related by Snell's law

$$\frac{\sin \theta_1}{\beta_1} = \frac{\sin \theta_2}{\beta_2} \quad (2.29)$$

As a result, V_r is represented by an integral on θ_1 taken along the contour Γ_1 described by Brekhovskikh (Fig.28-1, p.243, 1980)

$$V_r(\omega) = \frac{ik_1\beta_1}{2\pi} \int_{-\frac{\pi}{2}+i\infty}^{\frac{\pi}{2}-i\infty} \bar{T}(\theta_1) e^{-ik_1(x\sin\theta_1+z\cos\theta_1+nz\cos\theta_2)} \cos\theta_1 d\theta_1 \quad (2.30)$$

where

$$\bar{T}(\theta_1) = - \frac{2 m i}{m \cos \theta_1 + \sqrt{n^2 - \sin^2 \theta_1}} , \quad (2.31)$$

$$m = \frac{\mu_1}{\mu_2} \quad \text{and} \quad n = \frac{\beta_1}{\beta_2} . \quad (2.32)$$

In order to make use of the approximation obtained by Brekhovskikh, it is enough to show that our integral (2.30) has all the essential ingredients of his expression for the refracted wave given in Section 32 of his book. Brekhovskikh did not give all the details of his calculations since he gave them when approximating the refracted and the lateral waves in Sections 28-31. It is easy, however, to see that his expression for the refracted field ψ_1 on p.280 is brought first to the form of an integral along the contour Γ_1 by performing the same steps as those leading from [(26.24) on p.233, Brekhovskikh, 1980] to [(28.2) on p.242, Brekhovskikh, 1980]. Ignoring the $(kr)^{-1}$ term, the result for the refracted wave would be, in Brekhovskikh's notation,

$$\psi_1(\omega) = \frac{1}{m} e^{\frac{i\pi}{4}} \sqrt{\frac{k}{2\pi r}} \int_{-\frac{\pi}{2} + i\infty}^{\frac{\pi}{2} - i\infty} (1+V) \sqrt{\sin \theta} e^{ik(x \sin \theta + z \cos \theta - n z \cos \theta_1)} d\theta . \quad (2.33)$$

Using the expression [(2.17) on p.8, Brekhovskikh, 1980] for V we find that

$$\frac{1}{m} (1+V) = \frac{2 \cos \theta}{m \cos \theta + \sqrt{n^2 - \sin^2 \theta}} . \quad (2.34)$$

Hence (2.30), representing our case and (2.33) representing Brekhovskikh's case can be brought to an "almost" identical form by multiplying (2.33) by

$$C = \sqrt{\frac{2\pi r}{k}} \frac{k\beta_1}{2\pi} e^{-i\frac{\pi}{4}} \frac{m}{\sqrt{\sin\theta}} \quad (2.35)$$

The meaning of "almost" is that Brekhovskikh has an exponent of the form $ik(z_0 \cos\theta - nz \cos\theta_1 + r \sin\theta)$ whereas we have (in his notation), the exponent with the sign reversed: $-ik(z_0 \cos\theta + nz \cos\theta_1 + r \sin\theta)$, the reason being that he considered harmonic waves of the form $\exp(-i\omega t)$ and we have harmonic components of the form $\exp(i\omega t)$. This difference, however, is not an impediment in using his final results, as they are based on the saddle-point approximation and the path of steepest descent: the position of the saddle point is obtained by differentiating the expression in the exponent and equating the result to zero.

The results for our case are obtained, therefore, from Brekhovskikh's expressions on p.281-282 multiplying by the factor (2.35) and with the sign in the exponent reversed (in our notation, i.e., denoting his k by k_1 , his r by x and his angle of incidence β by γ). If γ is less than the critical angle, the motion is approximated by just one term representing the geometrical transmitted ray, but if γ is larger than the critical angle ($\sin\gamma > n$), there is an extra term expressed by a branch-line integral representing the so-called *lateral* wave. If the receiver is located in the same half-space as the source and $n < 1$, this will be the *head* wave, whereas if the receiver is located on the other side of the interface, the *lateral* wave is felt only in the vicinity of the interface as an evanescent wave, appearing to have travelled from the source to the point on the interface directly above the receiver and then penetrated below. According to Brekhovskikh's expression (32.14) on p.282, this evanescent wave is approximated as follows: if $m(\pi/2 - \gamma) < \sqrt{1 - n^2}$,

$$V_t^{(\text{evan.})} \approx A(k_1, \sin\gamma) e^{-ik_1 R_1 - k_1 z \sqrt{\sin^2\gamma - n^2}}$$

$$A(k_1, \sin \gamma) = \sqrt{\frac{2\pi x}{k_1}} \frac{k_1 \beta_1}{\pi R_1} e^{-i\frac{\pi}{4}} \frac{m}{\sqrt{\sin \theta}} \left[\frac{\cos \gamma}{m \cos \gamma + i \sqrt{\sin^2 \gamma - n^2}} + \frac{i m}{k_1 R_1 (n^2 - 1)} \right] \quad (2.36)$$

and if $m(\pi/2 - \gamma) \gg \sqrt{1 - n^2}$, $V_i^{(\text{evan.})}$ is approximated by a similar expansion, with $\frac{2}{k_1 R_1 m^2} \sqrt{1 - n^2} \cos^3 \gamma$ replacing the second term in the brackets defining $A(k_1, \sin \gamma)$. Here $R_1 = \sqrt{x^2 + z_o^2}$. This will be, therefore, an evanescent wave, generated by a ray arriving at the interface at an angle beyond the critical one so that it will be totally reflected back in the upper half-space. Still, this ray generates some disturbance in the lower half-space, but only very near the interface. The path along which the evanescent wave travels is therefore the one implied in Fig.2.6A which is based on Fig.32.2, p.281 of Brekhovskikh's book (see also Fig.1b in Drijkoningen and Chapman, 1988).

For $n > 1$, the contribution of the evanescent wave, based on Brekhovskikh's relation [(32.11) on p.282, 1980], is

$$V_i^{(\text{evan.})} \approx B(k_1, \sin \gamma) e^{-ik_2 R_2 - k_1 z_o \sqrt{n^2 \sin^2 \gamma - 1}}$$

$$B(k_1, \sin \gamma) = \sqrt{\frac{2\pi x}{k_1}} \frac{k_1 \beta_1}{\pi R_2} e^{-i\frac{\pi}{4}} \frac{mn}{\sqrt{\sin \gamma}} \left[\frac{\cos \gamma}{n \cos \gamma + im \sqrt{n^2 \sin^2 \gamma - 1}} + \frac{i}{m(1 - n^2)k_1 R_2} \right] \quad (2.37)$$

where $R_2 = \sqrt{x^2 + z^2}$. The form of the exponential leads to the travel path depicted in Fig.2.6B.

2.4 Numerical Examples

The *SH*-elastic case we have solved is similar to the acoustic case solved by Drijkoningen and Chapman (1988). The basic difference in the result lies in the transmission coefficient defined by equation (2.6). In the elastic case, the transmission coefficient does not have cross terms, i.e., each term either in the numerator or denominator bears the same index; while, in the acoustic case, it has cross terms (Aki and Richards, 1980). Substituting μ by $1/\rho$ in equation (2.6) and β by α in equation (2.7), the acoustic counterpart is obtained, i.e. the transmission coefficient should be $T=2\rho_2\eta_1/(\rho_2\eta_1+\rho_1\eta_2)$ in Drijkoningen and Chapman's paper (1988) in which vertical slowness η replaces their q . Figure 2.4A is the computation of the pressure responses which is similar to their Figure 4 and Figure 2.5A to their Figure 5. The absence of the "kick" at transmitted arrival in their Figure 4b is probably due to the coarse sampling width. Figures 2.4B and 2.5B show the time-derivative of the convolution of the pressure responses with the source wavelet having dominant frequency of 123 Hz ($\sigma=3*10^5$). Hereafter, we use this source wavelet to generate synthetic seismograms. Even though the onset of the transmitted arrival is not seen in Figures 2.4A(a) and 2.5A(a), its presence is obvious as a small pulse in the convolved result in Figures 2.4B(a) and 2.5B(a). Also, the arrival time for the evanescent event is more precisely given in the latter form.

For synthetic results in the elastic case, we have chosen the velocity and density of the lower half-space to be twice as large as those in the upper half-space. The other parameters are given in the insets and legends of the figures. We work with non-dimensional quantities and the basic scale factors, $\bar{\beta}$ for velocity, $\bar{\rho}$ for density and \bar{l} for length, are 1 km/s, 1000 kg/m³ and 5 m, respectively.

Figure 2.6 presents synthetic seismograms for a horizontal array of receivers at 1 m

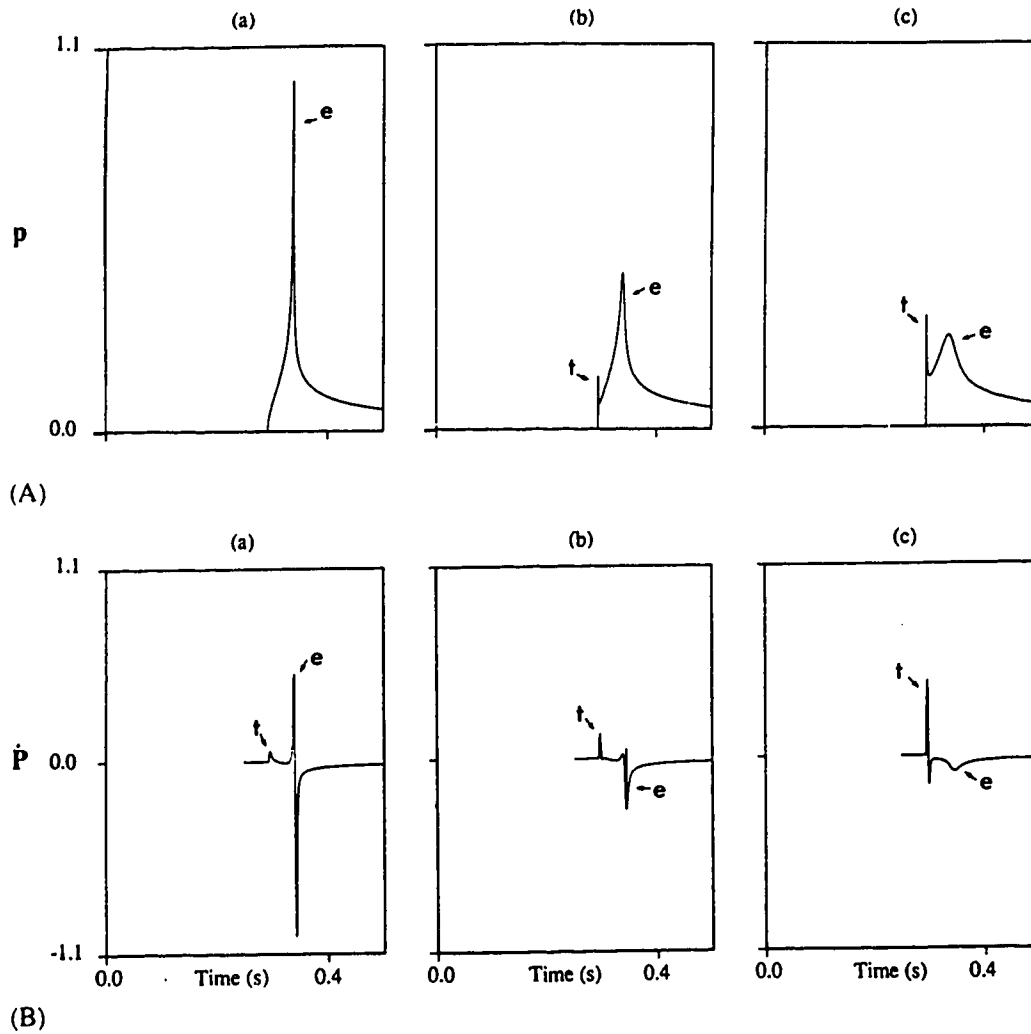


Figure 2.4: (A) Pressure responses for an acoustic model: $\alpha_1:\alpha_2 = 1.33$, $\rho_1:\rho_2 = 1.2$, receiver depth = 100 m, $x = 500$ m. The source heights z_0 are respectively (a) 1 m, (b) 7.5 m, (c) 30 m above the interface. This result is similar to Figure 4 of Drijkoningen and Chapman (1988); (B) the time derivative of the convolution of the pressure pulses in (A) with the Gaussian source function. The transmitted and evanescent arrivals are denoted as t and e .

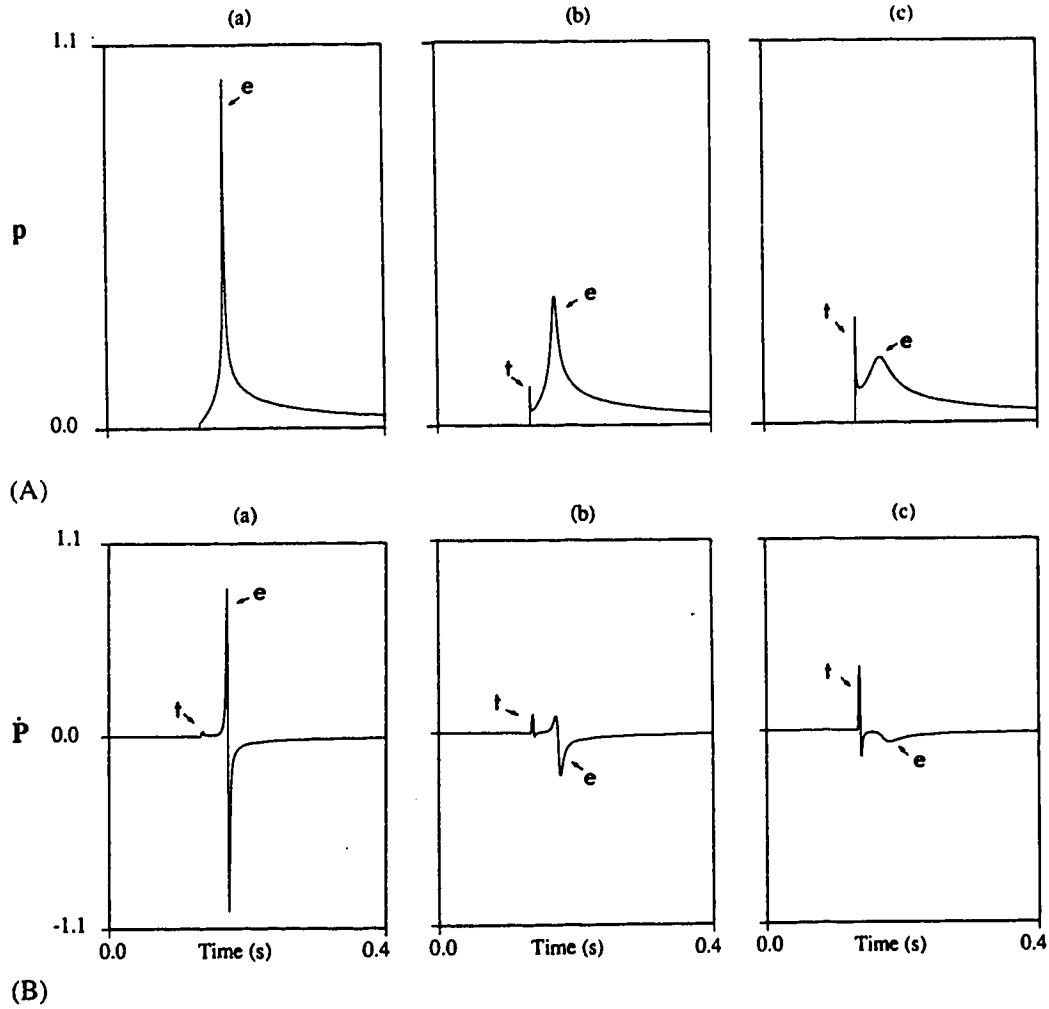


Figure 2.5: (A) Pressure responses for an acoustic model: $\alpha_1:\alpha_2 = 2.0$, $\rho_1:\rho_2 = 2.0$, receiver depth = 100 m, $x = 250$ m. The source heights z_0 are respectively (a) 1 m, (b) 7.5 m, (c) 30 m above the interface. This result is similar to Figure 5 of Drijkoningen and Chapman (1988); (B) the time derivative of the convolution of the pressure pulses in (A) with the Gaussian source function. The transmitted and evanescent arrivals are denoted as t and e .

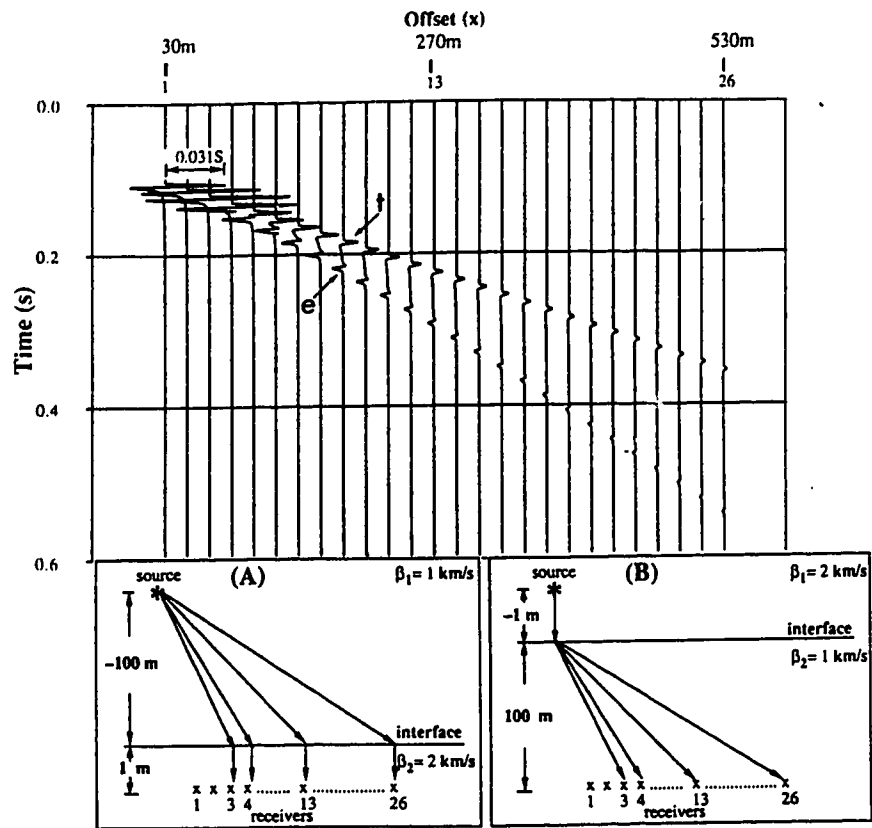


Figure 2.6: Synthetic seismograms for a horizontal array of receivers located below the interface for either the two cases depicted in insets (A) and (B). The transmitted and evanescent arrivals are denoted as t and e . For case (A), the velocities are 1 km/s and 2 km/s for the upper and lower half-spaces, respectively; for case (B), the high velocity half-space is above the low velocity one with a reversed source/receivers configuration. The rays show the paths of propagation and energy leakage for the postcritical event in each case. A scale factor S , equal to the basic scale factor \bar{l} for length, was applied to the graph in both cases.

below the interface to illustrate the behavior of the evanescent wave with offset. The critical distance is 57.7 m in this case. The evanescent wave appears at trace 4 and persists up to 530 m with almost the same amplitude as the transmitted arrival. The nature of the evanescent wave either called tunneling wave by Drijkoningen and Chapman (1988) or direct wave root by Stephen and Bolmer (1985) is well known and can be explained in terms of the so-called *wave of the lateral type* studied by Brekhovskikh (p282, 1980). The evanescent wave, which attenuates perpendicular to the boundary, bears a superficial resemblance to an anelastic wave propagating in a medium with finite Q (Borcherdt, 1973). For plane waves in an anelastic solid, it is found that the phase propagation is at a different angle to that of maximum attenuation. There is an important distinction in our elastic case, however, in that the phase velocity for an evanescent wave varies with the incident angle which is always greater than critical (inset A of Figure 2.6). The description of the wave path is given by the exponent in the first relation of (2.36). In inset A of Figure 2.6, the first line with an arrow represents a ray with propagation direction and phase velocity β_1 . The second arrow does not represent a ray path but indicates the direction of energy leakage and the direction of maximum attenuation. The energy diffuses into the lower medium with an approximate velocity β_2 .

By the reciprocity property, the seismograms for model 6A and 6B (case A and B of Figure 2.6) are identical. In model 6B, the high velocity half-space is on top of the low velocity one ($\beta_1:\beta_2 = \rho_1:\rho_2 = 2$) and the source is at 1 m above the interface with the receivers at 100 m below the interface. The explanation for case 6B is similar to that given above for case 6A and the wave path is described by the exponent in the first relation of (2.37). In this case, the evanescent energy are incident vertically from the source to the interface and excites the ordinary homogeneous wavefield in the lower medium. These waves then propagate to the receivers at all angles γ satisfying the condition $\sin\gamma > \beta_2/\beta_1$ (inset B of Figure 2.6).

Figure 2.7A is a vertical seismic profile (VSP) with offset greater than the critical distance for any receiver. The line of receivers intersects the horizontal profile shown in Figure 2.6, the trace 39 of Figure 2.7A being the same as the trace 12 of Figure 2.6. All the essential arrivals (direct, reflected, head wave and transmitted) are present. At receiver 39, which is located at 1 m below the interface, an evanescent wave arrives after the transmitted arrival and at approximately the same time as the incident arrival at receiver 37 located 3 m above the interface. The traces below the interface (with five additional traces) are magnified in Figure 2.7C to demonstrate the damping effect of the evanescent wave with depth. When the receiver is close to the interface, the amplitude of the evanescent wave is almost identical to that of the transmitted arrival (see trace 39 in Figure 2.7C). The event dies off rapidly with depth.

Figure 2.8 displays the logarithmic amplitudes of both the transmitted and evanescent waves versus depth. The evanescent amplitudes were measured from enlarged plots with respect to the tails of the transmitted waves. Several interesting properties can be observed from this plot. In the proximity of the boundary, the amplitudes of the transmitted and evanescent arrivals are comparable. A little deeper, the evanescent wave amplitude decreases, at first with a non-linear gradient on the logarithmic plot, but eventually, at about two characteristic wavelengths from the interface, the gradient on the logarithmic plot is linear. This is in accordance with Brekhovskikh's theory applied to the evanescent wave [see (2.36)], based on the asymptotic approximation for large $k_1 z$. Expressing k_1 and z in terms of wavelength $k_1 = 2\pi/\lambda_d$ and $z = n\lambda_d$, we find $k_1 z = 2\pi n$. For $n = 1.6$ we have $k_1 z$ equal to about 10 which seems to define for this case what a "large" number is, i.e., the limit of applicability of the asymptotic approximation given by (2.36), which, for fixed x and z_0 , is obtained by retaining only the first term in an asymptotic expansion in powers of $(k_1 z)^{-1}$.

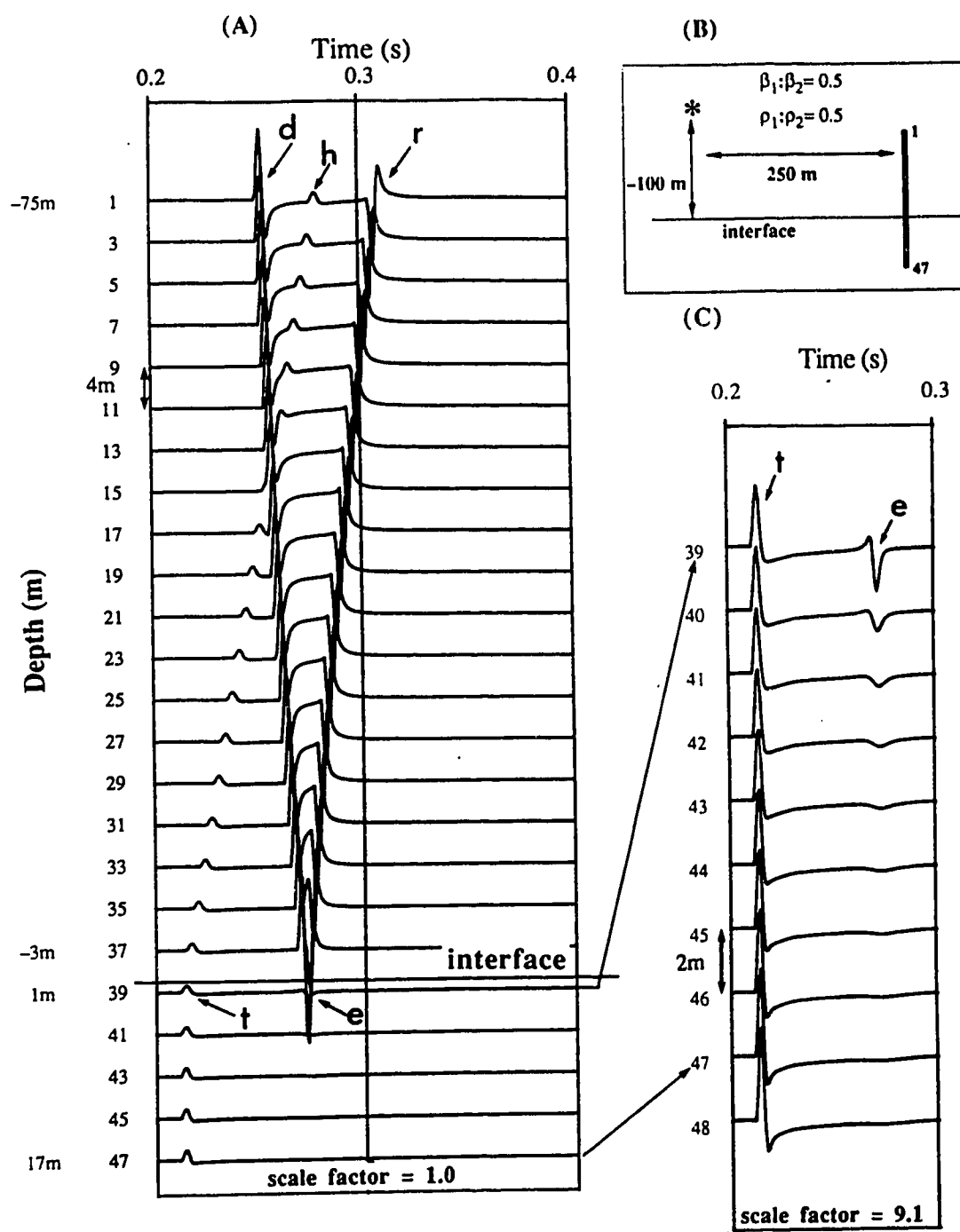


Figure 2.7: (A) The synthetic seismograms of a vertical seismic profile (VSP) for an elastic model. Only seismograms for "odd" receivers are shown. The direct, reflected, head waves, transmitted and evanescent arrivals are, respectively, denoted as d , r , h , t and e ; (B) the model used in (A) with 47 receivers. The source is indicated by a star (*); (C) a magnified VSP for the ten traces below the interface. Each of the seismic profiles is magnified by the indicated scale factor.

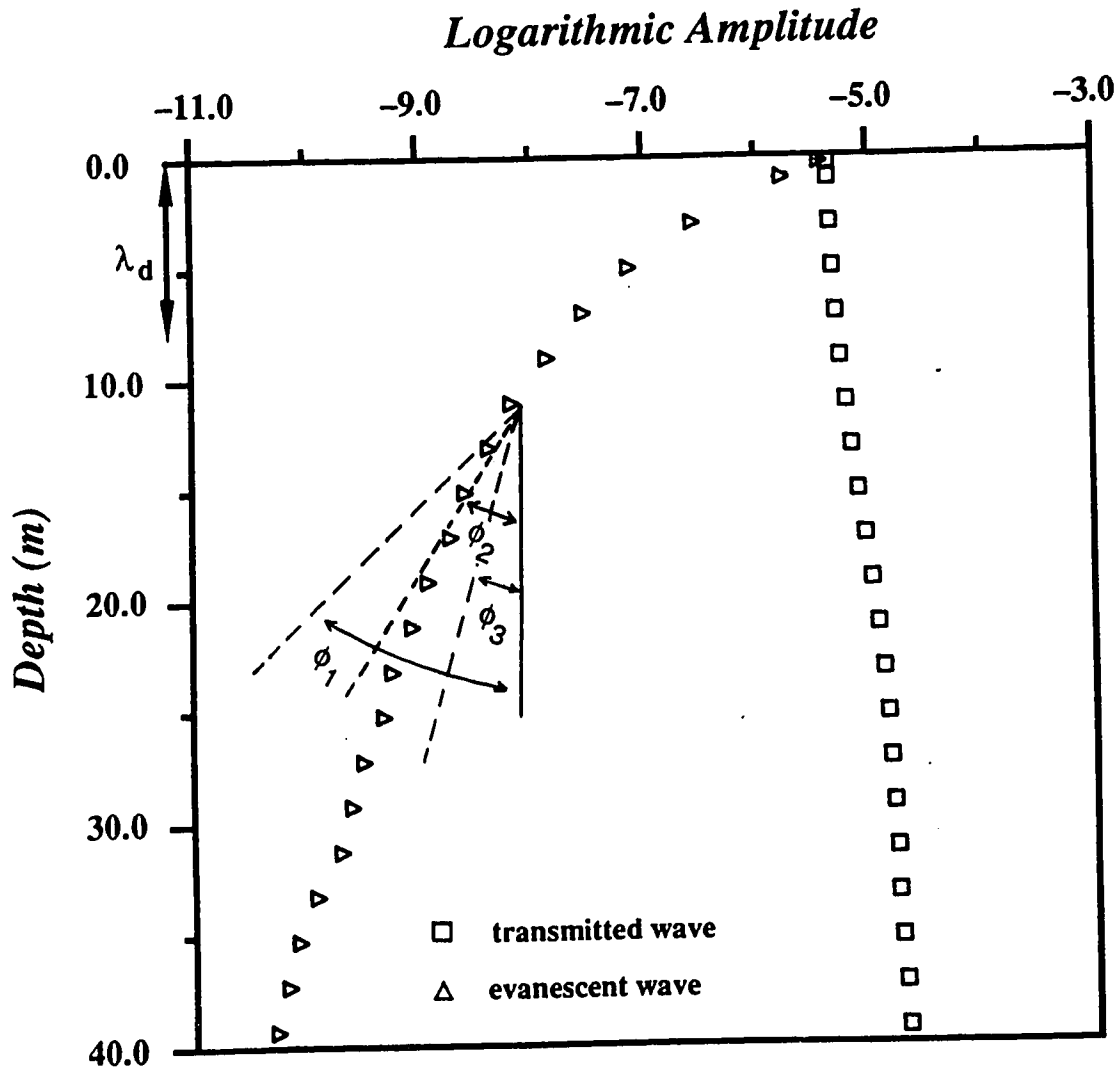


Figure 2.8: Logarithmic amplitudes of transmitted and evanescent waves versus depth.

The results were obtained graphically from enlarged plot similar to Figure 2.7C with 21 subsurface receivers. The first receiver is at 0.3 m below the interface while the second one is 1 m away from the interface and all the other receivers are located further down at 2 m spacing. The slope of the dashed line having angle ϕ_2 ($\approx 31^\circ$, $f_d = 123$ Hz) with respect to depth axis, is given by $[2\pi(\sin^2\gamma - (\beta_1/\beta_2)^2)^{1/2}]/\lambda_d$ where λ_d is obtained at the peak frequency. The other two limits, ϕ_1 ($\approx 46^\circ$, $f_1 = 208$ Hz) and ϕ_3 ($\approx 15^\circ$, $f_3 = 55$ Hz), are obtained at frequencies with respect to two-thirds of the peak spectral value. Note that the slope for ϕ_3 corresponds to the leakage of the evanescent wave at greater depths (> 30 m).

2.5 Conclusion

The study of the evanescent wave is important because its existence is not just a theoretical solution of the wave equation but also its actual presence has been widely observed: in favorable model and source/receivers configurations as illustrated in some of our figures, the amplitude of the evanescent wave is almost as big as the transmitted arrival. The properties of amplitude decay with depth or horizontal separation is a valuable means of retrieving the shallow crustal velocity information unattainable by conventional body wave analysis as mentioned by Stephen and Bolmer (1985).

CHAPTER 3

THE SOLUTION OF CAGNIARD'S PROBLEM FOR AN *SH* LINE SOURCE IN ELASTIC AND ANELASTIC MEDIA, CALCULATED USING THE ω - k INTEGRALS

3.1 Introduction

The problem considered in this chapter is one with an *SH*-pulse generated by a line source acting in a model consisting of two homogeneous, isotropic, linear viscoelastic half-spaces separated by a plane boundary. A previous treatment of this problem was done by Buchen (1971a) using asymptotic theory of Brekhovskikh (1980). In Chapter 2 the case when the half-spaces are elastic was presented with numerical results calculated using the Cagniard's method. It has been showed that the particle velocity at various source-receiver separations presents all the features predicted by our physical intuition, such as reflected and transmitted phases. It has also been demonstrated that for offsets beyond the critical distance, evanescent waves can occur, their arrival times and amplitude variation being consistent with Brekhovskikh's asymptotic theory for lateral waves. These results confirm, on the practical side, that the solution obtained by the Cagniard's method is exact, and the only errors are those introduced in the numerical evaluation of the integrals in the analytic representation of the solution. These errors can be made as small as desired by taking a sufficient number of integration nodes, and no other approximations are involved with this method. Unfortunately, for more complicated structures, like a stack of layers of variable elastic properties or a stack of anelastic layers, we are not able to use the Cagniard's method. Hence, if one wants an accurate solution, another direction must be sought. An immediate choice would be the classical representation of the solution for flat

structures in terms of double improper integrals, representing inverse integral transforms.

One of the advantages of using the double integral representation is that we are able to treat the anelastic structures in the same way as we treat the elastic ones. For the case of two homogeneous half-spaces treated here, we have found that all the types of waves present in the elastic case, are propagated also in anelastic structures, including the evanescent wave. As expected, the arrival times of all the phases have a delay, the pulse is dispersed and their amplitude decreases with increasing Q^{-1} .

The outline of this chapter is as follows. The solution is presented for a line source acting in a homogeneous space and subsequently in a model consisting of two half-spaces. The solution for an anelastic medium is obtained from the solution for an elastic one by making the elastic parameters complex. After describing the implementation of absorption using Azimi's dispersion law (Azimi et al., 1968 and Aki and Richards, 1980) and some related aspect of inhomogeneous plane wave theory (Lockett, 1962 and Cooper, 1967), a numerical procedure is given based on a similar treatment of elastic wave guides (Abramovici, 1968a and b) and of electromagnetic wave propagation due to antennas placed on the surface of a conducting earth (Abramovici and Chlamtac, 1978).

3.2 The Source Solution

Assume that in a homogeneous elastic space, a *SH* line source acts along the *y*-axis at the origin. Any motion due to the line force is directed along the *y*-direction and is independent of *y*, i.e., the problem is two-dimensional. The displacement component *v* in the *y*-direction away from the origin satisfies the force-free *S*-wave equation

$$\frac{\partial^2 v}{\partial t^2} - \beta^2 \nabla^2 v = 0 \quad , \quad \beta = \sqrt{\frac{\mu}{\rho}} \quad , \quad (3.1)$$

∇^2 being the Laplace operator. Here μ is the rigidity and β , the velocity. In cylindrical polar coordinates having the line source as axis, the Fourier transform

$V = \int_{-\infty}^{\infty} v(t) e^{-i\omega t} dt$ satisfies the Bessel equation

$$\frac{d^2 V}{dr^2} + \frac{1}{r} \frac{dV}{dr} + k^2 V = 0, \quad k = \frac{\omega}{\beta}. \quad (3.2)$$

Assuming that the disturbance is generated along the line source and is propagated away from this line, the only acceptable solutions are of the form

$$V = C H_0^{(2)}(kr) \quad (3.3)$$

with $H_0^{(2)}$ the Hankel function of the second kind of zero order and C a constant that depends on ω . The time-dependent displacement is:

$$v = v(x, z, t) = \frac{1}{2\pi} \int_{-\infty}^{\infty} C(\omega) H_0^{(2)}(kr) e^{i\omega t} d\omega. \quad (3.4)$$

The connection between $C(\omega)$ and the physical properties of the source is obtained as follows. Consider a small cylinder of unit length along the y -axis as depicted in Figure 3.1 and assume that on the lateral surface of this cylinder a given force is acting in the y -direction. The force per unit length $f = f(t)$ satisfies

$$f(t) = \lim_{r \rightarrow 0} (2\pi r \tau_{ry}). \quad (3.5)$$

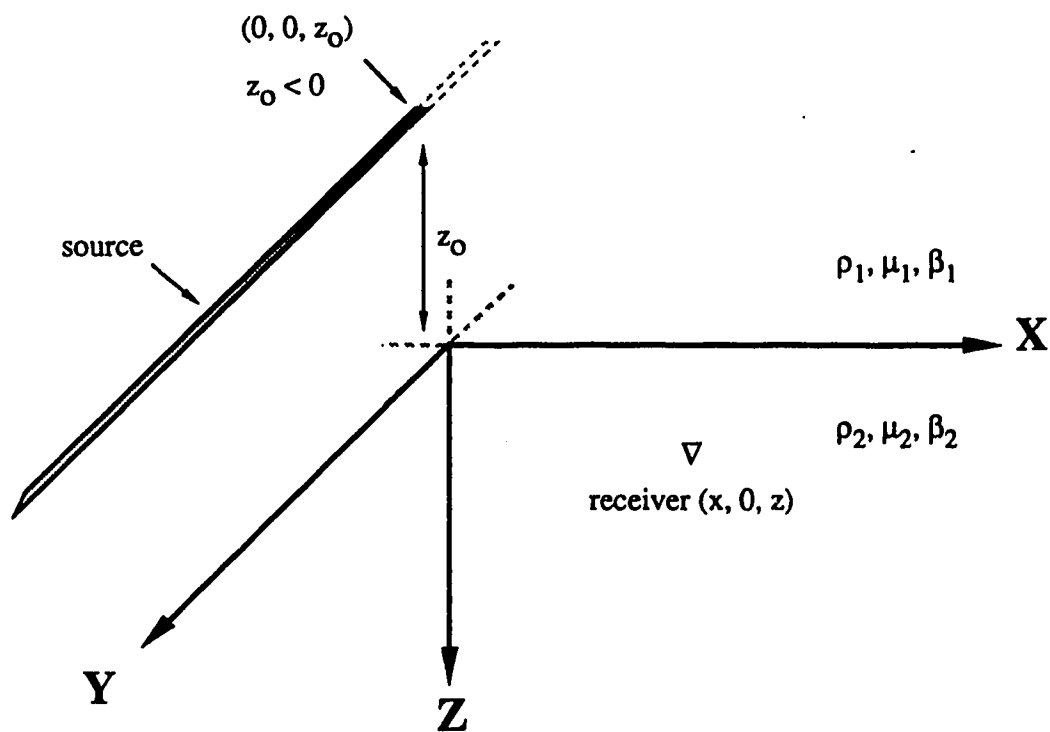


Figure 3.1: A line source of unit length along the y -axis generating SH waves and the geometry of the model.

Denoting by f_o the force per unit length, per unit time and assuming that the time variation of the source $g(t)$ is causal, we get, using Hooke's law,

$$f(t) = -f_o g(t) = \mu \int_{-\infty}^{\infty} C(\omega) e^{i\omega t} \lim_{r \rightarrow 0} \left[r \frac{dH_o^{(2)}(kr)}{dr} \right] d\omega . \quad (3.6)$$

However, (Watson, 1966)

$$\lim_{r \rightarrow 0} \left[r \frac{dH_o^{(2)}(kr)}{dr} \right] = \frac{2}{\pi i} , \quad (3.7)$$

leading to

$$C(\omega) = -\frac{f_o i}{4\mu} G(\omega) , \quad (3.8)$$

with $G(\omega)$ the Fourier transform of $g(t)$. Using the integral representation for the

Hankel function (Watson, 1966), $H_0^{(2)}(kr) = \frac{i}{\pi} \int_{-\infty}^{\infty} e^{-\nu|z|} \frac{-ikx}{\nu} dk$ where

$$\nu = \begin{cases} \sqrt{k^2 - \frac{\omega^2}{\beta^2}} & \text{if } |k| > \frac{|\omega|}{\beta} \\ i \sqrt{\frac{\omega^2}{\beta^2} - k^2} & \text{if } |k| < \frac{|\omega|}{\beta} \end{cases} \quad (3.9)$$

one arrives at the following representation for the displacement generated by the source at the origin:

$$v = \frac{f_0}{8\pi^2\mu} \int_{-\infty}^{\infty} G(\omega) e^{i\omega t} d\omega \int_{-\infty}^{\infty} e^{-v|z| - ikx} \frac{dk}{v} \quad . \quad (3.10)$$

3.3 The Solution In Two Half-Spaces

Consider two homogeneous elastic half-spaces in welded contact. Choose a right-handed Cartesian coordinate system depicted in Figure 3.1 and assume that a line source located at a height z_0 ($z_0 < 0$) in the upper half-space, generates a force directed only in the y -direction. The differential equations governing the particle displacement v everywhere except at the source are

$$\frac{\partial^2 v_j}{\partial t^2} = \beta_j \nabla^2 v_j \quad (j = 1, 2) \quad . \quad (3.11)$$

The boundary conditions to be satisfied at the interface, $z = 0$ are:

$$v_1 = v_2 \quad , \quad \mu_1 \frac{\partial v_1}{\partial z} = \mu_2 \frac{\partial v_2}{\partial z} \quad . \quad (3.12)$$

We take v_1 and v_2 in the same form as v for the homogeneous whole-space case , [eq. (3.10)], i.e., we seek P_1 and P_2 , as functions of ω and k , so that:

$$v_1 = \frac{f_0}{8\pi^2\mu_1} \int_{-\infty}^{\infty} G(\omega) e^{i\omega t} d\omega \int_{-\infty}^{\infty} P_1 e^{-ikx} dk \quad \text{for } z < 0 \quad (3.13)$$

and

$$v_2 = \frac{f_0}{8\pi^2\mu_1} \int_{-\infty}^{\infty} G(\omega) e^{i\omega x} d\omega \int_{-\infty}^{\infty} P_2 e^{-ikx} dk \quad \text{for } z > 0. \quad (3.14)$$

Equations (3.11) and the source condition will be satisfied if we take P_1 and P_2 as follows:

$$P_1 = \frac{1}{v_1} e^{-v_1 |z - z_0|} + A e^{v_1 z} \quad (3.15)$$

and

$$P_2 = B e^{-v_2 z} \quad (3.16)$$

where v_j are defined by (3.9) with β replaced by β_j , for $j = 1, 2$. The boundary conditions (3.12) will be satisfied if:

$$A = \frac{\mu_1 v_1 - \mu_2 v_2}{\mu_1 v_1 + \mu_2 v_2} \frac{e^{v_1 z_0}}{v_1}, \quad B = \frac{2\mu_1}{\mu_1 v_1 + \mu_2 v_2} e^{v_1 z_0}. \quad (3.17)$$

Hence, the solution of the problem for $z < 0$ is:

$$v_1 = \frac{f_0}{8\pi^2\mu_1} \int_{-\infty}^{\infty} G(\omega) e^{i\omega x} d\omega \int_{-\infty}^{\infty} \frac{1}{v_1} \left[e^{-v_1 |z - z_0|} + \frac{\mu_1 v_1 - \mu_2 v_2}{\mu_1 v_1 + \mu_2 v_2} e^{v_1 (z + z_0)} \right] e^{-ikx} dk \quad (3.18)$$

and for $z > 0$ it is:

$$v_2 = \frac{f_0}{8\pi^2\mu_1} \int_{-\infty}^{\infty} G(\omega) e^{i\omega x} d\omega \int_{-\infty}^{\infty} \frac{2\mu_1}{\mu_1 v_1 + \mu_2 v_2} e^{v_1 z_0 - v_2 z} e^{-ikx} dk. \quad (3.19)$$

3.4 Attenuation

One of the most natural ways of introducing absorption into the media is to make the velocity complex (Knopoff, 1964b; Sato, 1967; Clowes and Kanasewich, 1970; Kennett, 1975; Silva, 1976; O'Neill and Hill, 1979 and Kelamis et al., 1983) with the degree of intrinsic absorption characterized by the quality factor Q . In order for the pulse to be causal, we must also consider dispersion with the real part of velocity being frequency-dependent. We adopt Azimi's law (Azimi et al., 1968 and Aki and Richards, 1980) for frequencies no less than the reference frequency $f_r = 0.1$ Hz:

$$c(\omega) = c_r \left[1 + \frac{1}{\pi Q} \ln \left(\frac{f}{f_r} \right) + \frac{i}{2Q} \right] . \quad (3.20)$$

c_r is found by assuming that $c(\omega)$ approaches the model velocity at $f = 250$ Hz. Below the reference frequency there is no dispersion, the elastic velocity being replaced by $c_r \left(1 + \frac{i}{2Q} \right)$. The seismic waves in media with absorption are inhomogeneous. The characteristic properties of monochromatic plane waves in two half-spaces have first been examined by Lockett (1962) and Cooper (1967) and further explored by Buchen (1971b), Borchardt (1973, 1977) and Krebs (1980). Such waves are of the form:

$$e^{-i \vec{K} \cdot \vec{r}} = e^{-i(\vec{P} - i\vec{A}) \cdot \vec{r}} , \quad (3.21)$$

where the complex wave vector \vec{K} has modulus squared given by

$$K^2 = \vec{K} \cdot \vec{K} = (\vec{P} - i\vec{A}) \cdot (\vec{P} - i\vec{A}) = \frac{\omega^2}{c^2(\omega)} . \quad (3.22)$$

The vector \vec{P} points in the direction of increasing phase delay such that $\frac{\omega}{|\vec{P}|}$ is the phase speed, while \vec{A} points in the direction of maximum attenuation such that $\exp(-\vec{A} \cdot \vec{r})$ contributes to the spatial decay of amplitude.

3.5 The Numerical Integration

In order to compare results based on the ω - k integration with results calculated by the Cagniard's method, we computed the particle velocity for the same source, a Gaussian time function with Fourier transform

$$G(\omega) = i\omega \sqrt{\frac{\pi}{\sigma}} e^{-\omega^2/4\sigma - i\omega t_d} \quad (3.23)$$

This is identical to the one we used in Cagniard's problem [see equation (2.20) and Figure 2.3] with dominant frequency 50 Hz ($\omega_d = \sqrt{2\sigma}$, $t_d = \sqrt{\frac{2}{\sigma}}$ and $\sigma = 5 \cdot 10^4$). As the spectrum $|G(\omega)|$ of the considered time function decreases rapidly for frequencies not close to the dominant one, even when multiplied by $|\omega|$, the integral on ω extends practically over a relatively short interval. Hence, a fast Fourier transform with not too many frequency points will take care of the integration with respect to ω . However, in order to avoid high frequency computational noise coming from outside the relevant interval, we applied a cosine taper (0/5/230/250 Hz).

The price in accuracy paid when using the taper consists in having the peaks of the main events lower in height and slightly broadened. This source of accuracy loss should be compounded with that due to using only a finite set of frequency components. In view of the large reduction of the needed computer time and the total elimination of the high frequency noise, we found that the price is worthwhile, as one can see in Figures. 3.6a and

3.6b. However, improving the numerical methods and going over to either a supercomputer or a parallel computer, we will achieve a much higher accuracy, so that the ω - k seismograms will be much closer to the exact ones, e.g., the smooth onset seen on the mentioned figures will be much closer to the sharp one seen on the seismograms calculated by the Cagniard's method.

As to the k -integral, its integrand decreases eventually to zero, but has an oscillatory character as can be seen on Figure 3.2 representing the real and imaginary parts of the integrand for $z < 0$ at a frequency approximately equal to 5 Hz. The method to be used to calculate the k -integral, therefore, takes into account the possibility of this oscillatory character. We use the Euler's transformation method (Hildebrand, 1974) which was employed for the first time for the integrals occurring in seismology by Longman (1956) and proved to work also in antenna problems (Abramovici and Chlamtac, 1978). For intervals bounded by the zeros of the cosine function we used a 16-points Gaussian quadrature integration scheme with four split intervals. The number of terms used for Euler's transformation was related to the decay character of the integrand, having the calculation terminated when the terms do not contribute significantly to the integral. The tolerance used was 10^{-7} .

For the receiver in the same half-space as the source, it took on the average 4 min CPU on the Amdahl 5670 to obtain a whole seismogram while for a receiver in the other half-space it took less than 2 min. All the controlled parameters used are quite conservative as we want to compare with the exact result using Cagniard's method. Each seismogram presented here was calculated using 512 frequency points. Considering only half the number of frequencies, we obtained similar seismograms with a 16-point Gauss rule. A flow-chart of the computer code is provided in Figure 3.3.

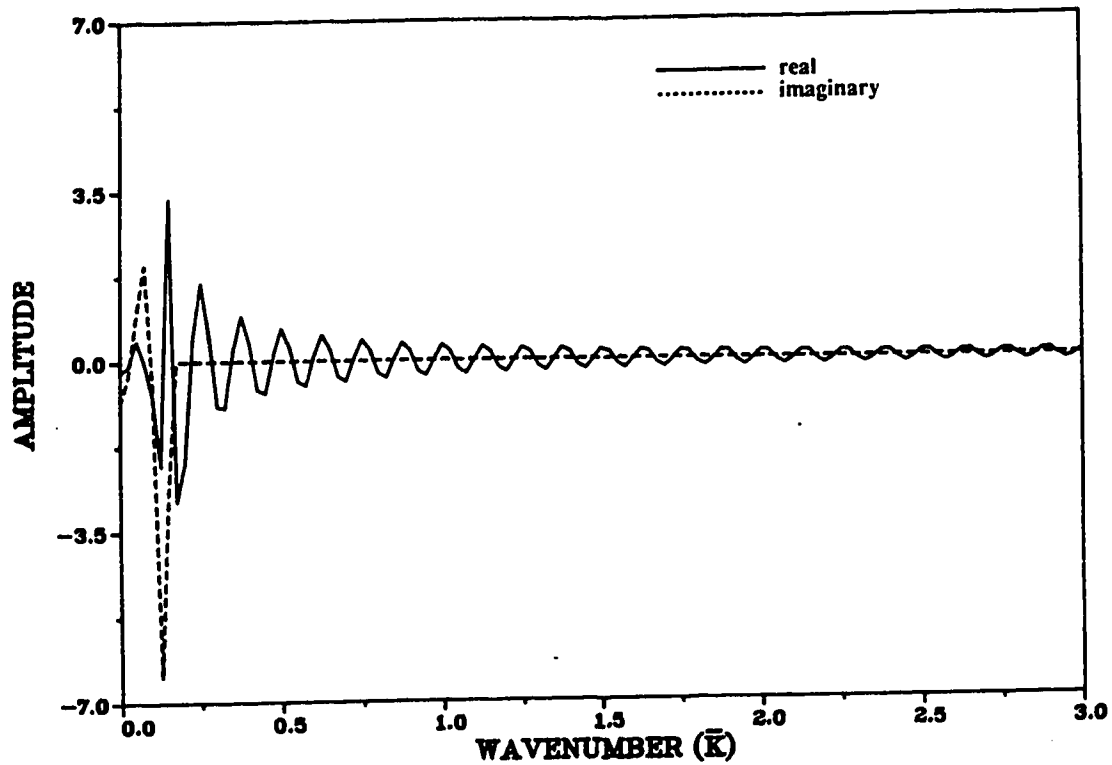


Figure 3.2: The behavior of the integrand P_I given by the expression (3.15) at 5 Hz for the elastic model in Figure 3.4e with the receiver being at the same level as the source. \bar{k} is the dimensionless horizontal wavenumber.

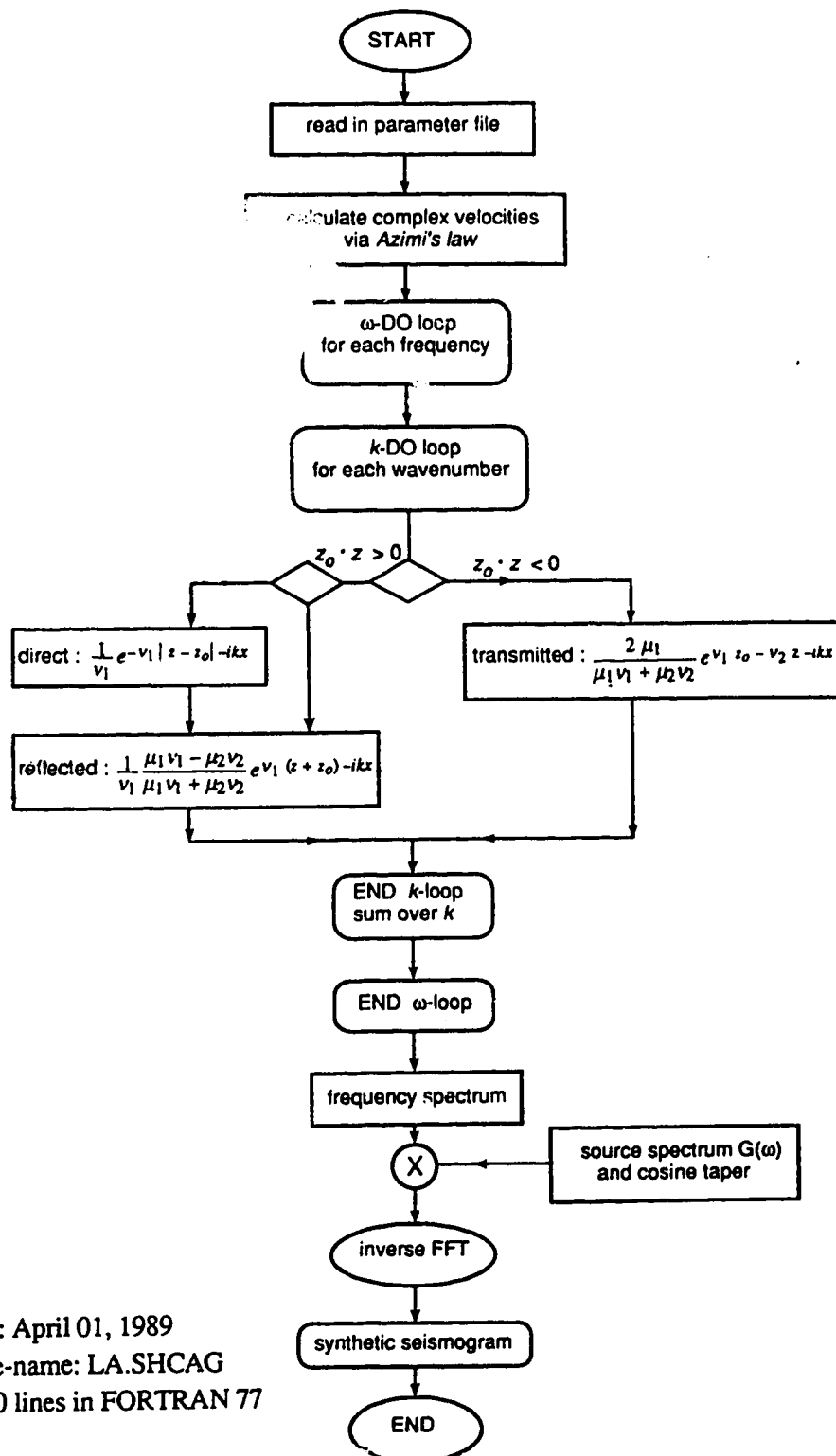


Figure 3.3: A flow-chart of the computer code LA.SHGAG.

3.6 Discussion Of Results

For the presented synthetic seismograms, we have chosen the velocity and density of the lower half-space to be twice as large as those in the upper half-space. The other parameters are on the figures themselves or their legends. We worked with non-dimensional quantities, the basic scale factors, $\bar{\beta}$ for velocity, $\bar{\rho}$ for density and \bar{l} for length being 2 km/s, 2000 kg/m³ and 5 m, respectively. As displayed in Figures 3.4 and 3.5, the results calculated for a sequence of receivers compare very well with the corresponding results calculated by the Cagniard's method, although they cannot be identical. We can see the differences when we plot two traces on an enlarged scale, e.g. in Figure 3.6a we compare the results for a configuration when the receiver is in the same half-space as the source and in Figure 3.6b the comparison is for a receiver on the other side of the interface. All the results described above represent elastic structures. We did, however, a number of calculations for anelastic structures and the corresponding seismograms show delays in the arrival times of the various phases, dispersion of the pulses and a decrease in amplitude. In Figure 3.4c we show seismograms for a vertical array of receivers for half-spaces having $Q = 50$. All the phases seen on the seismograms for the perfectly elastic structure (Figures 3.4a and b) are present on the anelastic case too (Figures 3.4c and d), including the evanescent wave, but the amplitudes are smaller. Similar features are seen also on Figure 3.5c for a horizontal array of receivers located at 1 m just beneath the interface.

Borcherdt (1977), in one of his theorems, implied that in viscoelastic media, if the incident angle θ_i is equal to the critical angle θ_c , then the transmitted \vec{P}_t propagates along the interface; however, if θ_i increases beyond θ_c then \vec{P}_t is not parallel to the interface. On our numerical seismograms, both head waves and evanescent waves are present when a certain *critical distance* condition is satisfied. It seems, therefore, that even when \vec{P}_t is

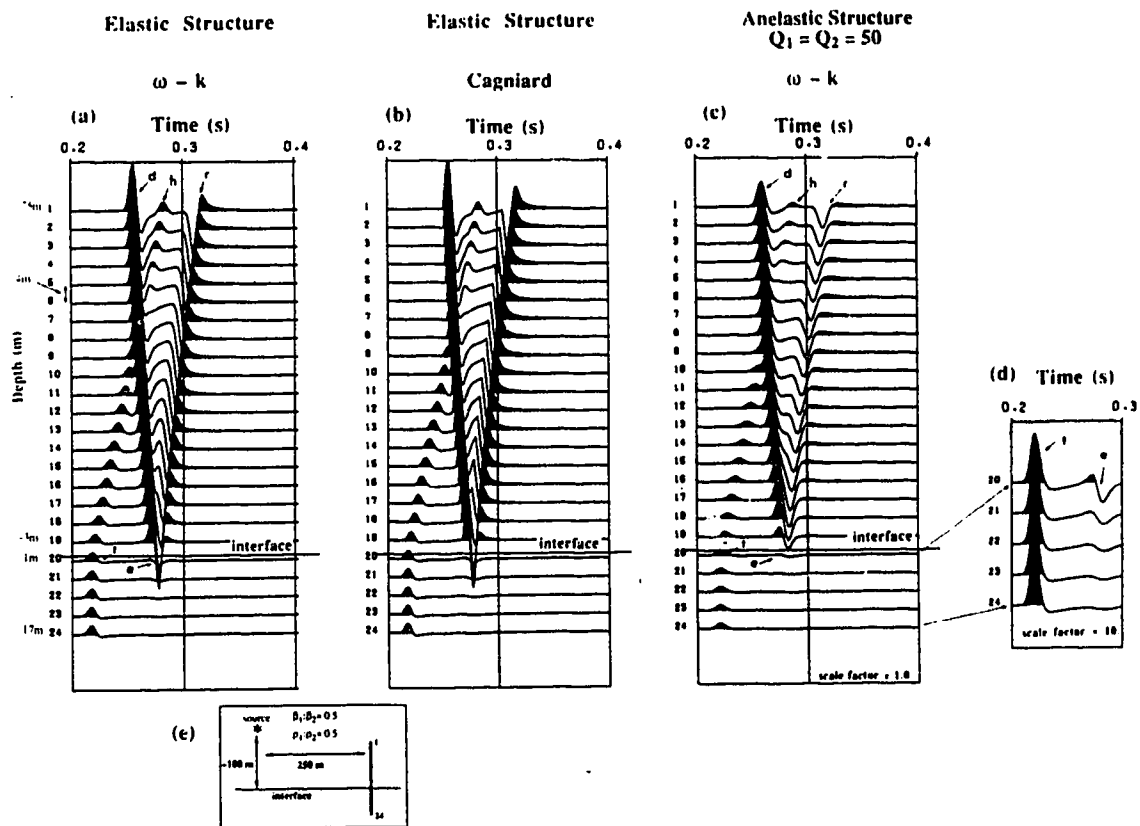


Figure 3.4: Comparison of results from two methods: (a) Synthetic seismograms of a vertical seismic profile (VSP) for an elastic structure using the ω - k method. The direct, reflected, head waves, transmitted and evanescent arrivals are denoted, respectively, as d , r , h , t and e . (b) The same VSP calculated using the Cagniard's method. Profiles (a) and (b) are individually normalized by the biggest absolute amplitude in that profile. (c) Synthetic seismograms of a VSP for an anelastic structure using the ω - k method. The profile is normalized by the same scale factor as obtained in (a). (d) A VSP for the five traces below the interface on plot (c), magnified by a factor of 10. (e) The model used in all calculations.

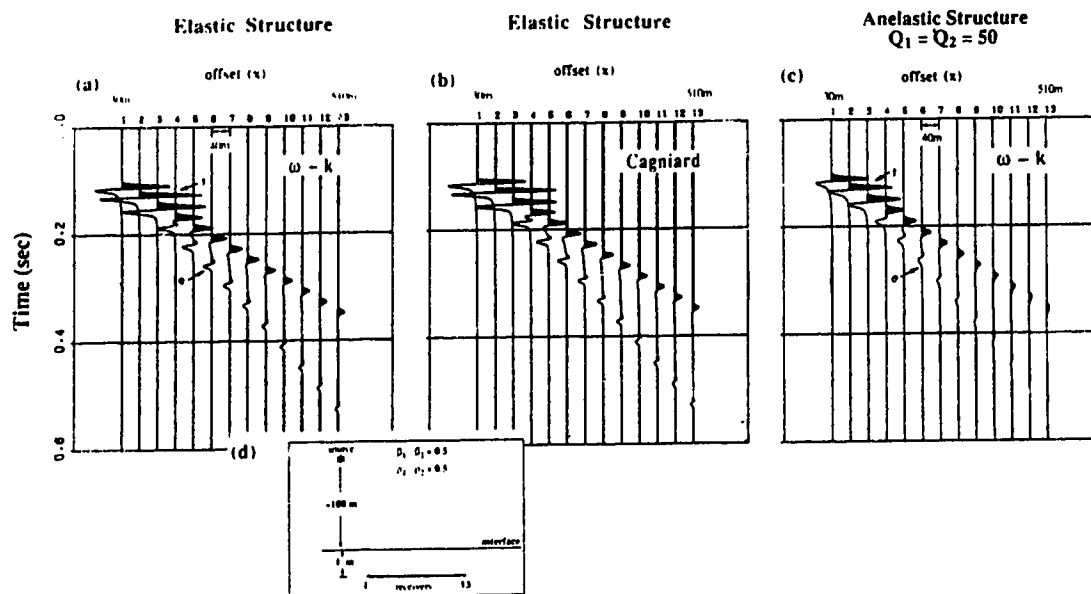


Figure 3.5: Comparison of results using two methods: (a) Synthetic seismograms for a horizontal array of receivers located below the interface for an elastic structure using the $\omega-k$ method. The transmitted and evanescent arrivals are denoted as t and e . (b) The same section calculated using the Cagniard's method. Profiles (a) and (b) are individually normalized by the biggest absolute amplitude in that profile. (c) Synthetic seismograms for the same receiver configuration for an anelastic structure using the $\omega-k$ method. The profile is normalized by the same scale factor as obtained in (a). (d) The model used in all calculations.

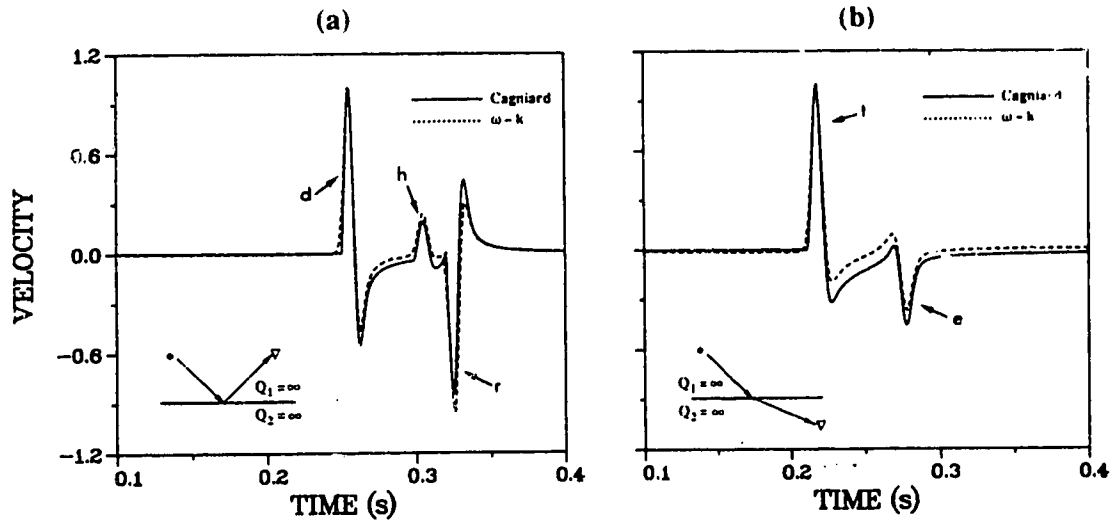


Figure 3.6: Comparison of results from two methods for an elastic structure: Cagniard (solid line) and $\omega-k$ (dashed line). (a) The receiver is in the same half-space as the source ($z_o = -100$ m, $x = 250$ m, $z = -100$ m). (b) The receiver is in the other half-space ($z = 3$ m). The direct, reflected, head waves, transmitted and evanescent arrivals are, respectively, denoted as d , r , h , t and e . (*) and (V) symbolize the source and the receiver. The seismogram calculated by the $\omega-k$ method is normalized by the same factor of the corresponding seismogram obtained by the Cagniard's method.

not parallel to the interface, it is almost so (Krebes, 1980). As the concept of a critical angle or distance is somehow degraded for plane waves in viscoelastic medium, the appearance of head and evanescent waves seems to be explained better by considering the effect of the boundary conditions on a curved wavefield produced by a source of finite or infinite extent (Richards, 1984).

In Figure 3.7, we depict, on the same scale, seismograms for an elastic case and for two anelastic structures: one having $Q = 100$ in both half-spaces (Figures 3.7a and b), the other $Q = 50$ (Figures 3.7c and d). Receivers have been located in both half-spaces so that we see the incident wave arriving from the source, then the head wave and the reflected one in the source medium (Figures 3.7a and c) and also the transmitted wave in the refracted medium (Figures 3.7b and d). For lower values of Q (higher attenuation), we have consistently a bigger time-delay for the arrival, greater dispersion and a greater diminishing of the amplitude.

In Figure 3.8 we considered two cases when one of the half-spaces is elastic and the other anelastic with $Q = 50$. Figures 3.8a and b show a case when the source is located in the elastic half-space while in Figures 3.8c and d the source medium is anelastic. As we can see from the figures, the dispersion and attenuation are stronger in the latter case.

3.7 Conclusion

The synthetic seismograms calculated using the ω - k integrals seem to be accurate enough even when the number of frequencies used is not too high to make the amount of needed computer time unreasonable. The advantage of this method is that it shows complete seismograms in relevant time and frequency windows both for perfectly elastic media and also for viscoelastic ones.

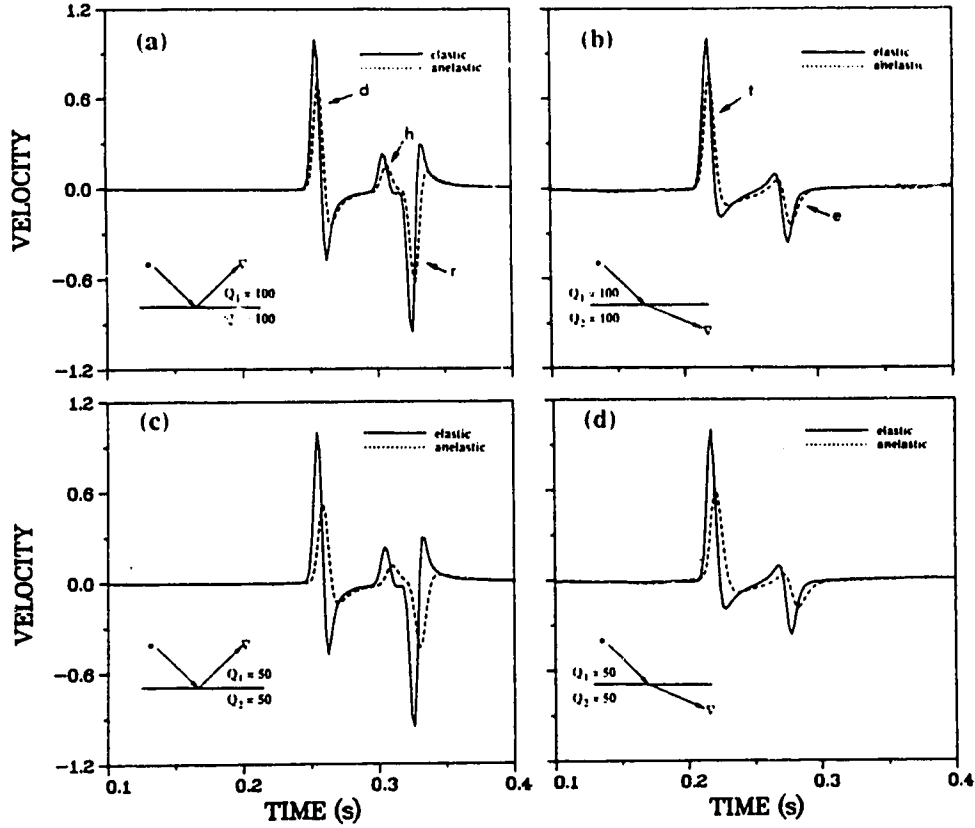


Figure 3.7: Comparison of elastic (solid line) and anelastic (dashed line) results. The elastic results are calculated by the Cagniard's method. (a) The receiver is in the same half-space as the source ($z_o = -100$ m, $x = 250$ m, $z = -100$ m) with $Q_1 = Q_2 = 100$. (b) The receiver is in the other half-space ($z = 3$ m) with $Q_1 = Q_2 = 100$. The direct, reflected, head waves, transmitted and evanescent arrivals are, respectively, denoted as d , r , h , t and e . (c) same as (a) but $Q_1 = Q_2 = 50$; (d) same as (b) but $Q_1 = Q_2 = 50$. (*) and (V) symbolize the source and the receiver. The seismogram calculated by the ω - k method is normalized by the same scale factor of the corresponding seismogram obtained by the Cagniard's method.

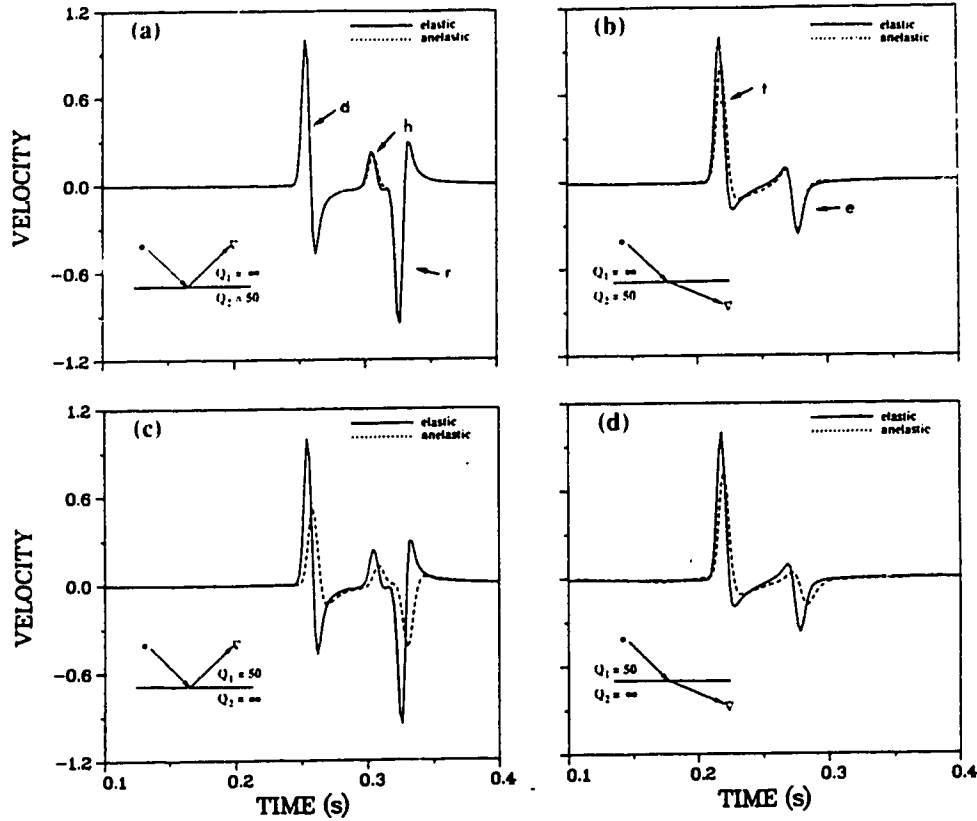


Figure 3.8: Comparison of elastic (solid line) and anelastic (dashed line) results. The elastic results are calculated by the Cagniard's method. (a) The receiver is in the same half-space as the source ($z_o = -100$ m, $x = 250$ m, $z = -100$ m) with $Q_1 = \infty$ and $Q_2 = 50$. (b) The receiver is in the other half-space ($z = 3$ m) with $Q_1 = \infty$ and $Q_2 = 50$. The direct, reflected, head waves, transmitted and evanescent arrivals are, respectively, denoted as d , r , h , t and e . (c) same as (a) but $Q_1 = 50$ and $Q_2 = \infty$; (d) same as (b) but $Q_1 = 50$ and $Q_2 = \infty$. (*) and (∇) symbolize the source and the receiver. The seismogram calculated by the ω - k method is normalized by the same scale factor of the corresponding seismogram obtained by the Cagniard's method.

For the simple model of two half-spaces in welded contact considered here, it seems that attenuation does not change radically the physical picture seen in the elastic case, but modifies it in a continuous manner, lengthening the time elapsed before a certain phase arrives to a receiver, broadening the pulse and diminishing its amplitude.

CHAPTER 4

SEISMOGRAMS USING THE ω - k INTEGRALS FOR A POINT P -SOURCE IN A VERTICALLY INHOMOGENEOUS ANELASTIC MODEL: THEORY AND COMPUTATIONAL ASPECTS

4.1 Introduction

The ω - k method has already been successfully applied to a simple case of two half-spaces in welded contact (Chapter 3). The present effort is to consider the much more complicated case of a stratified model, consisting of a vertically inhomogeneous layer welded to a homogeneous half-space, the layer being assumed to consist of a finite number of sublayers, that present singularities at interfaces. Each sublayer is assumed to be anelastic and not necessarily vertically homogeneous. The eigenvalue problem studying the wave propagation in stratified anelastic media can be formulated as a set of first order ordinary differential equations. The coefficient matrices of the systems thus formed depend on the elastic parameters of the media which are in turn continuous functions of the vertical coordinate, z within each sublayer. The displacement components on the free surface can be calculated by integrating directly the differential systems involved using a Runge-Kutta method. The solutions thus obtained are free from any approximation except numerical one.

The basic theory for elastic stratified models was known since the mid-sixties and beginning seventies, a landmark being the Gilbert and Backus (1966) paper, in which the first order ordinary differential systems for vertically inhomogeneous seismic structures were described and solved in terms of propagator matrices. Their approach was used by Abramovici (1968a) to calculate transfer functions for complex structures, by integrating

numerically the differential systems. In that paper, the exciting field was a random pressure acting on the surface of a homogeneous liquid layer present on the top of the structure. In a subsequent paper (Abramovici, 1968b), the disturbance was due to a point-source generating P -waves.

In the present chapter the basic theory pertaining to the solution of the wave equation for a layered anelastic solid half-space from a P -source is presented using the Fourier-Bessel representation (Abramovici, 1968a and b). In the mentioned papers of Abramovici, diagnostic diagrams were calculated to study waveguide problems. The new work developed in the next two chapters is the direct integration of the improper integrals in the k -space to obtain synthetic seismograms. The formalism allows the inhomogeneity of the medium to take any form along the depth axis with homogeneous discrete layers as a special case. The source is assumed to be in a homogeneous layer. The numerical methods to handle the boundary conditions in the presence of the source are also described. Azimi's law is used to account for dispersion and anelasticity (Abramovici, Le and Kanasewich, 1990). The k -integral is calculated first up to a user-controlled k_{\max} using a Romberg integration scheme. Long series of wavenumber and frequency are computed and are then cosine-tapered in f - k (or ω - k) space to avoid aliasing or wraparound events in the spatial-temporal domain. The inversion into the temporal domain is achieved through an inverse fast Fourier transform. The code was implemented on a parallel machine, Myrias SPS-2, with 64 processors using double precision FORTRAN 77. The final fast Fourier transform was carried out usually on the Amdahl 5670 main frame as were the graphical plots. In principle all the computation can be accomplished on a work station such as a SUN SPARC station 330 and this has been done occasionally although several days are required for a run to be completed. The numerical results and discussion of their significance will be given in Chapter 5.

4.2 The Mathematical Problem and its Formal Solutions

4.2.1 The Problem

Assume a vertically inhomogeneous model consisting of a stack of anelastic sublayers in welded contact with a homogeneous half-space. Within each sublayer, the elastic velocities, α and β and density ρ may vary continuously with the vertical coordinate. Anelasticity, quantified by the quality factor Q , is introduced in the frequency domain through Azimi's law (see Section 3.4). A point source generating P -waves in any sublayer is activated at an initial time $t = 0$. The disturbance at any point in the structure consists of both P and S -waves, due to reflection and transmission, and has cylindrical symmetry with respect to an axis that contains the source and is at right angle with the interfaces. Hence it is natural to use cylindrical coordinates in which all the quantities are independent of the azimuthal variable around the axis of symmetry. In order to satisfy the boundary conditions at the free surface and interfaces, as well as the radiation condition at infinity, one has to separate variables in the partial differential system involved and find the eigenfunctions of the problem.

A cylindrical system of coordinates, as depicted in Figure 4.1, is adopted with the z -axis oriented upwards from the bottom interface. For simplicity it is assumed here that the receiver is located anywhere on the free surface, at $z = H$, with H the total thickness of the inhomogeneous layer. The interfaces are located at $z = z_j, j = 0, 1, \dots, N-1$, with $z_0 = 0$ corresponding to the bottom interface, N being the number of sublayers. The Lamé parameters λ, μ and the density ρ are given functions of z in each sublayer, their constant values in the half-space being λ_0, μ_0 and ρ_0 .

Denoting the displacement components in cylindrical coordinates as s_r, s_z , and the stress components as τ_{rr}, τ_{zz} , etc., the mathematical problem for P -SV wave propagation, in the absence of body forces, consists in solving the momentum equations

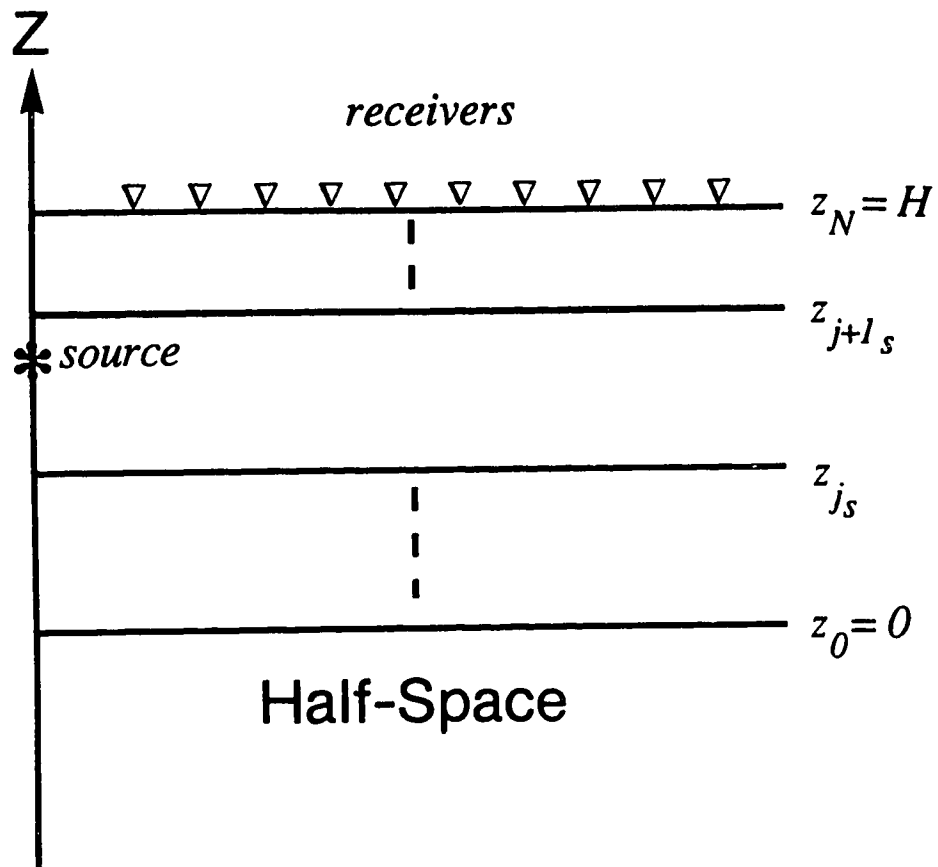


Figure 4.1: The geometry of the model. The source layer is bounded by z_{j+1_s} and z_{j_s} .

(Love, 1945; Eringer, 1965; Fung, 1977):

$$\begin{aligned}\rho \frac{\partial^2 s_z}{\partial t^2} &= \frac{\partial \tau_{zz}}{\partial z} + \frac{\partial \tau_{zr}}{\partial r} + \frac{\tau_{zr}}{r} \\ \rho \frac{\partial^2 s_r}{\partial t^2} &= \frac{\partial \tau_{rr}}{\partial r} + \frac{\partial \tau_{rz}}{\partial z} + \frac{\tau_{rr} - \tau_{\theta\theta}}{r}\end{aligned}\quad (4.1)$$

taking into account Hooke's law, (Love, 1945; Fung, 1977):

$$\begin{aligned}\tau_{rr} &= 2\mu \frac{\partial s_r}{\partial r} + \lambda \Delta \\ \tau_{zz} &= 2\mu \frac{\partial s_z}{\partial z} + \lambda \Delta \\ \tau_{\theta\theta} &= 2\mu \frac{s_r}{r} + \lambda \Delta \\ \tau_{zr} &= \mu \left(\frac{\partial s_r}{\partial z} + \frac{\partial s_z}{\partial r} \right)\end{aligned}\quad (4.2)$$

where Δ is the divergence of the displacement vector,

$$\Delta = \frac{\partial s_r}{\partial r} + \frac{\partial s_z}{\partial z} + \frac{s_r}{r}\quad (4.3)$$

so that:

1. zero initial conditions are satisfied for $t < 0$ (causality property);
2. boundary conditions of zero stress at the top surface and continuity of displacements

and stresses at any interface hold;

3. the Sommerfeld radiation condition holds for $z \rightarrow -\infty$;
4. in one of the sublayers which is homogeneous, a point source located on the z -axis at $z = z_s$ generates P -waves according to a given time-dependence $g(t)$.

The system of equations may be separated by using the following expressions of the displacement and stress components as products of functions of only one of the dependent variables (Ben Menahem, 1960; Abramovici, 1968b):

$$\begin{aligned}
 s_z &= k w(z) J_0(kr) e^{i\omega t} \\
 s_r &= q(z) \frac{\partial J_0(kr)}{\partial r} e^{i\omega t} \\
 \tau_{zz} &= k T_w(z) J_0(kr) e^{i\omega t} \\
 \tau_{zr} &= T_q(z) \frac{\partial J_0(kr)}{\partial r} e^{i\omega t}
 \end{aligned} \tag{4.4}$$

where k is the horizontal wavenumber, ω , angular frequency and J_0 , the ordinary Bessel function of order zero..

One obtains a more compact notation by defining a displacement-stress vector in physical variables (r, z, t) :

$$\mathbf{U} = \begin{bmatrix} s_z \\ s_r \\ \tau_{zz} \\ \tau_{zr} \end{bmatrix} \tag{4.5}$$

and its z -components as:

$$\mathbf{u} = \begin{bmatrix} w \\ q \\ T_w \\ T_q \end{bmatrix} . \tag{4.6}$$

The connection between \mathbf{U} and \mathbf{u} is

$$\mathbf{U} = \mathbf{D}\mathbf{u} \quad (4.7)$$

through the offset-dependent diagonal matrix:

$$\mathbf{D} = \text{diag} \left(kJ_0(kr), \frac{\partial J_0(kr)}{\partial r}, kJ_0(kr), \frac{\partial J_0(kr)}{\partial r} \right) e^{i\omega t} \quad (4.8)$$

Taking (4.8) into account and using simple recursion relations between Bessel functions, one finds that \mathbf{u} satisfies the following system of ordinary differential equations of fourth order (Gilbert and Backus, 1966; Abramovici, 1968b; Aki and Richard, 1980):

$$\frac{d\mathbf{u}}{dz} = \mathbf{M}\mathbf{u} \quad (4.9)$$

where

$$\mathbf{M} = \begin{pmatrix} 0 & \frac{\lambda k}{\lambda + 2\mu} & \frac{1}{\lambda + 2\mu} & 0 \\ -k & 0 & 0 & \frac{1}{\mu} \\ -\rho\omega^2 & 0 & 0 & k \\ 0 & X & -\frac{\lambda k}{\lambda + 2\mu} & 0 \end{pmatrix} \quad (4.10)$$

with

$$X = -\rho\omega^2 + k^2 \left(\lambda + 2\mu - \frac{\lambda^2}{\lambda + 2\mu} \right). \quad (4.11)$$

The system given by (4.9) governs the propagation of the disturbance anywhere in the medium once it is initiated.

4.2.2 The Solution In Homogeneous Media

There are two good reasons to seek first the solutions of system (4.9) in a homogeneous medium, i.e. one having λ, μ, ρ constant. First, as it was already explained, the source acts in an homogeneous sublayer and therefore, until the motion reaches the upper or lower boundary of this sublayer, the disturbance coincides with the solution in a homogeneous space having the same Lamé constants and density. Second, the half-space is assumed to be homogeneous and the integration process starts with the components of solutions in the half-space taken as initial values.

It is well known (Coddington and Levinson, 1987) that the solutions of a differential system with constant coefficients are of the form

$$Ce^{\eta z} \quad (4.12)$$

with η equal to any simple eigenvalue of the system, the constant coefficient C being in general different for each component and all the coefficients being determined up to a multiplicative factor.

The eigenvalues of system (4.9) are obtained from

$$\det(\mathbf{M} - \mathbf{I}\eta) = 0 \quad (4.13)$$

where \mathbf{I} is the unit matrix of order (4×4) . As expected, these eigenvalues are equal to $\pm K_\alpha, \pm K_\beta$, where

$$K_\alpha = \sqrt{k^2 - \frac{\omega^2}{\alpha^2}} \quad , \quad K_\beta = \sqrt{k^2 - \frac{\omega^2}{\beta^2}} \quad . \quad (4.14)$$

The square roots of the eigenvalues are defined uniquely as:

$$K_\alpha = \begin{cases} \sqrt{k^2 - \frac{\omega^2}{\alpha^2}} & \text{if } k > \left| \frac{\omega}{\alpha} \right| \\ i \sqrt{\frac{\omega^2}{\alpha^2} - k^2} & \text{if } k < \left| \frac{\omega}{\alpha} \right| \end{cases} \quad (4.15)$$

and K_β takes the same definition with α replaced by β . Physically, K_α and K_β correspond to downgoing P - and S -waves while the negative counterparts denote upgoing components.

The corresponding eigenvectors are:

$$\mathbf{u}_\pm^{(\alpha)}(z) = \begin{pmatrix} \pm K_\alpha \\ k \\ (\lambda + 2\mu) K_\alpha^2 - \lambda k^2 \\ \pm 2\mu k K_\alpha \end{pmatrix} e^{\pm K_\alpha z} \quad (4.16A)$$

and

$$\mathbf{u}_\pm^{(\beta)}(z) = \begin{pmatrix} k \\ \pm K_\beta \\ \pm 2\mu k K_\beta \\ (K_\beta^2 + k^2) \mu \end{pmatrix} e^{\pm K_\beta z} \quad (4.16B)$$

4.2.3 The Boundary Conditions

In the inhomogeneous layer, i.e. for

$$0 < z \leq H$$

a closed analytical solution to system (4.9) only exists in particular cases. In general, we can represent the solution only formally in a closed form, e.g. by using propagator matrices, as these matrices are known to exist but there are no closed expressions for them, e.g. finite combinations of quadratures. One way to overcome this difficulty is to replace the inhomogeneous layer by a stack of sublayers for which such closed forms exist, e.g. by a stack of homogeneous sublayers. This is the approximation used when applying the Thomson-Haskell method (Thomson, 1950; Haskell, 1953), in one of its variants (see Aki and Richards, 1980 and Kennett, 1983 for references). An alternative way is to integrate numerically system (4.9) using an accurate and stable numerical scheme. This alternative has been used successfully in order to calculate dispersion curves and transfer functions by Abramovici (1968a and b). The basic idea, used with any approach, is to integrate from the bottom interface up, i.e. from $z = 0$ to $z = H$ in the coordinate system chosen here. Taking as initial values at $z = 0$, the components of either $\mathbf{u}^{(\alpha)}$ or $\mathbf{u}^{(\beta)}$ in the half-space and integrating upwards, we obtain solutions $\mathbf{u}^{(\alpha)}$ and $\mathbf{u}^{(\beta)}$ in the entire structure (i.e., for $-\infty < z \leq H$) that satisfy the radiation condition. The components of $\mathbf{u}^{(\alpha)}$ and $\mathbf{u}^{(\beta)}$ at each interface, $z = z_j$ are used as initial values for a further integration for $z_j < z \leq z_{j+1}$. In this manner the solutions $\mathbf{u}^{(\alpha)}$ and $\mathbf{u}^{(\beta)}$ in the structure are continuous at the interfaces, thus satisfying all the required boundary conditions. The same is true for any linear combination

$$C_\alpha \mathbf{u}^{(\alpha)} + C_\beta \mathbf{u}^{(\beta)} \quad (4.17)$$

with coefficients C_α and C_β being arbitrary functions of ω and k and also for any superposition (discrete or continuous) of such linear combinations. The values of the coefficients determine the amount of contribution of each wave type to the response for each $(\omega-k)$ pair. By choosing a particular set of coefficients and a particular superposition, one is able to satisfy the conditions related to the presence of the source.

4.2.4 The Source

It is well known (Ewing, Jardetsky, Press, 1957) that the displacement and stress components of a homogeneous space generated by a point-source of P -waves located at $r = 0, z = z_s$ (in cylindrical coordinates) are derived from a potential

$$\phi = -\frac{V_o}{4\pi R} g\left(t - \frac{R}{\alpha}\right) \quad (4.18)$$

where $R = [r^2 + (z - z_s)^2]^{1/2}$ is the distance from the observation point to the source, V_o is the volume generated at the source in one second and g , as above, characterizes the time-dependence of the source, being equal to zero for $t < 0$.

The potential ϕ can be expressed as a Fourier-Bessel double integral

$$\phi = -\frac{V_o}{4\pi^2} \operatorname{Re} \int_0^\infty \hat{g}(\omega) e^{i\omega t} d\omega \int_0^\infty k \varphi(k) J_0(kr) dk \quad (4.19)$$

where

$$\varphi(k) = \frac{e^{-K_\alpha |z - z_s|}}{K_\alpha}, \quad (4.20)$$

$\hat{g}(\omega)$ is the Fourier transform of $g(t)$ and Re stands for "real part".

Taking the gradient and using Hooke's law, it is found that the displacement-stress

vector (Abramovici, 1990) for a P -source in a homogeneous space is as follows:

$$\mathbf{U}_{\text{source}} = \text{Re} \int_0^\infty d\omega \int_0^\infty \mathbf{D} \mathbf{u}_{\text{source}}^{(\alpha)} dk \quad (4.21)$$

where

$$\mathbf{u}_{\text{source}}^{(\alpha)} = \frac{V}{2K_\alpha} \begin{cases} \mathbf{u}_-^{(\alpha)}(z - z_s) & \text{if } z > z_s \\ \mathbf{u}_+^{(\alpha)}(z - z_s) & \text{if } z < z_s \end{cases}, \quad (4.22)$$

$$V = \frac{V_0 \hat{g}(\omega)}{2\pi^2}, \quad (4.23)$$

and $\mathbf{u}_\pm^{(\alpha)}$ are given by (4.16A). The Lamé parameters and density are those corresponding to the sublayer containing the source.

Once the displacement-stress vector $\mathbf{u}_{\text{source}}^{(\alpha)}$ due to the source in a homogeneous space is found, its value at the interface defining the source sublayer can be used to find numerically the source solution denoted as \mathbf{u}_s in the entire inhomogeneous layer: we integrate from $z = z_{j_s}$ downwards and from $z = z_{j_s+1}$ upwards where the source sublayer is defined by $z_{j_s} < z \leq z_{j_s+1}$. This vector function, \mathbf{u}_s , satisfies system (4.9), the source conditions and all the boundary conditions at interfaces. Since it is assumed that the receivers are at the free surface, the initial values for the system (4.9) due to the source are explicitly given by the first expression of (4.22) for $z > z_s$.

4.2.5 The Free Surface Conditions and the Solutions

In order to satisfy the boundary conditions at the top surface, we add the source

solution, defined above, to the general solution (4.17) of system (4.9),

$$\mathbf{u} = C_\alpha \mathbf{u}^{(\alpha)} + C_\beta \mathbf{u}^{(\beta)} + \mathbf{u}_s \quad (4.24)$$

and determine the constants C_α and C_β so that the stress components vanish for $z = H$:

$$\begin{aligned} C_\alpha T_w^{(\alpha)} + C_\beta T_w^{(\beta)} + T_{ws} &= 0 \\ C_\alpha T_q^{(\alpha)} + C_\beta T_q^{(\beta)} + T_{qs} &= 0 \end{aligned} \quad (4.25)$$

Performing the needed algebra and going back to the ω - k integrals, one finds the following expression for the displacement components at the free surface, $z = H$ (Abramovici, 1968b and 1990):

$$\begin{aligned} s_z &= \frac{V_0}{2\pi^2} \operatorname{Re} \int_0^\infty \hat{g}(\omega) e^{i\omega t} d\omega \int_0^\infty J_0(kr) \left[k \frac{(T_w)_s G \begin{pmatrix} 1 & 4 \\ 1 & 2 \end{pmatrix} - (T_q)_s G \begin{pmatrix} 1 & 3 \\ 1 & 2 \end{pmatrix}}{G \begin{pmatrix} 3 & 4 \\ 1 & 2 \end{pmatrix}} - kw_s \right] dk \\ s_r &= -\frac{V_0}{2\pi^2} \operatorname{Re} \int_0^\infty \hat{g}(\omega) e^{i\omega t} d\omega \int_0^\infty J_1(kr) \left[k \frac{(T_w)_s G \begin{pmatrix} 2 & 4 \\ 1 & 2 \end{pmatrix} - (T_q)_s G \begin{pmatrix} 2 & 3 \\ 1 & 2 \end{pmatrix}}{G \begin{pmatrix} 3 & 4 \\ 1 & 2 \end{pmatrix}} - kq_s \right] dk \end{aligned} \quad (4.26)$$

where $G \begin{pmatrix} m & n \\ 1 & 2 \end{pmatrix}$ is the second-order minors formed by rows m and n and columns 1 and 2 from the matrix

$$\mathbf{G} = (\mathbf{u}^{(\alpha)}, \mathbf{u}^{(\beta)}) \quad (4.27)$$

Here, the quantities within the brackets, [...], in (4.26) include the effect of transmission and reflection at the interfaces and are referred to as the *reflectivity functions*, $\tilde{S}_n(\omega, k, z_s)$ where $n=0$ is the vertical component and $n=1$ is the horizontal component.

4.2.6 The Second-Order Minors

Straightforward algebraic manipulation leads to the solution of the displacement components which has terms involving subtraction of products of elements from the solution u of the fourth-order differential system (4.9). The algorithm derived from direct implementation of the equations thus obtained has been found to be highly unstable since, at high frequencies, the elements become very large and accuracy is reduced after subtraction due to loss of significant digits. This numerical difficulty caused by loss significant digits when large or small numbers exist has been studied extensively by researchers such as Knopoff (1964a), Dunkin (1965), Gilbert and Backus (1966) and recently by Franssens (1983) and Kundu and Mal (1985). It is possible to avoid the inaccuracies due to possible cancellations occurring when adding and subtracting products. The proposed remedy to the problem, which involves the concept of subdeterminants or minors, is to calculate these terms directly from a higher order differential system. The version that will be used is attributed to Gilbert and Backus (1966). These minors, $G \begin{pmatrix} m & n \\ 1 & 2 \end{pmatrix}$, can be obtained directly by integrating numerically the sixth-order differential system from the top of the half-space to the free surface, $z = \bar{H}$ (Abramovici, 1968a and b; Abramovici, Le and Kanasewich, 1990):

$$\frac{d\Gamma}{dz} = \Omega\Gamma \quad (4.28)$$

where

$$\Gamma = \begin{bmatrix} G\left(\begin{smallmatrix} 1 & 2 \\ 1 & 2 \end{smallmatrix}\right) \\ G\left(\begin{smallmatrix} 1 & 3 \\ 1 & 2 \end{smallmatrix}\right) \\ G\left(\begin{smallmatrix} 1 & 4 \\ 1 & 2 \end{smallmatrix}\right) \\ G\left(\begin{smallmatrix} 2 & 3 \\ 1 & 2 \end{smallmatrix}\right) \\ G\left(\begin{smallmatrix} 2 & 4 \\ 1 & 2 \end{smallmatrix}\right) \\ G\left(\begin{smallmatrix} 3 & 4 \\ 1 & 2 \end{smallmatrix}\right) \end{bmatrix}, \quad (4.29)$$

$$\Omega = \begin{bmatrix} 0 & 0 & \xi & -\nu & 0 & 0 \\ 0 & 0 & k & \lambda\nu & 0 & 0 \\ X & -k\lambda\nu & 0 & 0 & k\lambda\nu & \nu \\ \rho\omega^2 & -k & 0 & 0 & k & -\xi \\ 0 & 0 & -k & -k\lambda\nu & 0 & 0 \\ 0 & 0 & -\rho\omega^2 & -X & 0 & 0 \end{bmatrix}, \quad (4.30)$$

where

$$\nu = \frac{1}{\lambda + 2\mu}, \quad \xi = \frac{1}{\mu} \quad (4.31)$$

and X is given by (4.11). The initial values at $z = 0$ are :

$$\Gamma_{z=0} = \begin{bmatrix} K_\alpha K_\beta - k^2 \\ k \{ 2\mu_0 K_\alpha K_\beta - (2\mu_0 k^2 - \rho_0 \omega^2) \} \\ -\omega^2 \rho_0 K_\alpha \\ \omega^2 \rho_0 K_\beta \\ -k \{ 2\mu_0 K_\alpha K_\beta - (2\mu_0 k^2 - \rho_0 \omega^2) \} \\ (2\mu_0 k^2 - \rho_0 \omega^2)^2 - 4k^2 \mu_0^2 K_\alpha K_\beta \end{bmatrix} \quad (4.32)$$

where λ , μ , ρ as well as the P - and S -wave velocities are those of the homogeneous half-space and the square roots for K_α and K_β are defined by (4.14) and (4.15).

4.3 Numerical Considerations and Computational Methods

The computation of the two displacement components given by (4.26) is achieved, in our approach, by integrating first the k -integral in the general form

$$S(r, z=H, \omega) = (-1)^n \int_0^\infty J_n(kr) \tilde{S}_n(\omega, k, z_s) dk \quad (n = 0, 1) \quad (4.33)$$

and then inverting the spectral result after being modified by the source function into the time domain by means of an inverse fast Fourier transform. This is usually known in the literature as *spectral method* (Frazer, 1988). The code is implemented in double precision using FORTRAN 77 on a parallel machine, *Myrias SPS-2*, with 64 processors in the following way:

```

PAKDO over frequency
  DO over k
    calculate  $\tilde{S}_n(\omega, k, z_s)$ 
  ENDDO
ENDPARDO .

```

The PARDO-loop structure which is the analogue to the DO-loop structure in Fortran, converts a sequential iteration into a parallel series of tasks in the Myrias's environment (Myrias, 1989). Other seismic applications in Myrias *SPS-2* have been reported by

Kapotas (1990).

Figure 4.2 shows a flow-chart of the computer code. Note that the reflectivity functions, which are dependent on the model and source location, are calculated in parallel for all the frequencies. The reason that the Bessel functions are left out at this stage is that they are the only factor depending upon the layout of the receivers. Therefore, one can use the calculated reflectivity functions for all receivers in a horizontal array, without redoing the calculation. A synthetic section for any receiver's configuration can later be assembled by multiplying the ω - k series with Bessel functions having appropriate offset argument. The Bessel functions are computed with an accuracy up to seven digits by the polynomials provided by Abramowitz and Stegun (p. 369-370, 1965). For illustrative purposes, a theoretical model was used to generate some intermediate results.

4.3.1 The Theoretical Model

The theoretical model (Pekeris et al., 1965) consists of a homogeneous elastic layer, 1 km thick, overlaying a homogeneous elastic half-space, having rigidity μ_o equal to twice the rigidity μ_l of the layer, both media satisfying the Poisson's hypothesis $\lambda = \mu$. The S -wave velocity, β_o in the half-space is assumed to be 10% higher than that of the layer β_l :

$$\beta_o = 1.1\beta_l .$$

$Q_\alpha = Q_\beta = 1000$ were employed to simulate the elastic result using the ω - k method. All the quantities were non-dimensionalized with the scale factors for length, density and velocity being H km, 6000 kg/m³ and 10 km/s respectively.

4.3.2 The Numerical Integration of the Differential Systems

For every model and source location, the main computational effort is to find the propagated displacement-stress vector and 2nd order minors at each level, for any pair

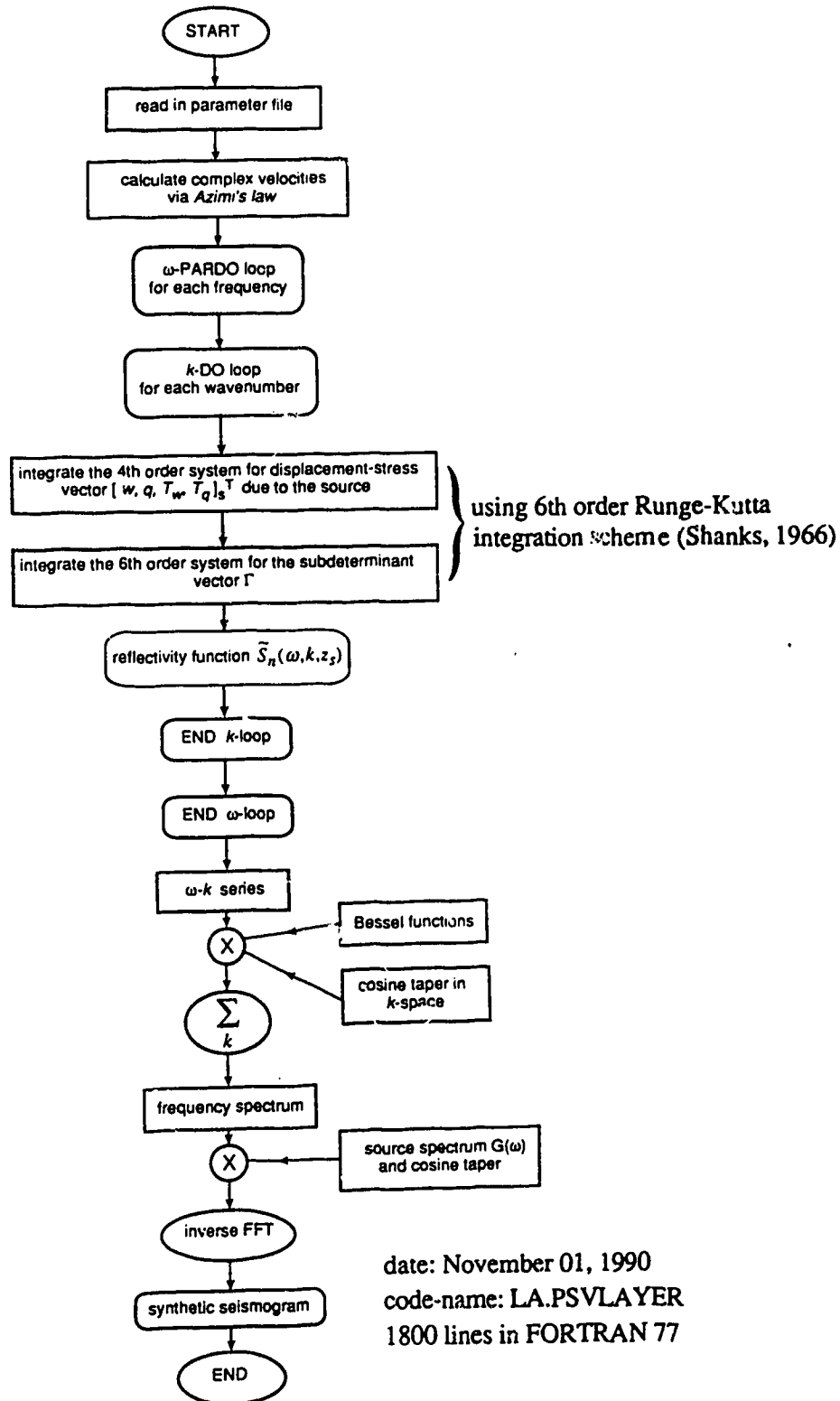


Figure 4.2: A flow-chart of the computer code LA.PSVLAYER.

(ω, k) , thus composing the reflectivity functions, $\tilde{S}_n(\omega, k, z_s)$. For small k , at least one of the square roots K_α or K_β is imaginary, even in the elastic case [see equation (4.15)]. Hence, the differential systems to be integrated have complex solutions, although the independent variable is real. Moreover, anelastic structures are considered with anelasticity being introduced via Azimi's law (Section 3.4; Aki and Richards, 1980; Abramovici, Le and Kanasewich, 1990), so that the coefficients of the differential system are also complex. As a result, systems of equations of orders eight and twelve have to be integrated respectively over a real independent variable.

Even though many multi-step schemes are used in practice to solve the initial value systems (4.9) and (4.28), a one-step scheme has been implemented as these are self-starting and always stable (Isaacson and Keller, 1966). A great advantage is that this approach allows handling inhomogeneous sublayers (like transition layers with linear variation of seismic velocities) in a straightforward manner rather than by dividing them into homogeneous sublayers. The fact that the ease of analyzing the truncation error and high accuracy can be easily obtained by reducing the stepsize also contributed to our decision of using a one-step scheme. The only disadvantage of a one-step scheme is the high number of evaluations per step. Some experiments were carried out with a set of Runge-Kutta methods of orders between 2 and 8 included in a package built originally for calculating phase velocities and transfer functions (Abramovici, 1968c) and used subsequently in electromagnetic wave propagation (Abramovici, 1974; Abramovici and Chlamtac, 1978). It was found that, for the purpose of the present study, the wanted accuracy is obtained using a sixth-order scheme involving six intermediate evaluations (Shanks, 1966), which is the minimum number of evaluations for this order. The step size used for all the results given in Chapter 5 was 0.004.

The difficulty also encountered by others (Schwab and Knopoff, 1970; Phinney et al., 1987) when using the Thomson-Haskell based algorithm is the overflow problem

associated with the elements of the solution (4.29) of the sixth-order system. However, this overflow problem can be easily eliminated by normalizing all the elements by the magnitude of the largest one which exceeds a threshold value set at 10^7 .

4.3.3 The k -Integral

Since $\tilde{S}_n(\omega, k, z_s)$ is a rational function for perfectly elastic medium, the function has singularities which prohibit straightforward numerical integration of the k -integral along the nonnegative real axis unless some appropriate integration contour transformation is taken. These singularities represent surface wave poles. These poles represent the slownesses of the free oscillations of the system. There is always a finite number of them but their positions change and their number increases with frequency. In order to circumvent the difficulty many techniques have been suggested. Kundu and Mal (1985) applied the theory of residues to remove the poles for idealized elastic structures. Phinney (1965) suggested the use of complex frequency $\omega = \omega_r - i\omega_I$ with a small positive imaginary part, ω_I to smooth the k -spectrum and the smoothing effect was then removed by multiplying the result by the exponential $\exp(\omega_I t)$ in temporal domain. Since it is a common observable fact that energy dissipates as wave propagates into the Earth (Knopoff, 1964b and Sato, 1967), the poles are removed in our case by introducing anelasticity into the medium to make velocities complex through Azimi's law (Section 3.4). In the presence of attenuation, the singularities are moved into the fourth quadrant of the complex $(k + i\delta)$ -plane away from the real k -axis.

A typical behavior of the reflectivity functions for the theoretical model can be seen in Figure 4.3, where the real parts of the functions are presented for three source locations and four different frequencies, two lower and two higher ones. The arrows point to the location of the real parts of the branch points for the square roots K_α and K_β , i.e. to the slownesses of the P - and S -waves in the half-space and layer respectively, multiplied by

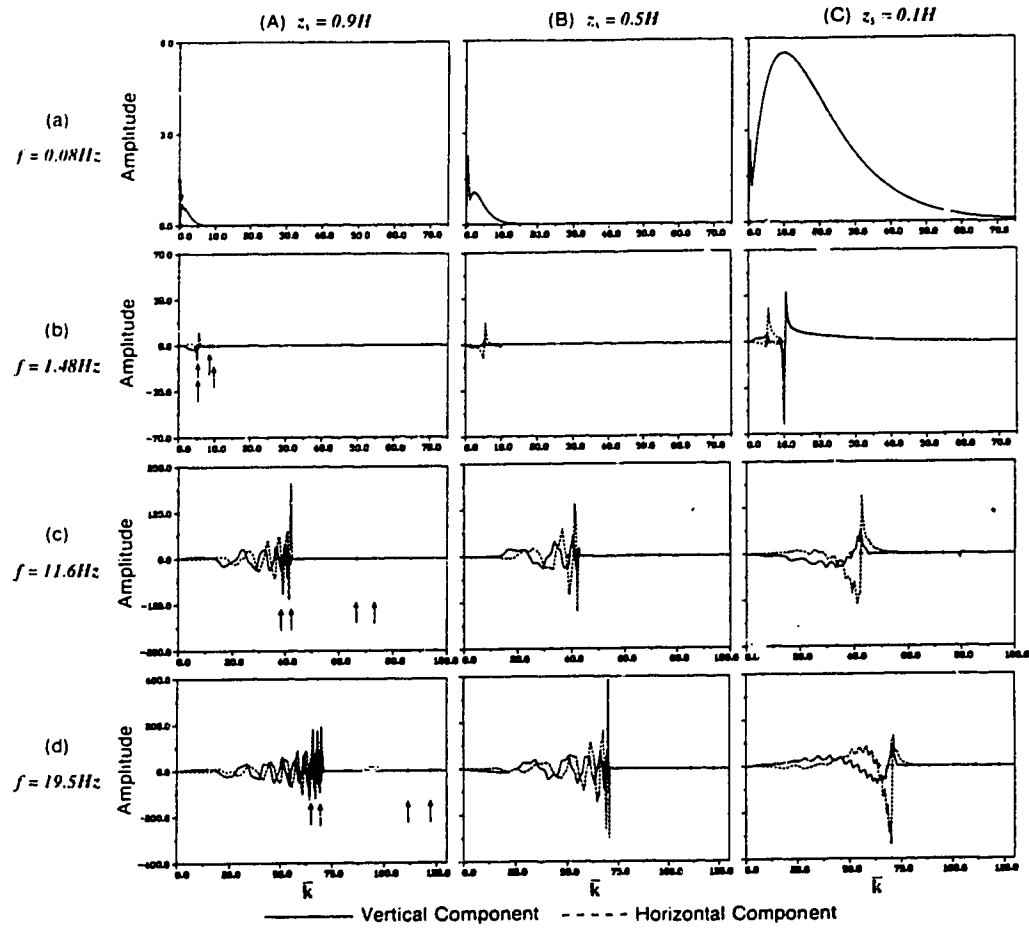


Figure 4.3: Plots of the real parts of the reflectivity functions at three different source depths and four different frequencies for the theoretical model. The same source depth is used along the column and the same frequency applies along row. The arrows point to the location of the real parts of the branch points for the square roots K_α and K_β . The first two are from the P -wave velocities and the last two are from the S -wave velocities.

the corresponding angular frequency. The rows show the functions for a fixed frequency, while the columns show them for a fixed source location. Even though the poles are located away from the real k -axis for anelastic media, their presence in the proximity of the integration path is felt strongly. As a result, one needs to increase the number of integration points to cover the highly-oscillating portion of the integrand.

Another numerical problem that must be solved in calculating the k -integral is the fact that the integration interval extends to infinity. However, in practice, a finite range of k -values is required only. As a general pattern in Figure 4.3, it is seen that with increasing frequency the integrand becomes more oscillatory. For higher frequencies the magnitude of the functions is governed by the slowness of the P -wave in the layer; a little past this point on the k -axis, the functions decay exponentially. For very low frequencies (0.08 Hz in Figure 4.3a) and a near-surface source (Figure 4.3C), Rayleigh energy dominates and the functions decay at a much higher value for k , which is expected from the known properties of Rayleigh waves (Ewing, Jardetsky and Press, 1957). Taking into account the described behavior, the effective k -interval $[0, k_{\max}]$, for which the internal integral is calculated, is determined in each case. The application of k_{\max} is equivalent to using a high-pass velocity-filter which eliminates events with apparent velocities slower than c_{\min} ($c_{\min} = \omega / k_{\max}$).

After being modified by the Bessel factors, the integrand becomes extremely oscillatory, especially for large offset. Adequate sampling is necessary to track the highly-oscillating portion of the integrand. A Filon scheme has long been used to evaluate integral involving highly varying function (Davis and Rabinowitz, 1984). Recently, Frazer and Gettrust (1984) and Frazer (1988) employed a modified version of Filon's scheme to evaluate a slowness integral similar to equation (4.33). Xu and Mal (1985) also suggested an adaptive Clenshaw-Curtis quadrature scheme. However, in our approach the range was divided into three or four subintervals and within each a Romberg scheme (Henrici, 1964)

of 513 points was used, thus resulting in a long k -series. Abrupt truncation of the k -series would give rise to wraparound events in r -space. In order to avoid this, the k -series was also cosine-tapered. As for each integration point one has to perform the above described Runge-Kutta process; therefore, the total computer time needed for all the 512 frequencies became forbiddingly high for an ordinary scalar or vector computer, no matter how powerful it is. The total CPU time for one model was no less than 2 hours on the Myrias SPS-2 system with 513 processors but $(2 * 512/64)$ hours with only 64 processors and the disk space required was more than 20 Megabytes in binary format.

4.3.4 The ω -Integral

Bouchon (1979) and Mallick and Frazer (1987) have also suggested the use of complex frequency, $\omega = \omega_r - i\omega_i$ with a small positive imaginary part, ω_i to attenuate aliasing in the time domain. Aliasing occurs in two cases: (1) when the frequency increment, Δf used is too coarse and (2) when the maximum frequency content f_{\max} , of the synthetic signal is larger than the Nyquist frequency. Since Δf [$\Delta f = 1/(2n\Delta t) = 1/2T$ where n is the number of frequency samples] determines the time window T , strong events which arrive outside T will then appear at the wrong location. In the complex-frequency approach, energy from times greater than T will be damped by $\exp(-\omega_i T)$. Here question arises as to choosing the appropriate size of the imaginary part and these authors have suggested some values. In our approach, a conservative way was followed by acquiring a long ω -series of 513 points using finer Δf so as to make T bigger. A cosine-taper was used to eliminate the contribution from frequencies higher than the Nyquist limit. However, by doing this one restricts the use of high frequency source since the combination of using large f_{Nyquist} and fine Δf will require more than 513 frequency points to make a proper size of time window in temporal space to include all the significant arrivals.

CHAPTER 5

SEISMOGRAMS USING THE ω - k INTEGRALS FOR A POINT P-SOURCE IN A VERTICALLY INHOMOGENEOUS ANELASTIC MODEL: NUMERICAL RESULTS

5.1 The Theoretical Model

In order to demonstrate that the proposed numerical approach and algorithms have been formulated correctly, a theoretical model, given in Section 4.3.1, is considered for which accurate calculations have been performed using the Cagniard-Pekeris-de Hoop method (Abramovici, 1970 – hereafter referred to as the A-paper). For comparative purposes, a triangular time-variation for the source is used (Figure 5.1a),

$$g(t) = \begin{cases} 0 & \text{for } t \leq 0, t \geq 2\Delta \\ \frac{t}{\Delta} & \text{for } 0 \leq t \leq \Delta \\ \frac{2\Delta - t}{\Delta} & \text{for } \Delta \leq t \leq 2\Delta \end{cases} \quad (5.1)$$

having a Fourier transform (Figure 5.1b),

$$\hat{g}(\omega) = \frac{\sin^2\left(\frac{\omega\Delta}{2}\right)}{\left(\frac{\omega\Delta}{2}\right)^2} e^{i\omega\Delta} \quad (5.2)$$

The parameter Δ controls the width of the pulse and was 0.1 in this experiment.

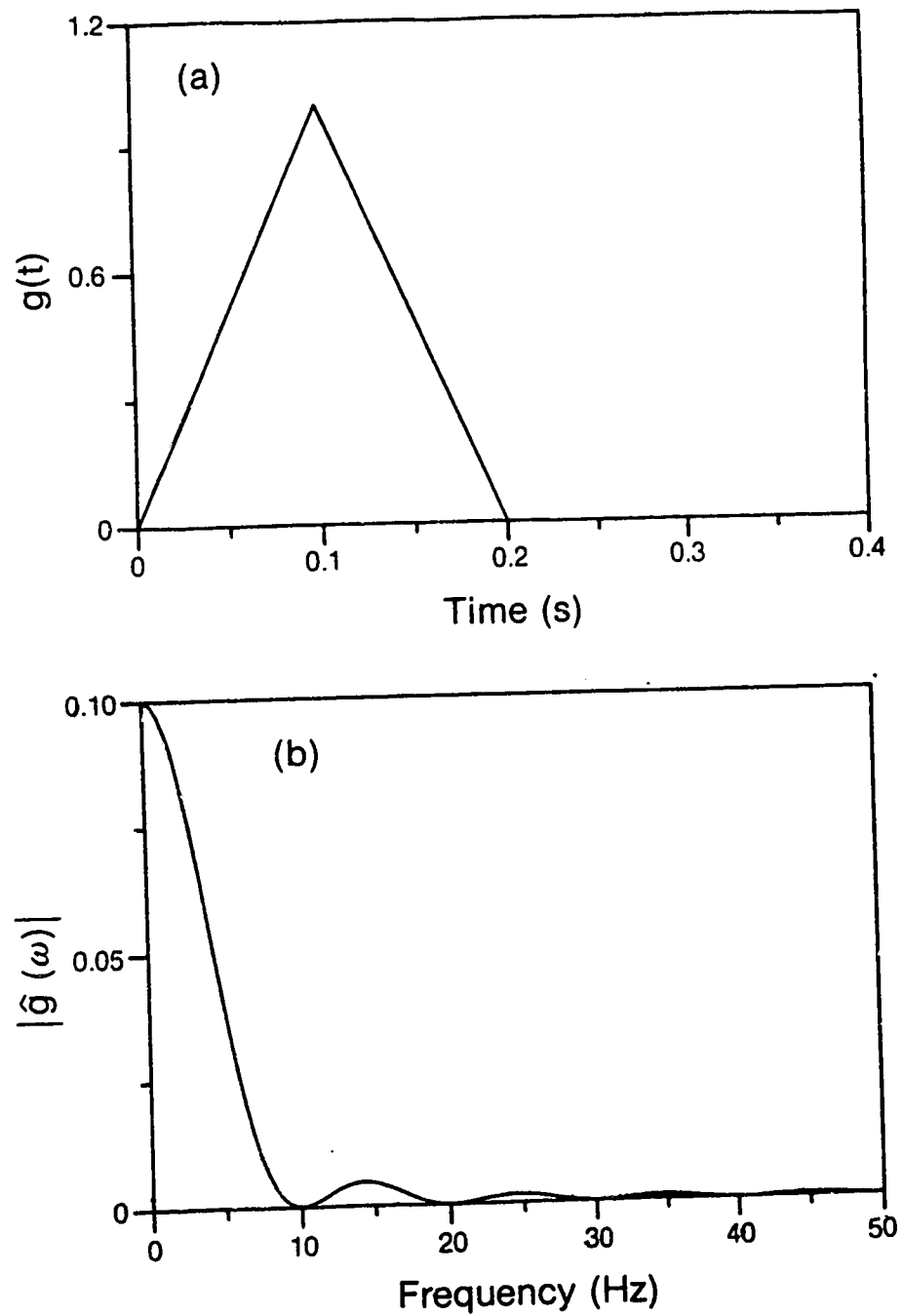


Figure 5.1: The triangular pulse with $\Delta = 0.1$: (a) the time-variation and (b) the Fourier spectrum.

This time function is very similar, but not identical, with the one used in the A-paper. There, the source was defined using the potential for the P -waves, the time-variation of which was a Heaviside function with "rounded shoulders" having quadratic time-variation. As a result, the displacement approached a triangular time-function only in the far-field. As seen in Figure 5.1b, most of the energy is concentrated within a narrow band 0-10 Hz, with very small side lobes. Outside this range, the pulse has a dominant DC value, the integrand being zero at zero frequency. The low frequency end might create difficulties in the fast Fourier transform inversion to the time-domain (which is how we performed the ω -integral), due to its sharp edge. However, no low-cut cosine tapering was applied at this end since it would have reduced significantly the energy content of the signal, especially that of the Rayleigh wave (Helmberger, 1968). Each seismogram was calculated in the frequency range 0-30 Hz and multiplied by a cosine taper (0/0/25/30 Hz) in order to minimize high frequency integration noise. For the deeper sources with $z_s = 0.5H$ and $z_s = 0.9H$, we took $k_{\max} = b_\alpha + 25$ where b_α is the P -wave slowness in the layer multiplied by the corresponding angular frequency, whereas for the shallow source at $z_s = 0.1H$, we took $k_{\max} = b_\alpha + 75$. In order to avoid spatial aliasing, we applied also the following cosine tapers: (0/0/ $b_\alpha + 15$ / $b_\alpha + 25$) for the deeper sources and (0/0/ $b_\alpha + 60$ / $b_\alpha + 75$) for the shallower source. The finite k -interval was then divided into four subintervals.

Figures 5.2b-5.4b show synthetic seismograms calculated using the ω - k method for three different source depths at $r = 5H$. The corresponding numerical seismograms in the A-paper (Figures 3-5 in the A-paper and here referred to as 5.2a-5.4a) are also included for comparison. As one can see, it is difficult to identify each individual phase in these seismograms, which is also the case for those in the A-paper, e.g., on Figures 5.2a-5.4a. Instead, one identifies, as in the A-paper, four groups of rays of the form P_n , P_nS , P_nS_2 and P_nS_3 giving together the appearance of a characteristic oscillatory transient oscillation.

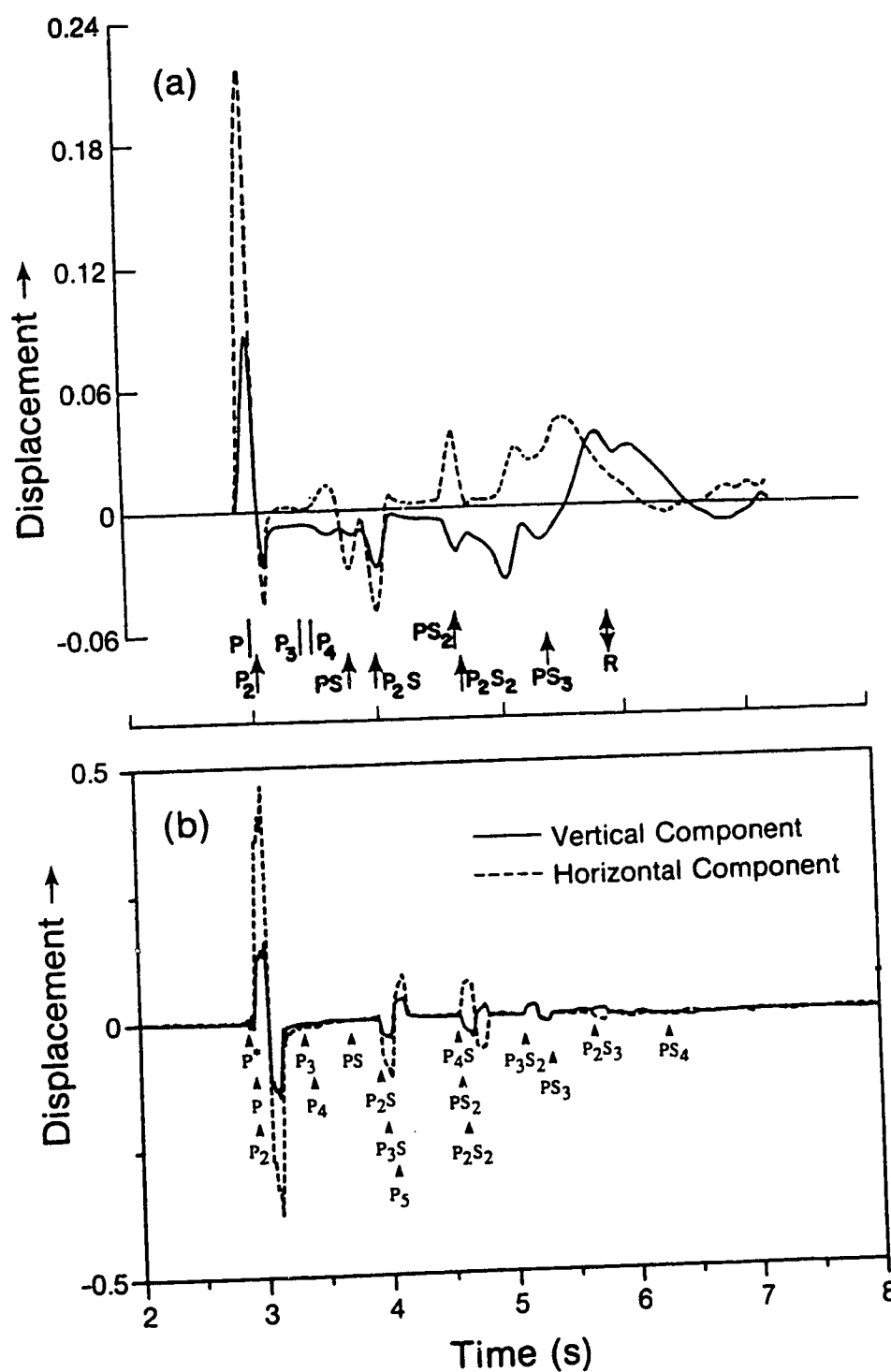


Figure 5.2: Comparison of synthetic seismograms obtained using two different methods: (a) the Cagniard-Pekeris-de Hoop method, (reproduced from the A-paper) (b) the ω - k method. The model is a 1 km-layer overlaying a half-space with $z_s = 0.9H$ and $r = 5H$. The arrows in (b) mark the arrival time of each phase while those in (a) are shifted by Δ .

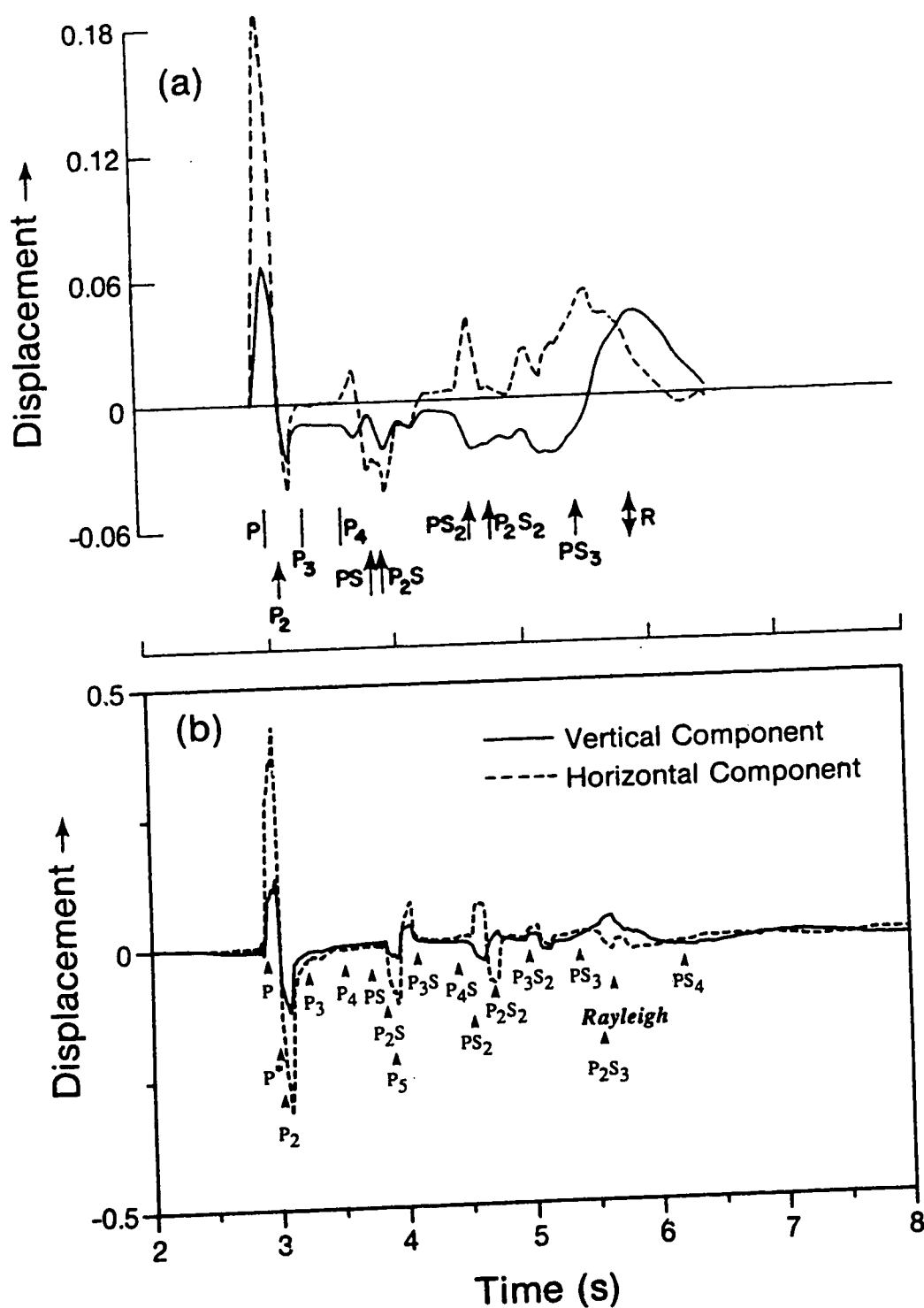


Figure 5.3: Comparison of synthetic seismograms obtained using two different methods: (a) the Cagniard-Pekeris-de Hoop method, (reproduced from the A-paper) (b) the ω - k method. The model is a 1 km-layer overlaying a half-space with $z_s = 0.5H$ and $r = 5H$. The arrows in (b) mark the arrival time of each phase while those in (a) are shifted by Δ .

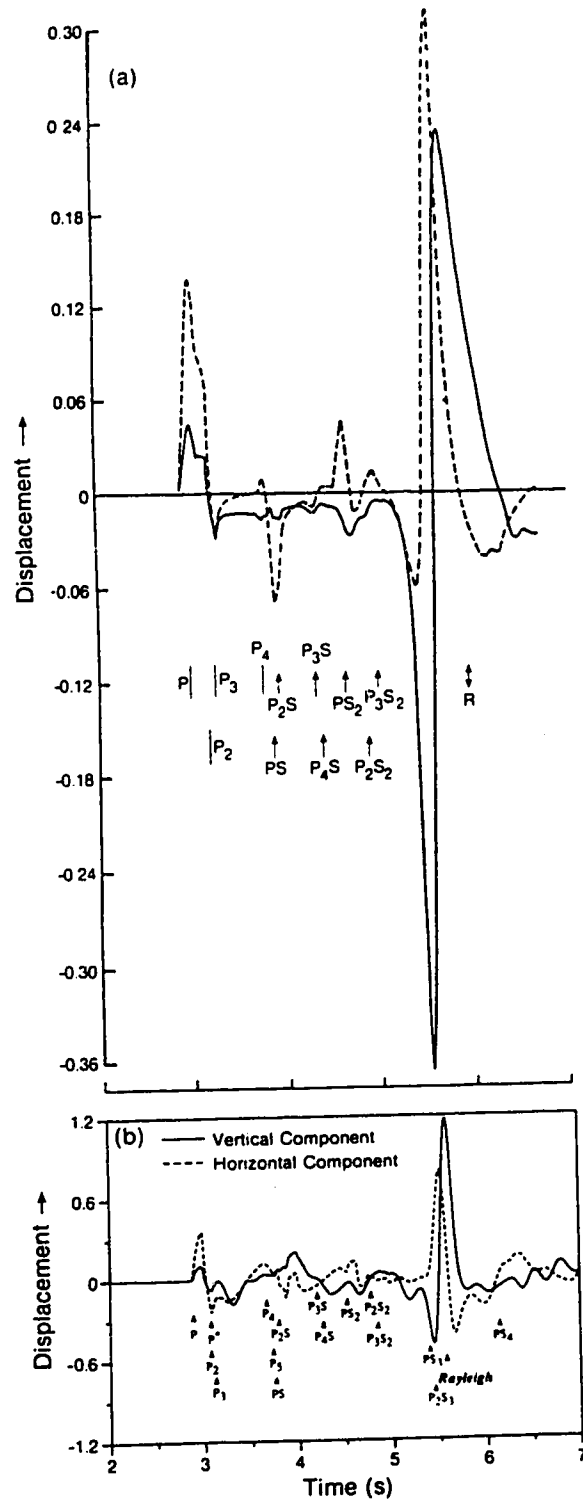


Figure 5.4: Comparison of synthetic seismograms obtained using two different methods: (a) the Cagniard-Pekeris-de Hoop method, (reproduced from the A-paper) (b) the ω - k method. The model is a 1 km-layer overlaying a half-space with $z_s = 0.1H$ and $r = 5H$. The arrows in (b) mark the arrival time of each phase while those in (a) are shifted by Δ .

The subscript denotes the type multiplicity. Another common characteristics of the ω - k seismograms and those based on the Cagniard-Pekeris-de Hoop method is the fact that the horizontal displacement has a larger amplitude than the vertical displacement, for the mentioned groups of body waves. For a source not near the surface, their shape is similar, except for polarity, which is sometimes the same and sometimes opposite. For a near-surface (Figure 5.4), the behavior of the horizontal displacement is not the same, at least in some time intervals. A marked difference between the ω - k seismograms and those in the A-paper is the total absence of the Rayleigh wave for the deep source in Figure 5.2b. For a source in the middle of the layer, the Rayleigh wave shows up (Figure 5.3b) and it is by far the main feature on the seismogram for a near-surface source (Figure 5.4b), similarly to what one sees in Figure 5.4a.

It should be noted that, from other studies (Ewing, Jardetsky and Press, 1957 and Lamb, 1904), the ω - k seismograms showed the more correct form of the relative amplitudes of vertical and horizontal components for Rayleigh waves. Both sets showed the same retrograde particle motion. There are other differences of a general character, between the ω - k seismograms and those in the A-paper, among them:

1. the ratios of the magnitudes of the positive and negative portions of similar waves or groups of waves are not the same, e.g., the negative oscillation at the arrival of P_2 is larger on the ω - k seismograms;
2. the oscillations in Figures 5.3b and 5.4b center around the zero-level, which is not the case with the oscillations on the corresponding Figures 5.3a and 5.4a;
3. the ratio of amplitudes of the horizontal and vertical displacements of the Rayleigh wave in Figure 5.4b is different from that in the corresponding Figure 5.4a.

There is no doubt that one of the reasons for the discrepancies between the numerical seismograms presented here and those in the A-paper is the difference in the time-variation of the source, mentioned in the previous section. There are, however, two

additional reasons. One is related to the fact that the models for the ω - k calculation contain a certain degree of anelasticity, while the calculation of the A-paper were done for purely elastic structures. Although a high Q ($Q = 1000$) was used to simulate structures of a similar nature, some differences should be present. Finally, the integrands are windowed both in wavenumber and frequency; as found from previous studies (Chapter 3), some filtering takes place as a result of applying cosine tapers.

Figure 5.5 shows a pair of synthetic displacement sections with true amplitude for the theoretical model having the source midway in the layer. Clipping has been applied to the negative amplitudes for plotting purpose. Converted waves and multiples are prominent and the Rayleigh wave is stronger vertically than horizontally as expected (Ewing, Jardetsky and Press, 1957). The decaying behavior of the waves is due to anelasticity and spherical spreading.

Taking into account the difference in the source function in the near field and the introduction of attenuation, it would appear that the current numerical results are a good representation of the displacement fields. Further tests would involve comparison with model experiments.

5.2 The Two-Layered Crustal Model

Figure 5.6 shows a parameter profile for a crustal model with two homogeneous layers over a homogeneous half-space and the synthetic velocity sections, with no exponential gain correction are shown in Figure 5.7. The source acts at 50 m below the surface and has a Gauss-type variation (Figure 2.3) with a dominant frequency of 5 Hz. The quality factors Q_α and Q_β are the same. The cosine taper $(0/0/(b_\beta)_s/(b_\beta)_s*1.05)$ was applied in the k -domain with four subintervals where $(b_\beta)_s$ is related to the S -slowness of the source layer. In the ω -domain, a cosine taper $(0/0/18/19.5\text{Hz})$ was used.

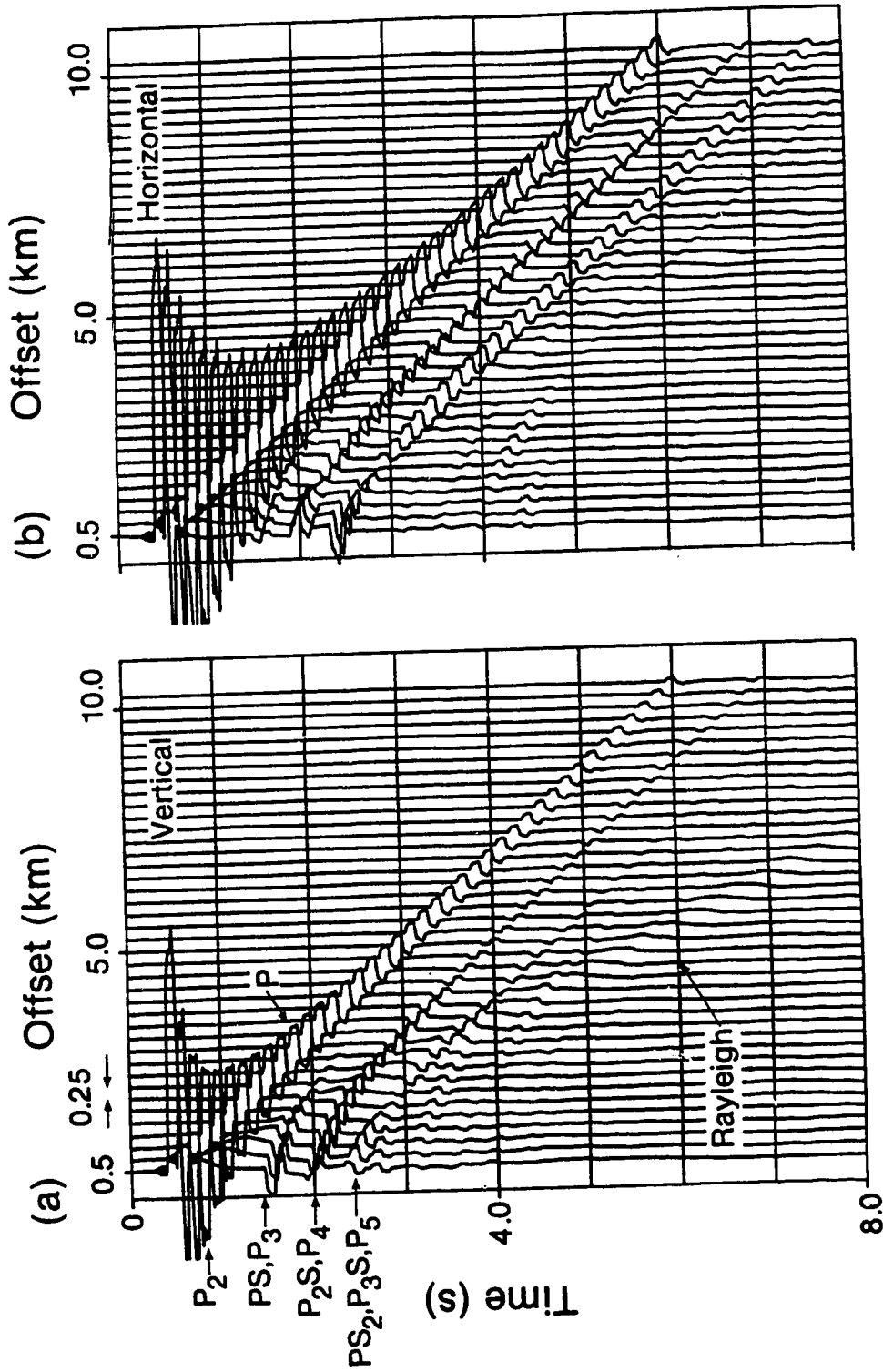


Figure 5.5: Synthetic displacement sections for a 1 km-layer model. The source is midway in the layer and has a triangular time-function: (a) vertical component and (b) horizontal component. The arrows point to the approximated locations of the indicated phases. The subscript denotes the type multiplicity.

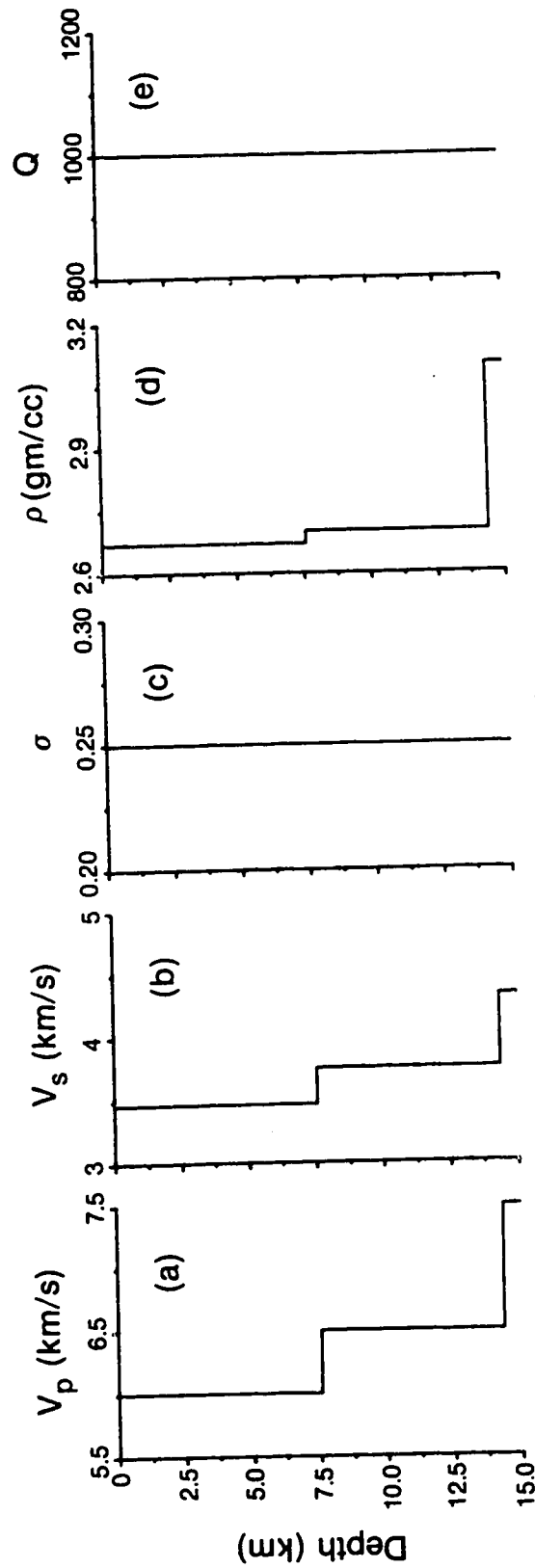


Figure 5.6: Parameter profiles for a two-layered crustal model. σ is the Poisson's ratio.

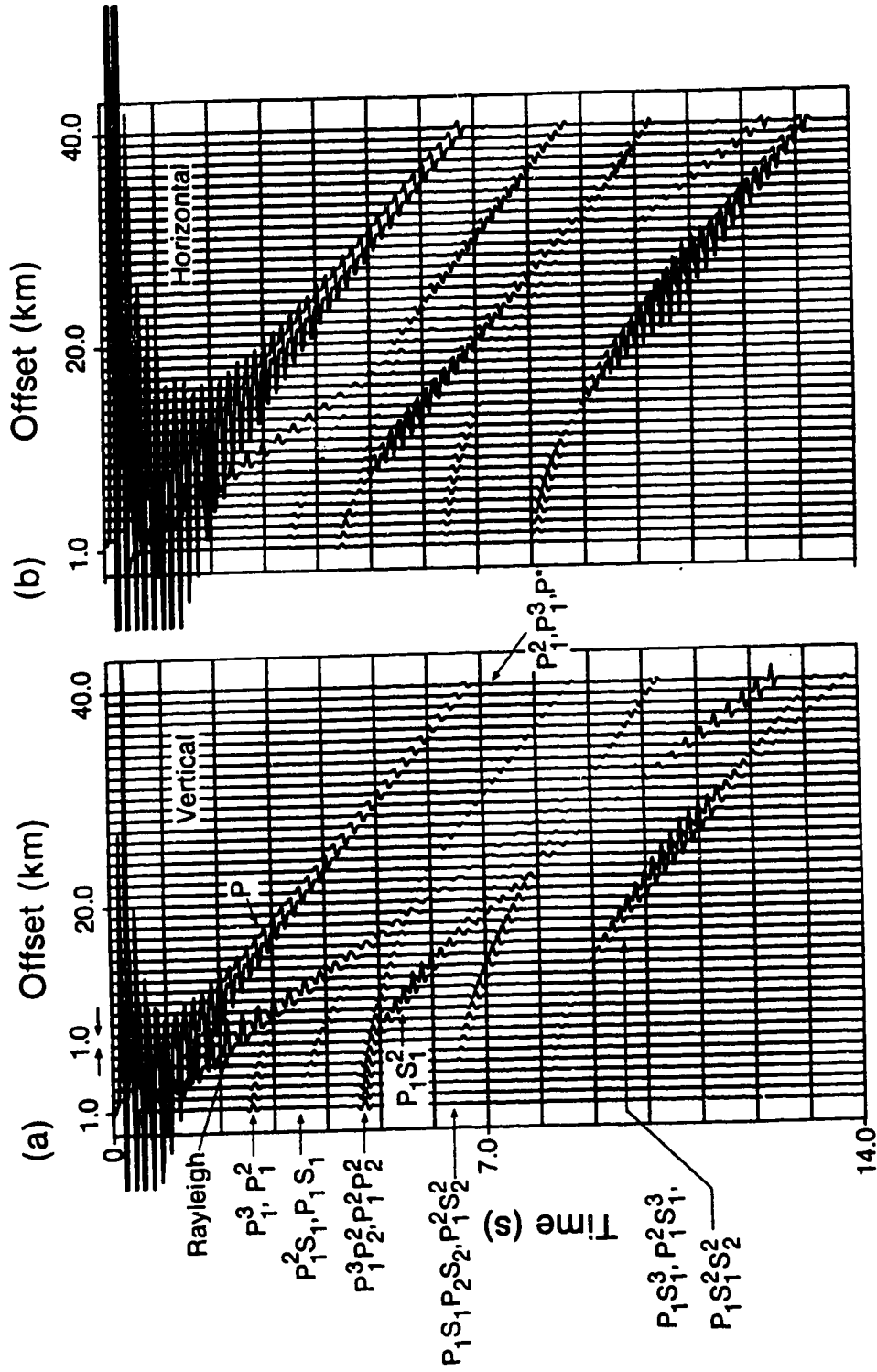


Figure 5.7: Synthetic velocity sections for a two-layered model. The source acts at 50 m below the surface and has a Gaussian time-variation: (a) vertical component and (b) horizontal component. The arrows mark the approximated arrivals of the indicated phases. The superscript denotes the multiplicity of the ray traversing the layer indicated by the subscript.

As discussed previously, it is difficult to identify the contribution of each individual phase, the seismogram being the result of superposition of all the arrivals within the calculated frequency-wavenumber window. The incident arrival preserves the shape of a Gaussian pulse, whereas the other arrivals come as a group say P_1^2 and P_1^3 , thus distorting the pulse shape. The head wave, P^* , is weak and comes approximately after 37 km. The high amplitude after 9.0 sec is contributed by at least three arrivals as indicated. The "ghost" arrival, $P_1S_1^2$, which travels from the source to the surface as P and reflects as S at the surface and the first interface, has significant amplitude especially on the horizontal component (Figure 5.7b) cutting across some of the major arrivals. Some residual Rayleigh energy is present, as the k -integral covers parts of the evanescent regime.

5.3 The Cold Lake Models

The Cold Lake deposit is one of Alberta's oil and tar sands resources in east-central Alberta. The crude bitumen deposits in this area are mostly confined within the lower Cretaceous Mannville group which is further subdivided into the McMurray, Clearwater and Grand Rapids formations. The target formation for most seismic experiments is the Clearwater formation, approximately 50 m thick and 450 m deep. The bitumen contained in the Clearwater formation contributes to about one-half of the total bitumen reserves at Cold Lake (Outtrim and Evans, 1977). A geological and geophysical description of the Cold Lake area has been given by Harrison et al. (1981) and Kanasewich (1983).

Current Enhanced Oil Recovery (EOR) techniques such as steam injection into the target zone, have become an integral part of the extraction of heavy oil. However, these conventional methods recover not more than one quarter of the original oil *in-situ*. Recently, open-pit mining, for high percentage recovery using modern mining techniques has been proposed. In any case, detailed reservoir mapping is essential for later

development, control and *in-situ* monitoring processes. In particular, one would like to determine the size, shape, location of the target zone and the preferred direction of growth of the steam front. For decades, remote sensing methods such as seismic reflection techniques have proved to be a very successful tool in delineating these features leading to improved oil extraction technique and more efficient and cost-effective field operations. The seismic method provides a higher degree of accuracy and resolution than are achieved by any other geophysical methods. This is so because the elastic wave has the shortest wavelength of any wave that can be observed after being modified by the Earth's system in its passage through Earth's structure and it experiences the least distortion and attenuation in waveform and amplitude.

In a study of *in-situ* attenuation of the Clearwater Formation using well-to-well seismic data by Macrides (1987), the value of Q_α was found to be as low as 10 in the steam-invaded zone due to mobilized bitumen of high temperature, and Poisson's ratio was as high as 0.4 due to steam condensation. Seismic amplitude, signatures and spectral character were also found to be significantly different in *pre-* and *post-steam* areas.

In the present study, computer simulations for the Cold Lake models are carried out for the following purposes: to study theoretically models with velocity gradient, thus checking the behavior of the algorithm, the response from finely-layered structure and the reflection response from the target zone due to small changes in velocity and density. In particular, one would like to study how Poisson's ratio changing from low to high in the target zone affects the seismic amplitudes at different frequencies. A low value for Poisson's ratio represents the *pre-steam* environment and a high value for the *post-steam* environment. Synthetic results at large angles of incidence are also used to justify that it is necessary to go beyond the current recording offsets for detecting the subtle changes induced by changes in Poisson's ratio. The synthetic seismograms that follow are displayed with true relative amplitudes unless otherwise stated. 513 frequency points were

calculated within the range 0-150 Hz. A Gaussian time-variation with a dominant frequency of 35 Hz was used and the cosine taper used was (0/0/125/140 Hz). The k -integral was calculated with three subintervals.

Figure 5.8a shows a simplified "Cold Lake" model with 7 layers which has a low velocity zone with Poisson's ratio $\sigma = 0.2$. The source was buried at 10 m deep. Figure 5.9A shows the behavior of the real parts of the reflectivity functions at four different frequencies: two lower and two higher ones. The arrows point to the location of the real parts of the branch points for the square roots K_α and K_β , i.e. to the P - and S -wave slownesses in the half-space and source layer respectively, multiplied by the corresponding angular frequency. The integrands are smoother especially at high frequencies than those from the one-layered half-space (Figure 4.3) due to lower Q . However, the basic behavior is the same: Rayleigh energy is dominant at low frequencies and diminishes at high frequencies. Figure 5.10 displays a plot of the real parts of the branch points versus calculated frequencies for the simplified models. Lines 1 and 2 are the loci of P - and S -wave slownesses in the half-space multiplied by the corresponding angular frequency {denoted as $(b_\alpha)_{\text{half}}$ and $(b_\beta)_{\text{half}}$ } whereas lines 3 and 4 are correspondingly due to P - and S -wave slownesses within the source layer {denoted as $(b_\alpha)_{\text{source}}$ and $(b_\beta)_{\text{source}}$ }. Two effective values of k_{max} were used with different cosine tapering.

Figure 5.11 shows two components of synthetic sections of true relative amplitudes calculated with k_{max} being $(b_\beta)_{\text{source}} + 145$ and cosine taper {0/0/ $(b_\beta)_{\text{source}} + 100$ / $(b_\beta)_{\text{source}} + 145$ }. The shaded area in Figure 5.10 denotes the coverage of the k -values involved with line 5 as the boundary. The k_{max} thus chosen covers most of the Rayleigh energy at low frequencies, resulting that the Rayleigh arrival is the most prominent event in both components. By choosing $k_{\text{max}} = (b_\beta)_{\text{source}}$ with {0/0/ $(b_\alpha)_{\text{source}}$ / $(b_\beta)_{\text{source}}$ } as tapering, the Rayleigh wave is excluded from Figure 5.12.

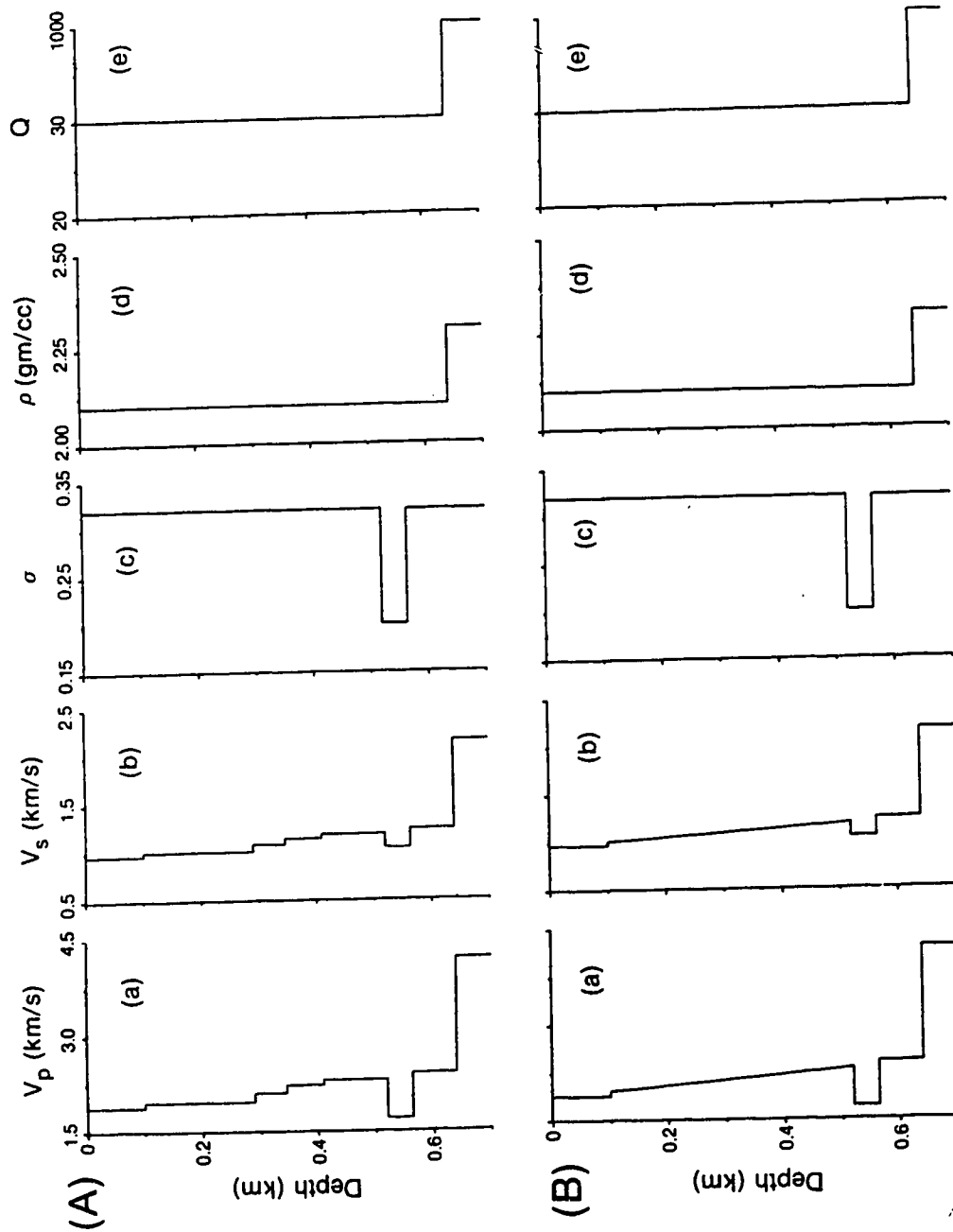


Figure 5.8: Two simplified "Cold Lake" models with a low velocity zone: (A) 7 discrete homogeneous layers and (B) 4 layers with a velocity gradient.

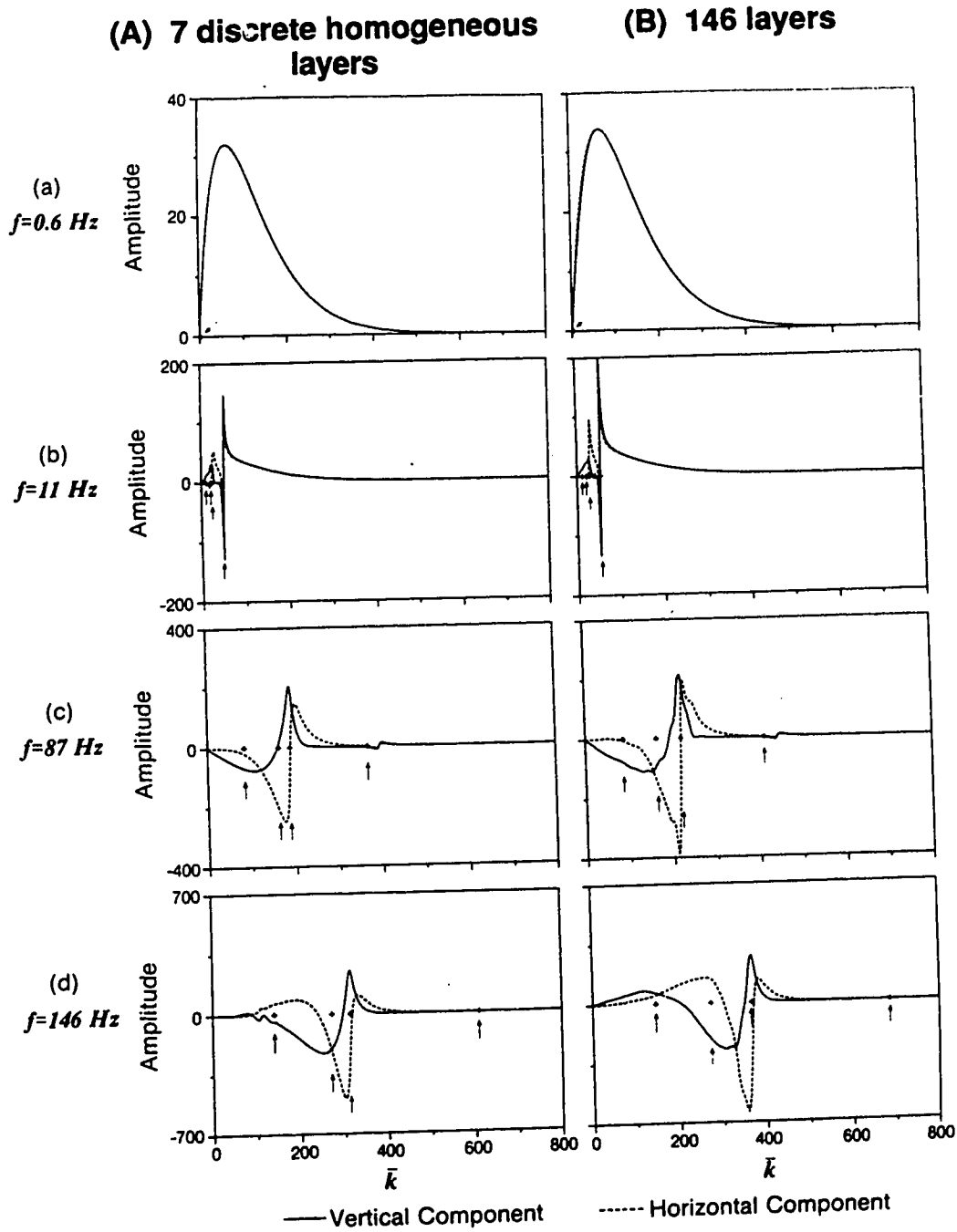


Figure 5.9: Plots of the real parts of the reflectivity functions at four different frequencies for (A) 7 discrete homogeneous layers and (B) 146 layers. The arrows point to the location of the real parts of the branch points for the square roots K_α and K_β . The first two are from the P - and S -wave velocities of the half-space and the last two are from the P - and S -wave velocities of the source layer.

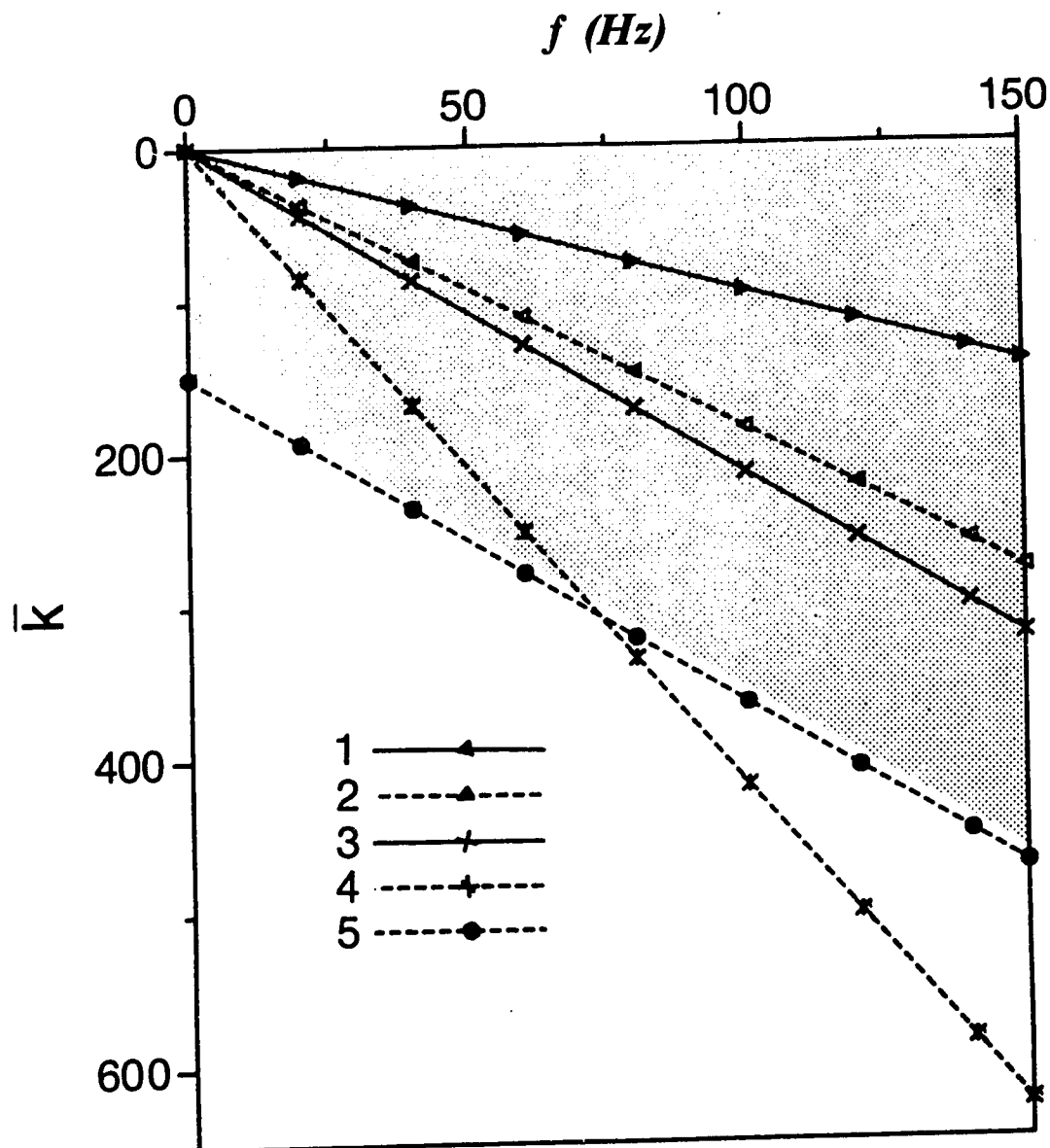


Figure 5.10: Plot of real parts of the branch points versus frequency. These are a function of the P -wave velocity in the half-space (line 1), S -wave velocity in the half-space (line 2), P -wave velocity within the source layer (line 3) and S -wave velocity within the source layer (line 4). Line 5 delineates the boundary (or upper limit) of the k -integral for results shown in Figure 5.11 and the shaded area denotes the coverage.

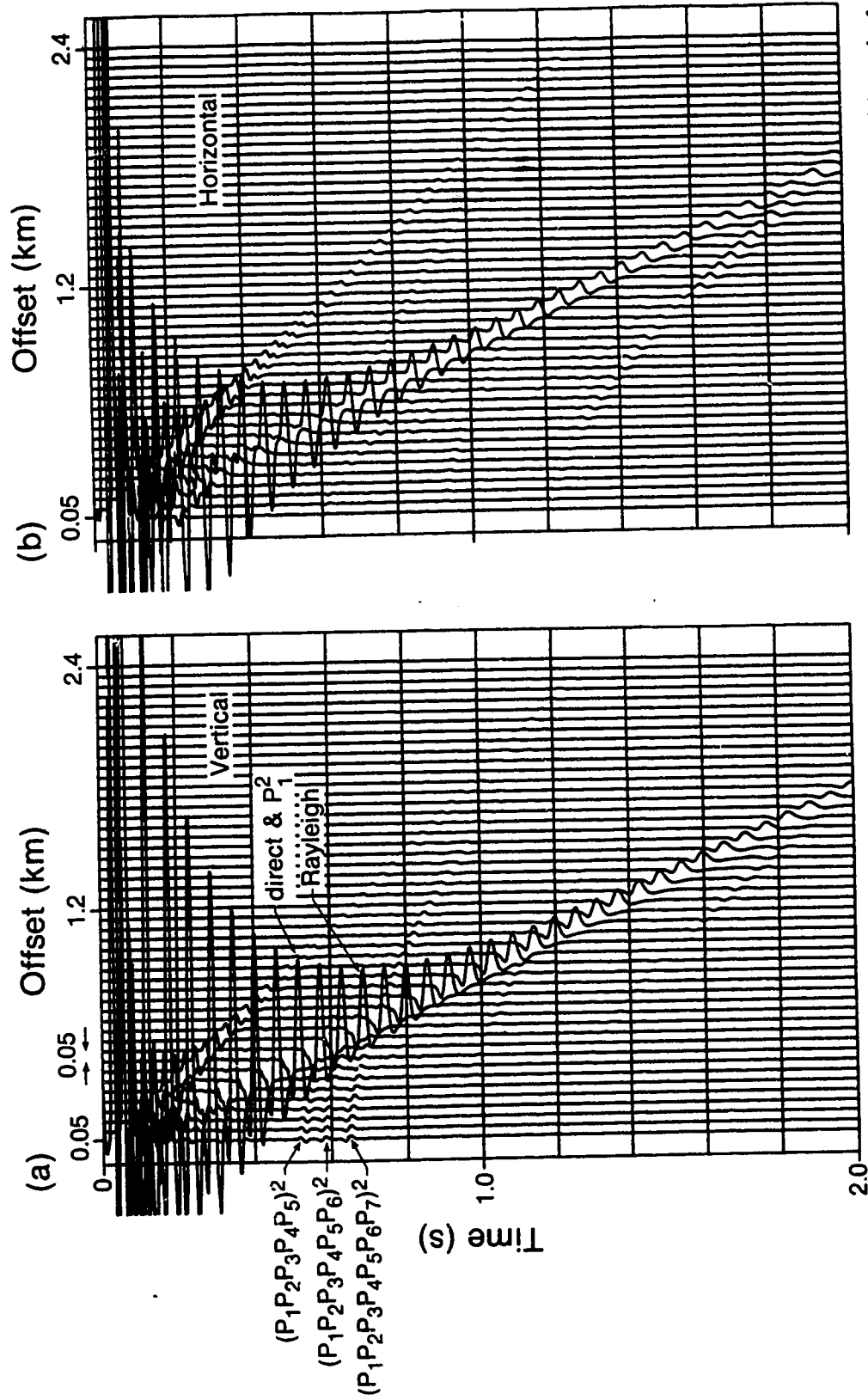


Figure 5.11: Synthetic velocity sections for the 7-layered "Cold Lake" model with Rayleigh wave included. (a) vertical component and (b) horizontal component. The arrows mark the approximated arrivals of the indicated phases. The superscript denotes the multiplicity of the ray traversing the layer indicated by the subscript.

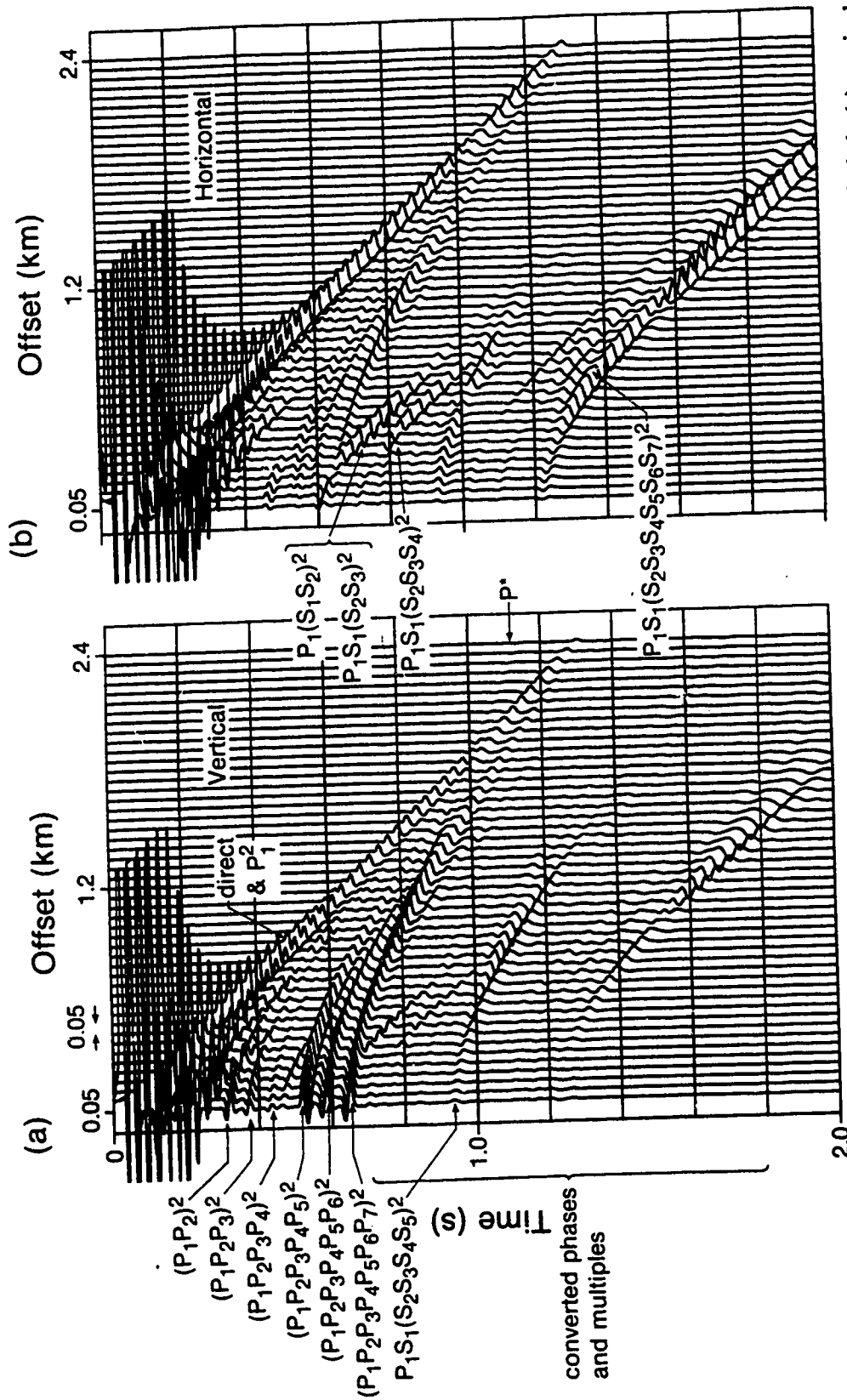


Figure 5.12: Synthetic velocity sections for the 7-layered "Cold Lake" model with Rayleigh wave excluded. (a) vertical component and (b) horizontal component. The arrows mark the approximated arrivals of the indicated phases. The superscript denotes the multiplicity of the ray traversing the layer indicated by the subscript.

The primary reflections have bigger amplitudes in the vertical components than in the horizontal components due to the source type and vice versa for the converted reflections. These properties are preserved in other synthetic results to be discussed. Due to the high velocity contrasts, the last three primary reflections are strong events as indicated. The head wave P^* from the half-space is weak while converted reflections, e.g. $P_1(S_1S_2)^2$ at the free surface are noticeable especially in the horizontal section. Most of the converted reflections arise from the intermediate layers, have large amplitudes (Figure 5.12B) and cut across the primary arrivals. The strong events after 1.2 sec are due to the constructive interference of the converted modes and multiples.

Synthetic results from a 4-layered model with a velocity gradient shown in Figure 5.8B are given in Figure 5.13. The same processing parameters used for Figure 5.12 were employed. Since the gradient zone replaces the intermediate 4 layers, the primary reflections and the converted reflections within these layers disappeared accordingly. P_1S_1 and $P_1S_1^2$ show up as early events in both components. Diving rays from the gradient zone are very weak and interfere with P_1^2 and the direct arrival. The head wave, P^* , is also a weak arrival.

From discretization of the sonic and density logs from Cold Lake area, a multilayered structure was obtained as shown in Figure 5.14A with 146 layers. Some thin layers with high velocities are real and consistent with the high density picks. The target zone is 44 m thick and 440 m deep. Figure 5.14B shows the expanded portion of the profiles in the target region and represents the undisturbed environment before steam injection (*undisturbed state*). The intrusion of steam in the target zone changes the petrophysical properties of the medium. Figure 4.15C is one of the suggested profiles for the on-going steam injection or post-steam injection environment (*steam state*) which has a P -wave velocity gradient from 2100 m/s at 440 m to 1800 m/s at 470 m and then back to 2100 m/s at 484 m. The zone has an average density of 2.15 gm/cc and a low Poisson's

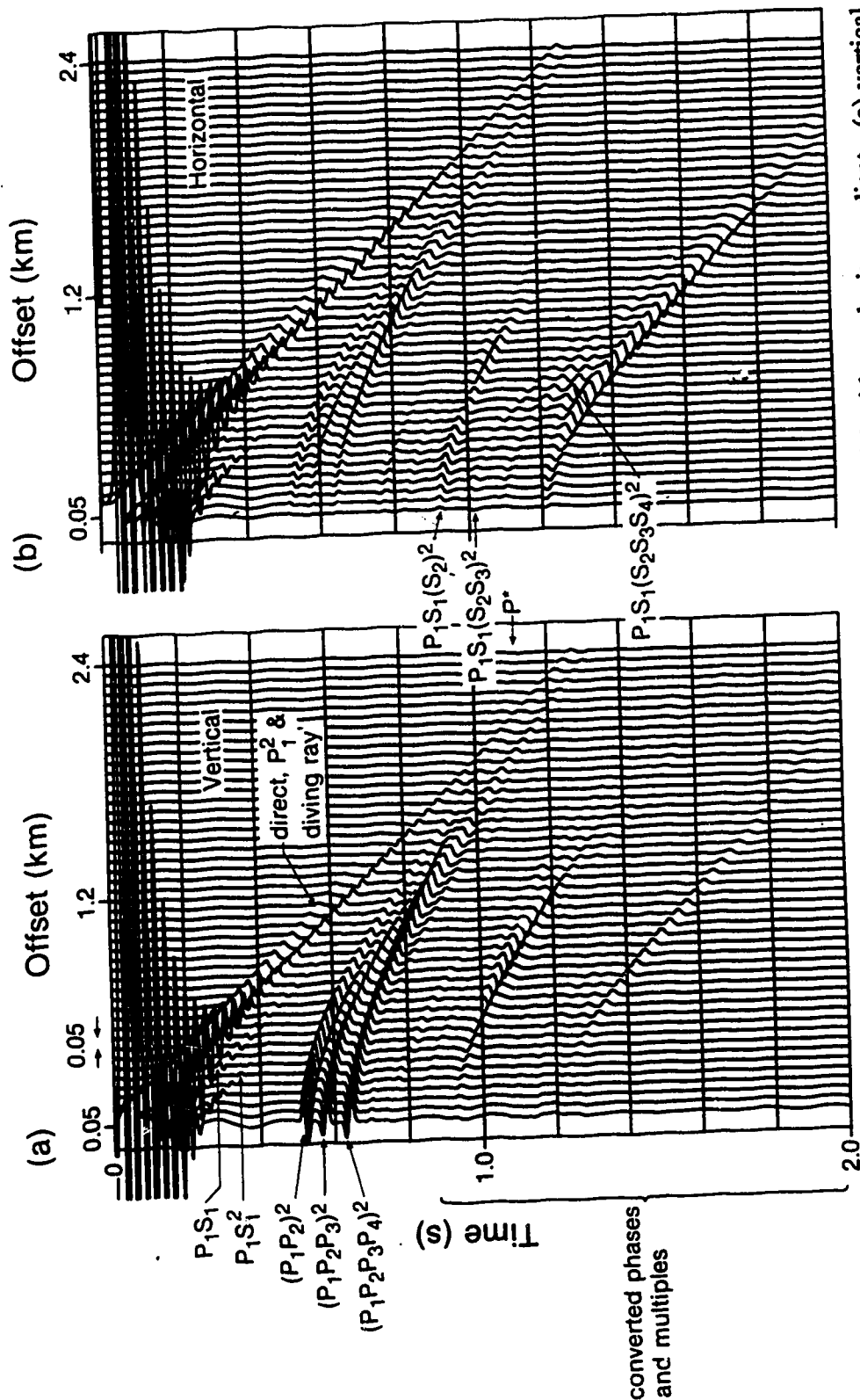


Figure 5.13: Synthetic velocity sections for the 4-layered "Cold Lake" model with a velocity gradient. (a) vertical component and (b) horizontal component. The arrows mark the approximated arrivals of the indicated phases. The superscript denotes the multiplicity of the ray traversing the layer indicated by the subscript.

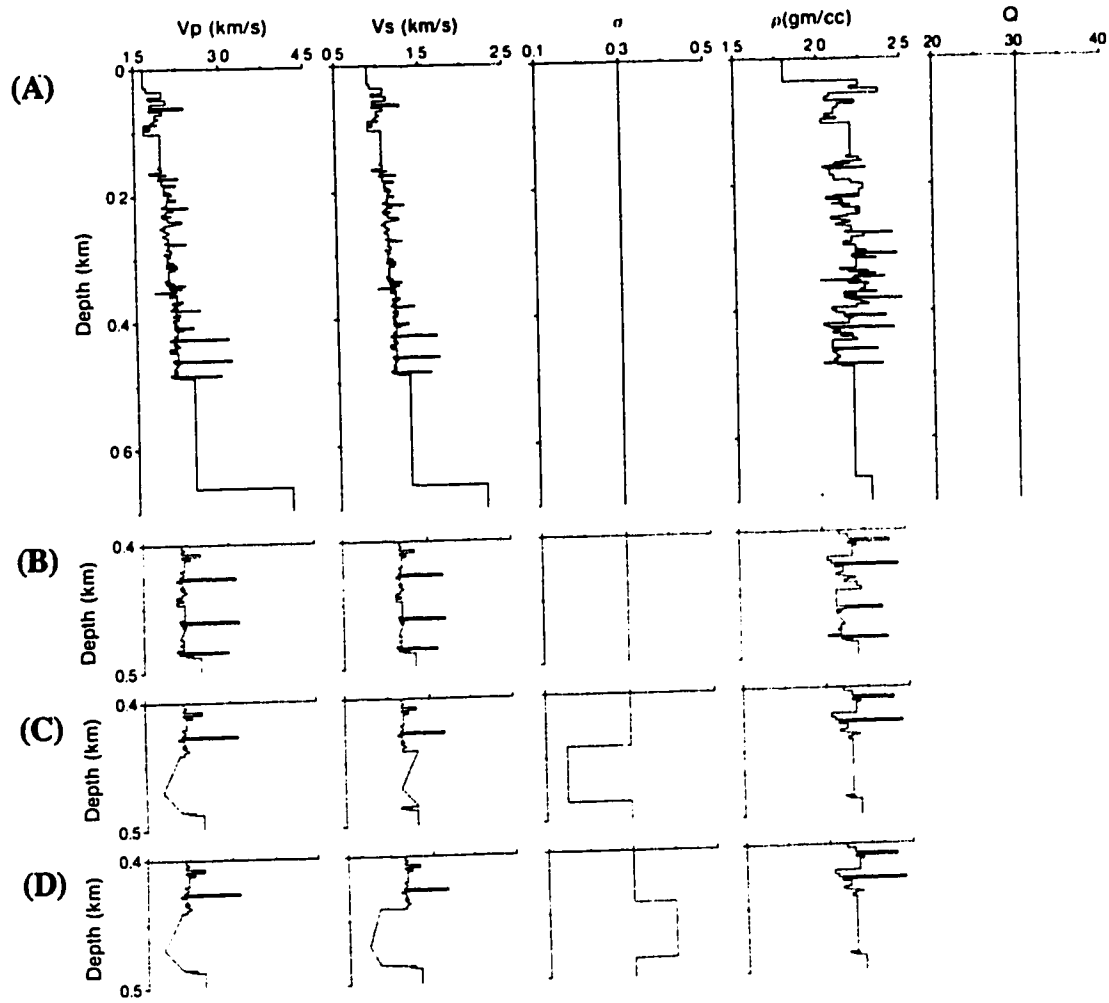


Figure 5.14: Multilayered "Cold Lake" models: (A) an *undisturbed* model; (B) expanded portion of an *undisturbed* model; (C) expanded portion of a *steam* model with a zone of low Poisson's ratio; (D) expanded portion of a *condensation* model with a zone of high Poisson's ratio. σ is Poisson's ratio, ρ is density and the same Q applies for Q_α and Q_β .

ratio of 0.15 simulating the *steam* environment. In case steam condensation (*condensation state*) is severe, a high Poisson's ratio of 0.4 (Figure 5.14D) was employed to account for the presence of a non-viscous fluid mixing with the mobile viscous bitumen. Numerical simulation in these cases assumes that the reservoir is widespread laterally which is indeed the case, and the reflected rays do sample the interior of the zone without encountering the edges.

Plots of the reflectivity functions for the *undisturbed state* at four different frequencies are shown in Figure 5.9B. Except for some difference in general characters and amplitude, the behavior of the reflectivity functions of the 7-layered and 146-layered cases is very similar at all four frequencies. In order to compare theoretical results for different *states* of the reservoir, it is convenient to define notations for major reflections. For all cases P_1 stands for the P -reflection from the thin layer at 426 m with a large velocity spike and P_{half} denotes the P -reflection from the half-space. P_{B1} and P_{B2} are the P -reflections from the other two thin layers of high velocity at 460 m and 484 m depth in model B (Figure 5.14B). P_{C1} and P_{D1} have the same arrival time in models C and D (Figure 5.14C and D) and represent the P -reflection from the velocity discontinuity at around 484 m in depth.

In order to see some interference effects from finely-layered structure at close offset and earlier times, incident arrivals are attenuated by choosing a k -taper: $\{0/0/(b_\alpha)_{\text{source}} * 09/(b_\alpha)_{\text{source}}\}$ with k_{max} being $(b_\alpha)_{\text{source}}$. Figures 5.15 and 5.16 show the synthetic sections of both vertical and horizontal components. The amplitudes have been exponentially scaled by $\exp(7t)/13$. An attempt at identifying reflections from each interface is difficult even at close offsets since the reflections in finely-layered structure tend to interfere with one another giving rise to a broader integrated pulse. Reflection from the half-space, P_{half} can be seen in all cases (Figure 5.15). P_1 is present at close offsets and seems to lose its identity when one goes beyond 180 m. The arrival times of P_{B1} and P_{B2}

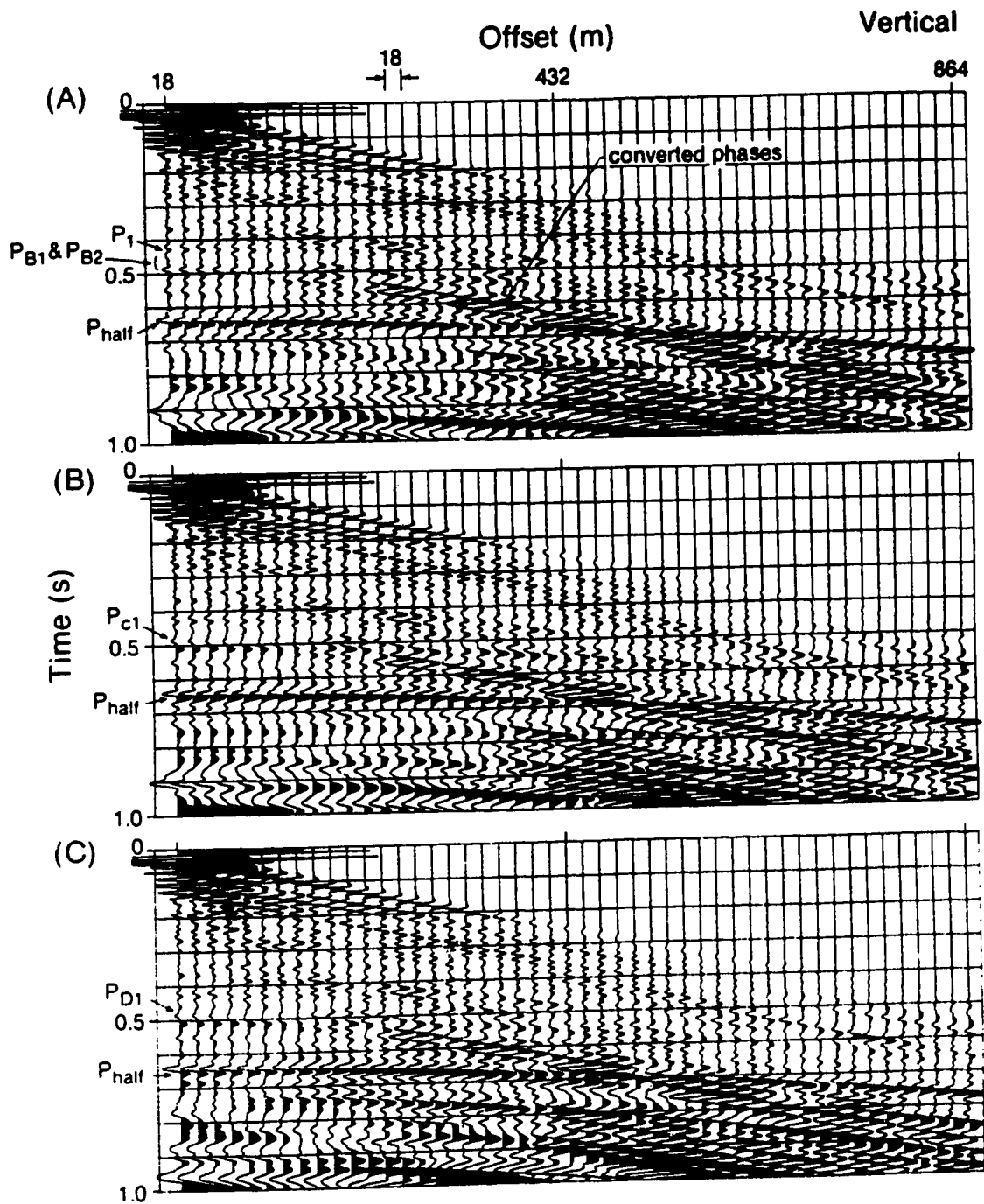


Figure 5.15: Synthetic vertical velocity sections for the multilayered "Cold Lake" models: (A) *undisturbed state*; (B) *steam state* and (C) *condensation state*.

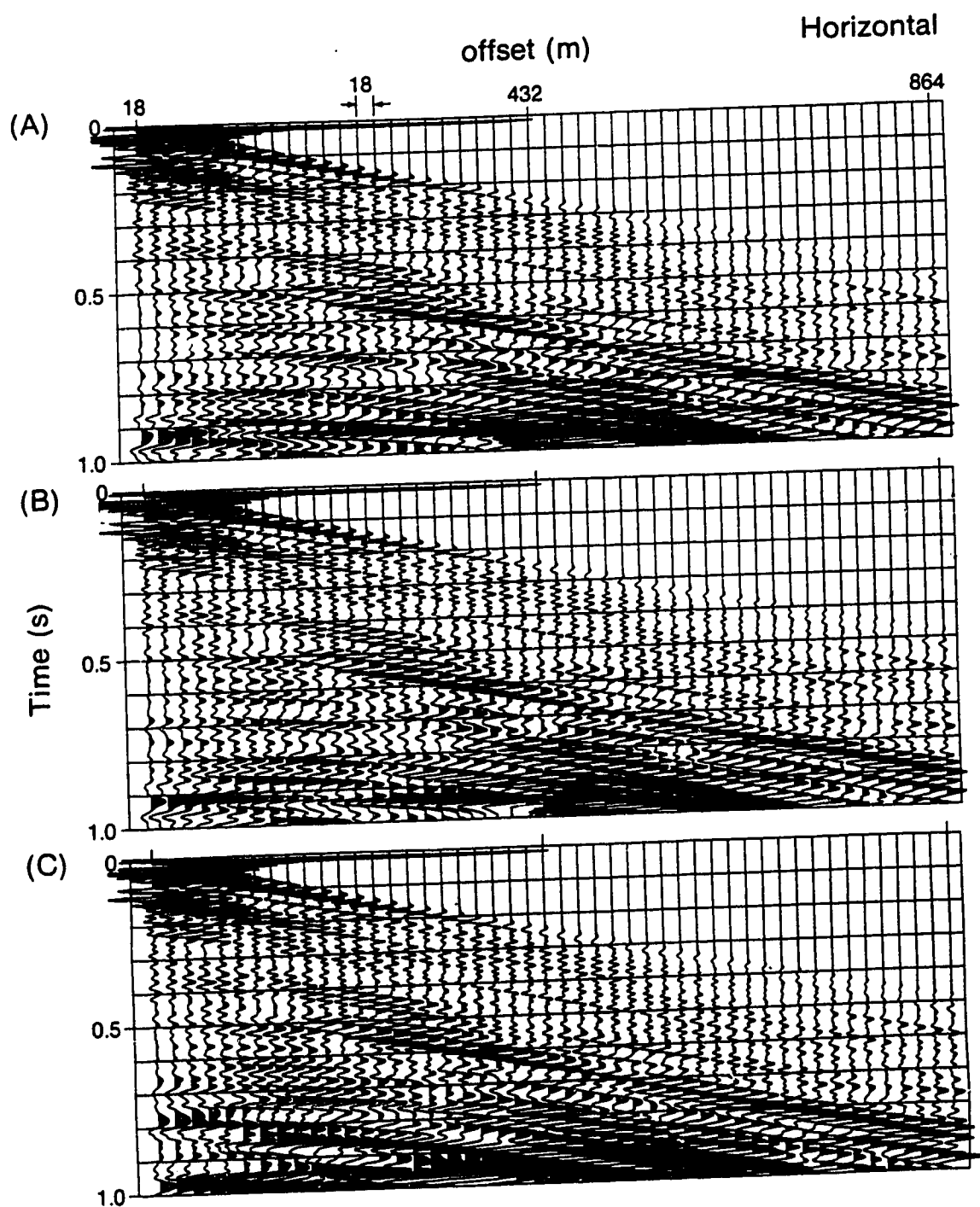


Figure 5.16: Synthetic horizontal velocity sections for the multilayered "Cold Lake" models: (A) *undisturbed state*, (B) *steam state* and (C) *condensation state*.

are hard to define. Converted reflections are strong arrivals cutting the arrival P_{half} in the middle of the sections (Figure 5.15). Horizontal components (Figure 5.16) are prominent with many strong converted arrivals.

The spectral character of the components are given in Figures 5.17 and 5.18 for the closest ($r=18$ m), the middle ($r=432$ m) and the farthest ($r=864$ m) traces. The spectra indicate that the spectral amplitude and frequency content decrease with offset. This is as expected since high frequencies are more absorbable by the Q of the Earth and seismic energy is spreading out along bigger wavefronts and anelastically attenuated in its passage through the Earth. At close offset ($r=18$ m), the vertical spectra are bimodal and the horizontal spectra have only one mode. The horizontal spectra have larger amplitudes and energy content, thus justifying the predominance of the horizontal components over the vertical ones. The spectra at the same offset for all three *states* look similar. Spectral dissimilarity can be seen by taking the difference. For example, Figure 5.18D shows the difference between the spectra of the *undisturbed* and *condensation states*. The difference indicates the effect of Poisson's ratio on the spectral characters. Differences are mainly confined within the low frequency band and imposes no difficulty for detection by modern broadband recording instruments. However, the differences which varies within approximately ± 0.05 , though significant, may be too subtle to be detected since it has to be recorded in a background of noise. It should be mentioned that the effect of Q has been neglected in this study since in *steam-condensation state*, Q tends to be smaller than 10 and compound effects due to change in Q and Poisson's ratio might greatly enhance the difference (Macrides and Kanasewich, 1987). Also, greater spectral difference might be expected if a window containing mostly arrivals from the target zone is analysed. Perhaps the significant change due to the difference in Poisson's ratio can be found by analyzing the change in seismic amplitudes with angle of incidence (AVO).

Since the only difference in structures lies in the target zone, seismic response

Vertical

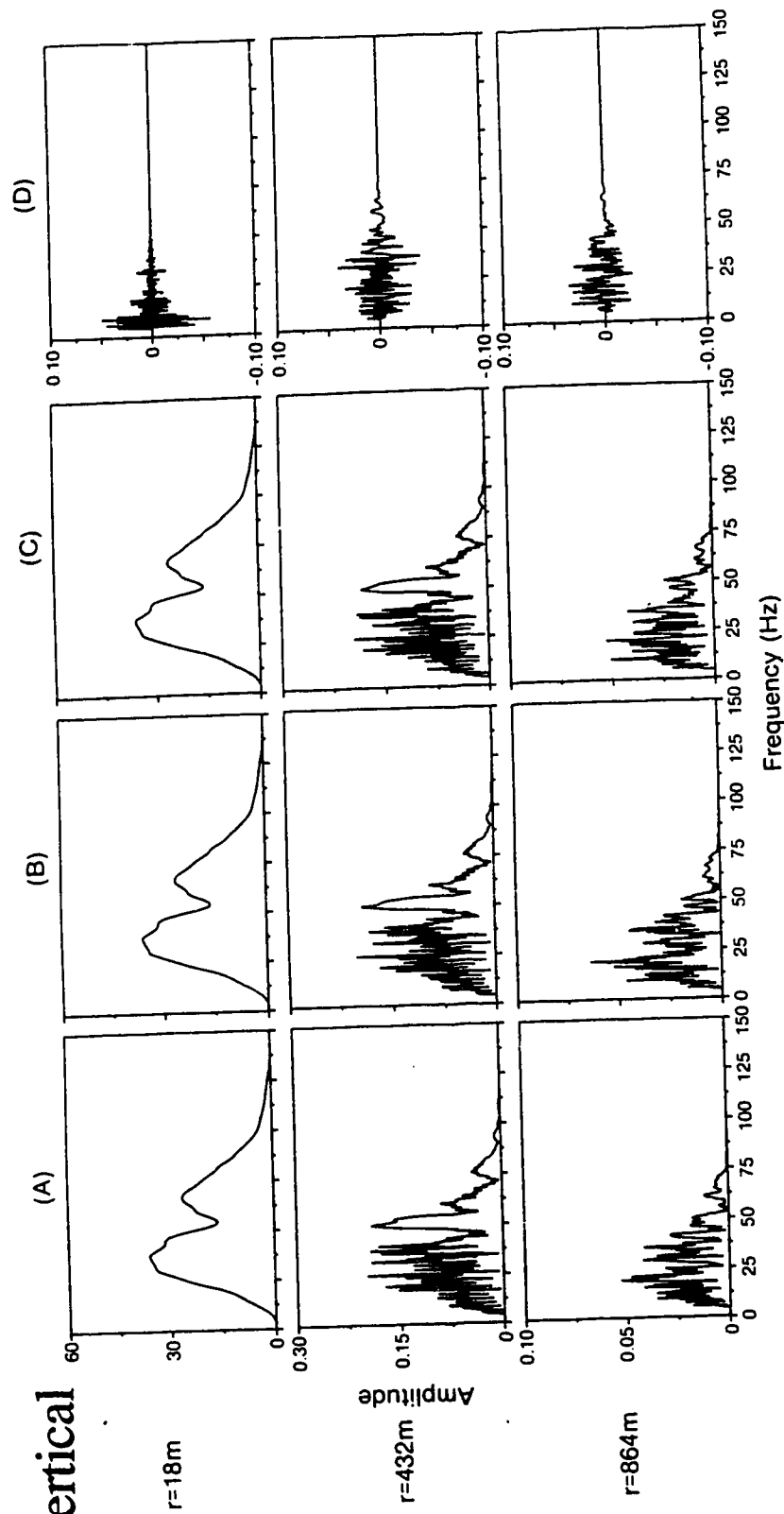


Figure 5.17: Amplitude spectrum of the vertical components for the three traces: the closest, the middle and the farthest in Figure 5.15. (A) Undisturbed state, (B) steam state, (C) condensation state and (D) difference between steam and condensation states.

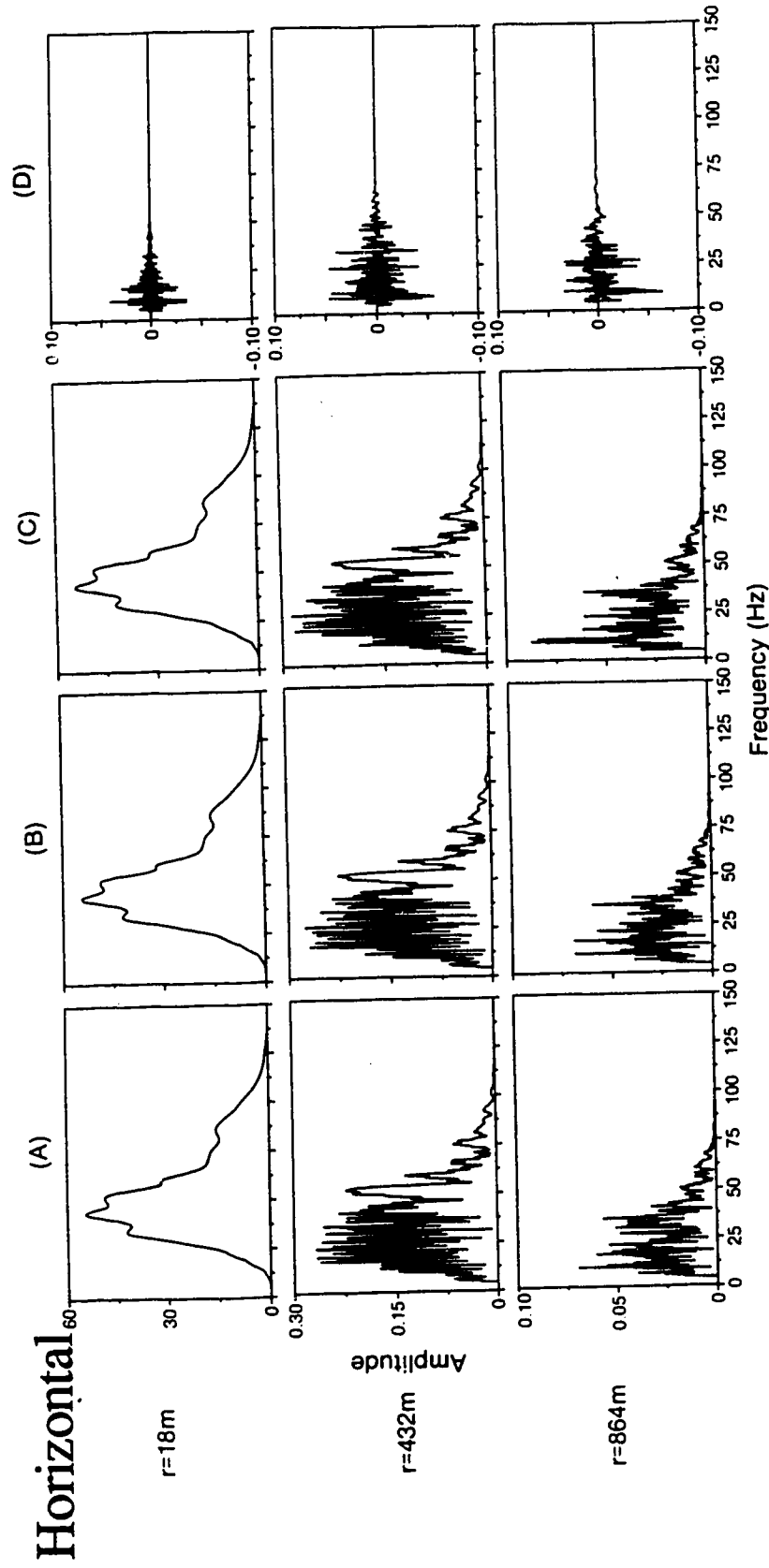


Figure 5.18: Amplitude spectrum of the horizontal components for the three traces: the closest, the middle and the farthest in Figure 5.16. (A) Undisturbed state, (B) steam state, (C) condensation state and (D) difference between steam and condensation states.

above the zone should be expected to be the same. This is indeed the case as shown in the difference plots (Figures 5.19 and 5.20). The plots show the differences of actual amplitudes of the response between *states* with no exponential gain. The shaded portion is positive difference and the unshaded is negative. The differences as shown in Figures 5.19A and B display the effect of structure difference on seismic signatures. The difference in elastic properties in the steam-invaded zone induce shifts in arrival time and changes in seismic characters of later arrivals. There are two strong *events of difference* between the *undisturbed* and *steam states* in Figure 5.19A indicating that there are significant variation in reflection amplitudes arising from the steam-zone (*steam-zone event*) as well as from the half-spaces (*half-space event*). The former is due to change in elastic properties and the latter is mainly due to time shift. As well, the plot shows that the *undisturbed* amplitudes are stronger than the *steam* amplitudes and this property persists across the section. The *steam-zone event* tends to have two strong peaks which are stronger at close offset than at far offset. The reverse is true for the horizontal difference as shown in Figure 5.20A where at close offset, the amplitudes from both states are comparable and the *undisturbed* amplitudes are bigger only at far offsets. Differences in later arrivals such as multiples are more evident in the horizontal components.

Figures 5.19B and 5.20B show the difference in seismic responses between the *undisturbed* and *condensation states*. Increase in Poisson's ratio reduces the shear wave velocity. Difference in later arrivals such as converted modes are stronger in this case especially in the horizontal components (Figure 5.20B). Amplitudes of horizontal response from the target zone in both *states* are quite similar giving rise to an "almost" null difference (Figure 5.20B) as compared with the difference between *undisturbed* and *steam states* (Figure 5.20A). As shown in Figure 5.19B, the strength of the two peaks of the *steam-zone events* at close offsets is replaced by a strong trough from 430 m onwards indicating that the *condensation* amplitudes are stronger at far offsets. The *half-space*

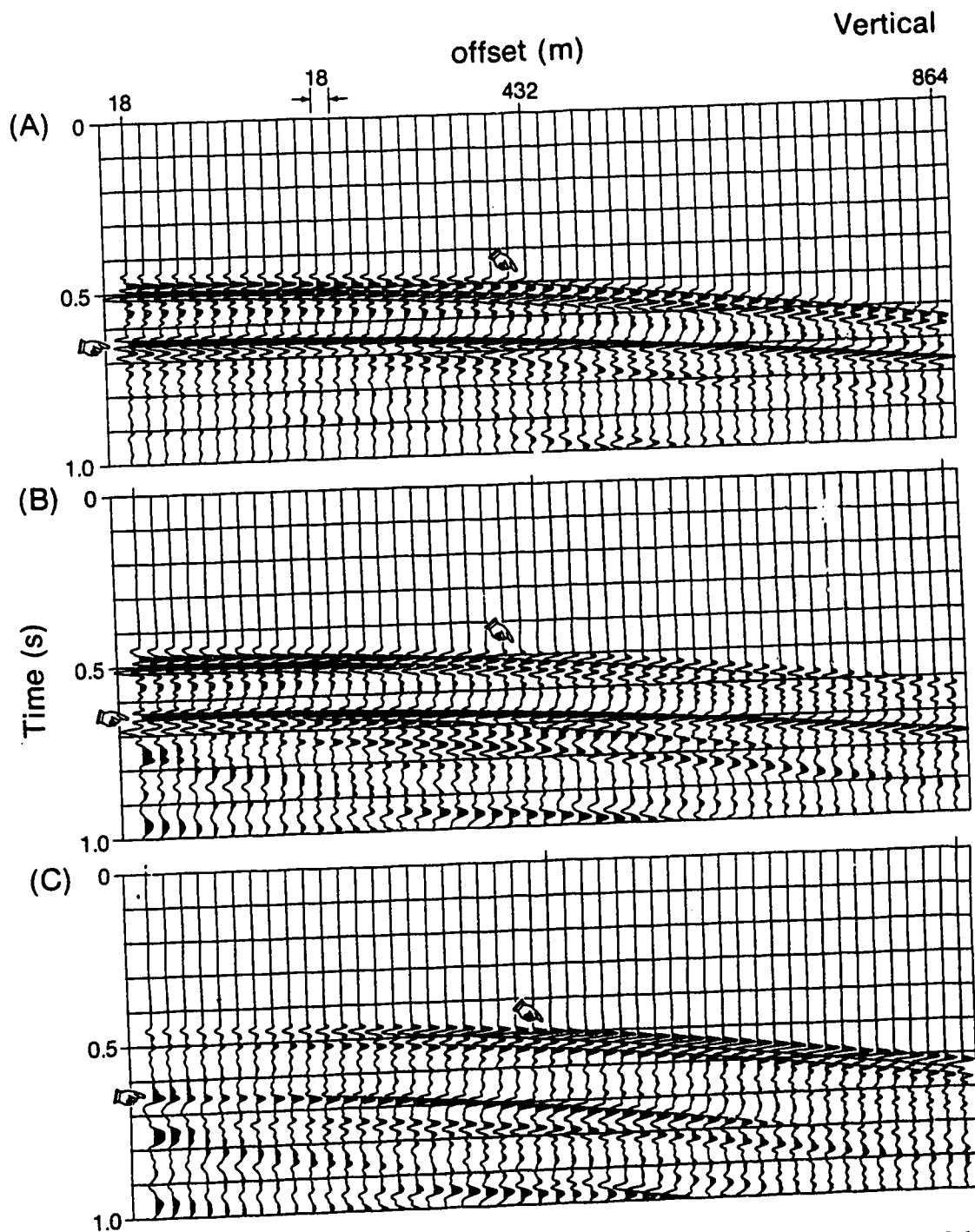


Figure 5.19: Vertical sections of differences for the multilayered "Cold Lake" models. Difference between (A) *undisturbed-steam states*, (B) *undisturbed-condensation states* and (C) *steam-condensation states*. The fingers indicate the *steam-zone event* and the *half-space event*.

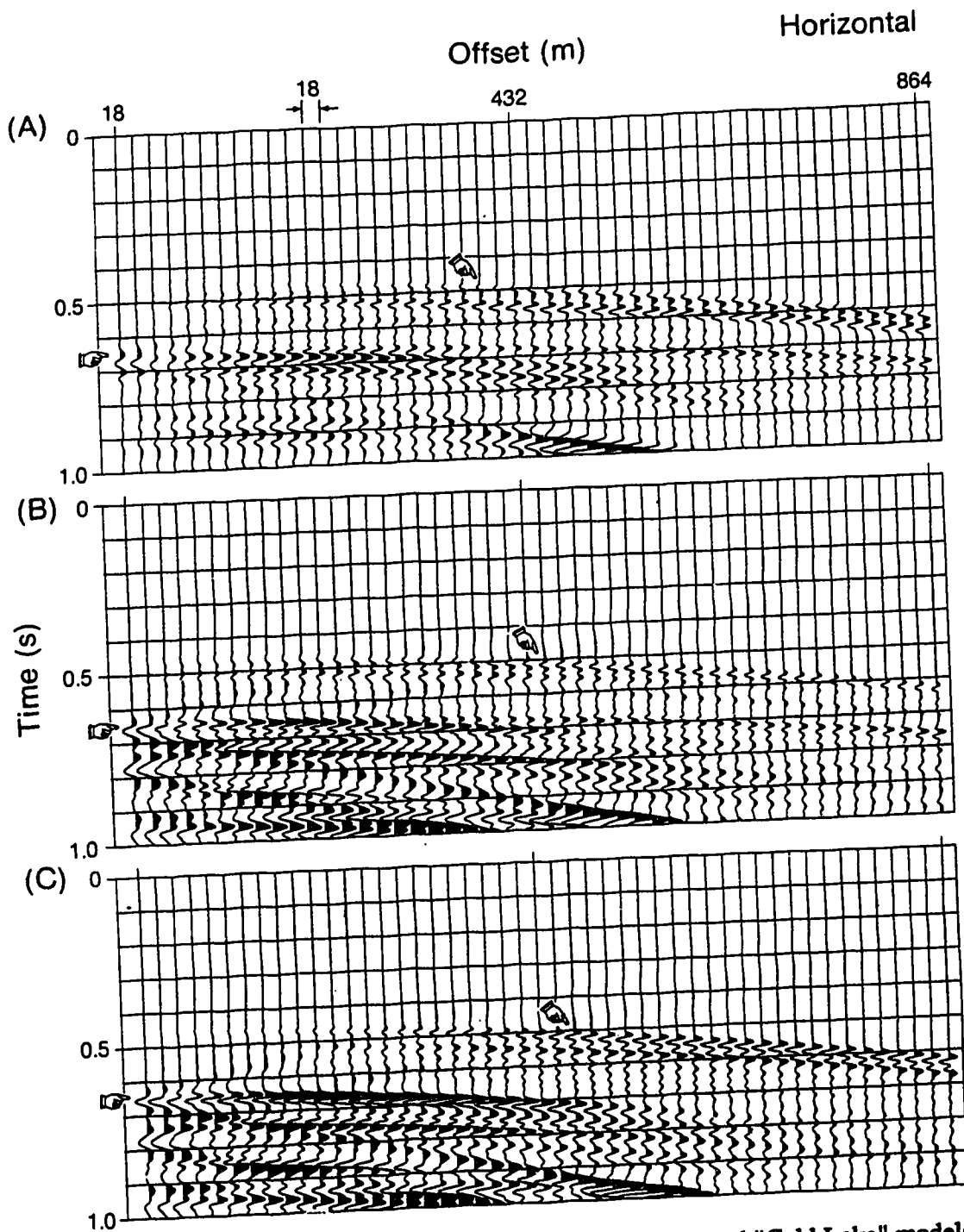


Figure 5.20: Horizontal sections of differences for the multilayered "Cold Lake" models. Difference between (A) *undisturbed-steam states*, (B) *undisturbed-condensation states* and (C) *steam-condensation states*. The fingers indicate the *steam-zone event* and the *half-space event*.

event persists across the section as in the *undisturbed-steam states*. The effect of Poisson's ratio on seismic response has been intensively investigated under the category of *amplitude versus offset* (AVO) using plane wave theory by Koefoed (1955), Ostrander (1984), Shuey (1985) and Tsingas (1989), to name a few. The main problem is to infer the underlying elastic parameters from seismic amplitudes. In cases where the fine-scale structure of the medium is considered, care has to be taken to analyse the reflection amplitudes for formation identification and elastic parameters inversion since the effect of such fine structure give rises to anomalous reflection amplitudes due to interference (Stephens and Sheng, 1985). Figures 5.19C and 5.20C display the effect of Poisson's ratio on seismic response. Since *P*-wave velocity does not change, the difference seen in these plots originates from the converted shear modes due to change in Poisson's ratio from 0.15 to 0.4. Significant differences can be seen from moderate to far offsets. At far offset strong positive difference of the *steam-zone event* is shown in vertical components (Figure 5.19C) and strong negative difference in horizontal components (Figure 5.20C). The *half-space event* is significant up to 700 m. Differences in later arrivals are more prominent in horizontal components.

In summary, there are significant changes in seismic amplitudes, frequency content and arrival time between *states*. However, most of these subtle differences can only be detected at the far offsets, i.e. beyond 432 m.

5.4 Conclusion

By making a series of comparison between the three *states: undisturbed-steam, undisturbed-condensation and steam-condensation* using the multilayered "Cold Lake" model, significant changes in seismic response have been found. These subtle changes can provide valuable information about the *state* of the target zone, however they can only be

detected at far offsets.

Although the numerical results obtained using an ω - k integral representation are not identical with the results based on the Cagniard-Pekeris-de Hoop method for the elastic theoretical model, the high degree of similarity gives us confidence that the ω - k method may lead to reliable results for complex structures, especially for structures that contain a certain degree of anelasticity.

Synthetic sections for four simple structures: two deep and two shallow indicate that within the calculated frequency-wavenumber window, the method gives rises to all the arrivals predicted by simple ray tracing. Converted reflections are prominent in all cases and in the horizontal component sections. Multiple-components recording: vertical and horizontal are beneficial for shear wave analysis since converted events are *masked* in the vertical components.

CHAPTER 6

CONCLUDING REMARKS

An analytic expression for the transmitted *SH*-wave from an impulsive line source through a boundary separating two elastic, homogeneous and solid half-spaces has been derived by means of the Cagniard-de-Hoop method. Besides the transmitted arrival, an evanescent wave shows up in the synthetic results as part of the solution of the wave equation when the incident angle is greater than the critical angle.

A very thorough investigation of the properties of the evanescent wave was made, particularly for the case when attenuation is introduced in the medium. This has clarified the behavior of particle motion which, in the literature, had been extrapolated to point and line sources with the use of plane wave theory. When either the source or the receiver is close to the boundary between the half-spaces, the amplitudes of the transmitted and evanescent waves are comparable. The evanescent wave does not have a definite phase velocity but depends on the incident angle and has its maximum attenuation perpendicular away from the boundary. The amplitude decay of waves with distance far from the interface agrees well with the rate predicted by asymptotic theory. Utilizing the small skin-depth penetration of the evanescent wave and in favorable velocity contrasts and source-receiver configurations, valuable elastic properties of the shallow crusts may be retrieved.

The expression for the transmitted *SH*-wave for the same two-half-spaces problem has been recast in a form of an improper ω - k double integral. In this way, effects of anelasticity can be incorporated easily by making velocities of the medium complex. For the simple models of two anelastic or one elastic and one anelastic half-space in welded contact considered, all the arrivals predicted by the elasticity theory are present. Elastic results compare well with those obtained by the Cagniard-de Hoop method. Synthetic

results have demonstrated that attenuation does not drastically change the physical picture seen in the elastic case but modifies it in a continuous manner. The broadening of the pulse and the reduction of amplitudes have been anticipated due to dispersion and attenuation. The evanescent wave is present in anelastic media after a certain *threshold* distance is satisfied. The argument in the inhomogeneous plane wave theory that *the critical angle is discrete or non-existent in anelastic medium* (Borcherdt, 1973 and 1977; Krebs, 1980) does not seem to explain the phenomena satisfactorily. The reason for the discrepancy between our results and those from plane wave theory lies in the importance of curvature of the wavefronts considered in this case.

The basic mathematical formalism of wave propagation in an anelastic layered half-space due to a point P -source has been discussed along with its numerical implementation and computation aspects. The displacement components are expressed in closed form as improper ω - k double integrals. The integrands of the k -integral are products of the reflectivity functions and offset-dependent Bessel functions. The reflectivity function depends on the elastic properties of the structures and is a linear combination of factors of the source terms and the 2nd order minors. These terms can be obtained by directly integrating the 4th and 6th order differential systems of 1st order equations. The reflectivity functions are the same for any model and source depth and are calculated only once. The upper limit, k_{\max} of the k -integral, is determined to cover the significant parts of the integrands by examining some plots of the reflectivity functions. Examination of this kind is not necessary if a certain k -window (or velocity-window) is desired. The integration range is then divided into three or four subintervals and within each Romberg scheme of 513 points is used. Within any frequency band, 513 frequency points are computed and the ω -integral is achieved by an inverse FFT. Fine sampling in frequency space is necessary to avoid aliasing events in temporal space unless some smoothing operations are taken such as using complex frequency. Cosine taperings in the ω - k plane

are applied to avoid aliasing events in r - t space.

The ω - k integration method demonstrated here has the advantage of yielding the complete solution within a desired frequency-wavenumber bandpass. Surface and direct waves can be included or excluded by limiting the wavenumber integration. Similar to the reflectivity method, our formulation is computationally expensive. Computational time can be greatly reduced if an adaptive integration scheme with automatically-adjusted sampling interval is employed to avoid oversampling in the smooth part of the integrand. As well, less computation time is required by finding the eigen-solutions in the homogeneous sublayers and limiting the Runge-Kutta integration in the inhomogeneous sublayers. However, unlike the former method, the theory as presented provides a simpler algorithm, bypassing the bookkeeping required to account for the upgoing and downgoing waves.

Numerical studies from some simple crustal and shallow models have demonstrated the numerical approach is well adapted to any model on any scale. The results from such models have also indicated that the occurrence of events agree well with ray tracing. Synthetic seismograms from finely-layered Cold Lake models have shown detectable changes in seismic amplitudes and arrival times in *pre*- and *post-steam* condition. However, spectral characters from synthetic results do not show as strong differences between *states* as the analysis of real data indicated (Macrides, 1987). Far-offset recording is able to provide valuable information about the current *state*: *steam* or *condensation* of the reservoir. Recording of both vertical and horizontal components is desirable to distinguish the underlying factors inducing the changes.

In this dissertation a complete theoretical and numerical exposition of the ω - k method has been presented and the synthetic seismograms using the algorithm as presented have been given for the first time. The method yields the *complete wave solution* for a point P -source in a vertically inhomogeneous and anelastic layer over a half-space. The method has been shown to be practical with the availability of the latest parallel or vector

processors. With the current computer power and storage capacity, computing wave propagation in anisotropic and porous media using the ω - k formalism will be our next phase of investigation.

REFERENCES

- Abramovici, F. (1968a). Diagnostic diagrams for transfer functions for oceanic wave guides, *Bull. Seism. Soc. Am.* 58, 427-456.
- Abramovici, F. (1968b). Mode theory versus theoretical seismograms for a layered solid, *J. Geophys. Res.* 16, 9-20.
- Abramovici, F. (1968c). Computer programs for leaking and locked modes in elastic wave-guides, IGPP, University of California at San Diego.
- Abramovici, F. (1970). Numerical seismograms for a layered elastic elastic solid, *Bull. Seism. Soc. Am.* 60, 1861-1876.
- Abramovici, F. (1974). The forward magnetotelluric problem for an inhomogeneous and anisotropic structure, *Geophysics* 39, 56-68.
- Abramovici, F. (1978). A generalization of the Cagniard method, *J. Comp. Physics* 29, 328-343.
- Abramovici, F. (1990). The double integral solution of seismic problems, 18th Internat. Conf. on Math. Geophys., Abstracts, 65.
- Abramovici, F. and M. Chlamtac (1978). Fields of a vertical magnetic dipole over a vertically inhomogeneous earth, *Geophysics* 43, 954-966.
- Abramovici, F. and J. Gal-Ezer (1978). Numerical seismograms for a vertical point-force in a layered solid, *Bull. Seism. Soc. Am.* 68, 81-101.
- Abramovici, F., L. H. T. Le and E. R. Kanasewich (1989). The evanescent wave in Cagniard's problem for a line source generating *SH* waves, *Bull. Seism. Soc. Am.* 79, 1941-1955.
- Abramovici, F., L. H. T. Le and E. R. Kanasewich (1990). The solution of Cagniard's problem for an *SH*-line source in elastic and anelastic media, *Bull. Seism. Soc. Am.* 80, 1297-1310.

- Abramowitz, M., and Stegun, I. A., 1965, Handbook of mathematical functions, Dover.
- Aki, K. and P. G. Richards (1980). Quantitative Seismology, vol. I, W. H. Freeman and Co., San Francisco, California.
- Alekseev, A. S. and B. G., Mikhailenko (1980). The solution of dynamic problems of elastic wave propagation in inhomogeneous media by a combination of partial separation of variables and finite-difference methods, J. Geophys. 48, 161-172.
- Alford, R. M., K. R. Kelly and D. M. Boore (1974). Accuracy of finite-difference modelling of the acoustic wave equation, Geophysics 39, 834-842.
- Azimi, Sh. A., A. V. Kalinin, V. V. Kalinin and B. L. Pivovarov (1968). Impulse and transient characteristics of media with linear and quadratic absorption laws, Izvestiya, Physics of the Solid Earth 88-93.
- Ben-Menahem, A. (1960). Diffraction of elastic waves from a source in a heterogeneous medium, Bull. Seism. Soc. Am. 50, 15-33.
- Ben-Menahem, A., and M. Vereš (1973). Extension and interpretation of the Cagniard-Pekeris method for dislocation sources, Bull. Seism. Soc. Am. 63, 1611-1636.
- Borcherdt, R. D. (1973). Energy and plane waves in linear viscoelastic media, J. Geophys. Res. 78, 2442-2453.
- Borcherdt, R. D. (1977). Reflection and refraction of type-II S waves in elastic and anelastic media, Bull. Seism. Soc. Am. 67, 43-67.
- Bouchon, M. (1979). Discrete wave number representation of elastic wave fields in three-space dimensions, J. Geophys. Res. 84, 3609-3614.
- Braile, L. W. and R. B. Smith (1975). Guide to the interpretation of crustal refraction profiles, Geophys. J. R. Astr. Soc. 40, 145-176.
- Brekhovskikh, L. M. (1980). Waves in Layered Media, Academic Press, New York.
- Buchen, P. W. (1971a). Reflection, transmission and diffraction of SH-waves in linear viscoelastic solids, Geophys. J. R. Astr. Soc. 25, 97-113.

- Buchen, P. W. (1971b). Plane waves in linear viscoelastic media, *Geophys. J. R. Astr. Soc.* 23, 531-542.
- Cagniard, L. (1939). *Réflexion et Réfraction des Ondes Séismiques Progressives*, Gauthier-Villars, Paris, France.
- Cagniard, L. (1962). *Reflection and Refraction of Progressive Seismic Waves*, translated from French by E. A. Flinn and C. H. Dix, McGraw-Hill, New York.
- Chapman, C. H. (1973). The earth flattening transformation in body wave theory, *Geophys. J. Roy. Astr. Soc.* 35, 55-70.
- Chapman, C. H. (1978). A new method for computing synthetic seismograms, *Geophys. J. Roy. Astr. Soc.* 54, 481-518.
- Chin, R. C. Y., G. W. Hedstrom, and L. Thigpen (1984). Matrix method in synthetic seismograms, *Geophys. J. Roy. Astr. Soc.* 77, 483-502.
- Clowes, R. M. and E. R. Kanasewich (1970). Seismic attenuation and the nature of reflecting horizons within the crust, *J. Geophys. Res.* 75, 6693-6705.
- Coddington, E. A. and N. Levinson (1987). *Theory of ordinary differential equations*, McGraw-Hill.
- Cooper, H. F. Jr. (1967). Reflection and transmission of oblique plane waves at a plane interface between viscoelastic media, *J. Acoust. Soc. Am.* 42, 1064-1069.
- Copson, E. T. (1960). *An Introduction to the Theory of Functions of a Complex Variable*, Oxford University Press, Oxford.
- Davis, P. J. and P. Rabinowitz (1984). *Methods of numerical integration*, Academic Press.
- de Hoop, A. T. (1958). Representation theorems for the displacements in an elastic solid and their application to elastodynamic diffraction theory, Ph.D. Thesis, Technische Hogeschool, Delft, Holland.
- de Hoop, A. T. (1960). A modification of Cagniard's method for solving seismic pulse problems, *Appl. Sci. Res.* B8, 349-356.
- Dunkin, J. W. (1965). Computation of modal solutions in layered, elastic media at high

- frequencies, *Bull. Seism. Soc. Am.* 55, 335-358.
- Drijkoningen, G. G. and C. H. Chapman (1988). Tunneling rays using the Cagniard-De Hoop method, *Bull. Seism. Soc. Am.* 78, 898-907.
- Eringen, A. C. (1965). *Mechanics of continua*, Wiley.
- Ewing, W. M., W. S. Jardetsky and F. Press (1957). *Elastic waves in layered media*, McGraw-Hill.
- Foster, D. J. and J. I. Huang (1990). Global asymptotic solutions of the wave equation, 18th Internat. Conf, Math. Geophys., 63.
- Franssens, G. R. (1983). Calculation of the elasto-dynamic Green's function in layered media by means of a modified propagator matrix method, *Geophys. J. Roy. Astr. Soc.* 75, 669-691.
- Frazer, L. N. (1988). Quadrature of wavenumber integrals, in Doornbos, D. J., Ed., *Seismological algorithms*, Academic Press Inc., 279-290.
- Frazer, L. N. and J. F. Gettrust (1984). On a generalization of Filon's method and the computation of the oscillatory integrals of seismology, *Geophys. J. Roy. Astr. Soc.* 76, 461-481.
- Fuchs, K. (1968). The reflection of spherical waves from transition zones with arbitrary depth-dependent elastic moduli and density, *J. Phys. Earth* 16, 27-41.
- Fuchs, K. and G. Müller (1971). Computation of synthetic seismograms with the reflectivity method and comparison with observations, *Geophys. J. R. Astr. Soc.* 23, 417-433.
- Fung, Y. C. (1977). *A first course in continuum mechanics*, Prentice-Hall.
- Gilbert, F. and S. J. Laster (1962). Experimental investigation of PL modes in a single layer, *Bull. Seism. Soc. Am.* 52, 59-66.
- Gilbert, F., and G. E. Backus (1966). Propagator matrices in elastic wave and vibration problems, *Geophysics* 31, 326-332.

- Gilbert, F., and D. V. Helmberger (1972). Generalized ray theory for a layered sphere, *Geophys. J. Roy. Astr. Soc.* 27, 57-80.
- Harrison, D. B., R. P. Glaister and H. W. Nelson (1981). Reservoir description of the Clearwater oil sand, Cold Lake, Alberta, Canada, in *The future of heavy crude and tar sands*, McGraw-Hill Inc., 264-279.
- Haskell, N. A. (1953). The dispersion of surface waves on multilayered media, *Bull. Seism. Soc. Am.* 43, 17-34.
- Helmberger, D. V. (1968). The crust-mantle transition in the Bering-Sea, *Bull. Seism. Soc. Am.* 58, 179-214.
- Helmberger, D. V. (1973). On the structure of the low velocity zone, *Geophys. J. R. Astr. Soc.* 34, 251-263.
- Helmberger, D. V. and R. Wiggins (1971). Upper mantle structure of midwestern United States, *J. Geophys. Res.* 76, 3229-3245.
- Henrici, P. (1964). *Elements of numerical analysis*: Wiley.
- Hildebrand, F. B. (1974). *Introduction to numerical analysis*, McGraw-Hill Press, New York.
- Hron, F. and E. R. Kanasewich (1971). Synthetic seismograms for deep seismic sounding studies using asymptotic ray theory, *Bull. Seism. Soc. Am.* 61, 1169-1200.
- Isaacson, E., and H. B. Keller (1966). *Analysis of numerical methods*: Wiley.
- Kanasewich, E. R. (1983). Cold Lake seismicity project, report no. 3.
- Kapotas, S. S. (1990). Seismic imaging with a parallel MIMD computer, internal report, Department of Physics, University of Alberta.
- Kelamis, P. G., E. R. Kanasewich and F. Abramovici (1983). Attenuation of seismograms obtained by the Cagniard-Pekeris method, *Geophysics* 48, 1204-1211.
- Kennett, B. L. N. (1975). The effects of attenuation on seismograms, *Bull. Seism. Soc. Am.* 65, 1643-1651.

- Kennett, B. L. N. (1983). *Seismic wave propagation in stratified media*, Cambridge University Press, Cambridge.
- Kerner, C. (1990). Modelling of soft sediments and liquid-solid interfaces: modified wavenumber summation method and application, *Geophys. Prosp.* 38, 111-137.
- Kind, R. (1979). Extension of the reflectivity method, *J. Geophys.* 45, 373-380.
- Kind, R. (1985). The reflectivity method for different source and receiver structures and comparison with GRF data, *J. Geophys.* 58, 146-152.
- Knopoff, L. (1964a). A matrix method for elastic wave problems, *Bull. Seism. Soc. Am.* 54, 431-438.
- Knopoff, L. (1964b). "Q", *Rev. Geophys.* 2, 625-660.
- Koefoed, O. (1955). On the effect of Poisson's ratio of rock strata on the reflection coefficients of plane waves, *Geophys. Prosp.* 3, 381-387.
- Krebes, C. G. (1980). *Seismic body waves in anelastic media*, Ph. D. thesis, University of Alberta.
- Kundu, T. and A. K. Mal (1985). Elastic waves in a multilayered solid due to a dislocation source, *Wave Motion* 7, 459-471.
- Lamb, H. (1904). On the propagation of tremors over the surface of an elastic solid, *Phil. Trans. Roy. Soc. Lond.* 203A, 1-42.
- Le, L. H. T., F. Abramovici and E. R. Kanasewich (1990a). Synthetic seismograms for vertically inhomogeneous solids, Abstracts, 18th Internat. Conf. on Math. Geophys., Abstracts, 123.
- Le, L. H. T., F. Abramovici and E. R. Kanasewich (1990b). Synthetic seismograms for vertically inhomogeneous and anelastic media using spectral (w-k) method, 60th Ann. Internat. Mtg., Soc. Expl. Geophys., Expanded Abstracts.
- Lockett, F. J. (1962). The reflection and refraction of waves at an interface between viscoelastic media, *J. Mech. Phys. Solids* 10, 53-64.

- Longman, I. M. (1956). Note on a method for computing infinite integrals of oscillatory functions, *Proc. Camb. Phil. Soc.* 52, 764-768.
- Longman, I. M. (1961). Solution of an integral equation occurring in the study of certain wave-propagation problems in layered media, *J. Acoust. Soc. Am.* 33, 954-958.
- Love, A. E. M. (1944). *A treatise on the mathematical theory of elasticity*, Dover.
- Macrides, C. G. (1987). *Seismic tomography in oil sands for monitoring thermal recovery processes*, Ph. D. thesis, University of Alberta.
- Mallick, S. and L. N. Frazer (1987). Practical aspects of reflectivity modeling, *Geophysics* 52, 1355-1364.
- Mallick, S. and L. N. Frazer (1988). Rapid computation of multioffset vertical seismic profile synthetic seismograms for layered media, *Geophysics* 53, 479-491.
- Mora, P. (1990). *The seismic simulation project*, internal report, Department of Physics, University of Paris.
- Myrias (1989). *SPS - 2/PAMS: system user's manuel*, Myrias Research Corporation.
- Müller, G. (1985). The reflectivity method: a tutorial, *J. Geophys.* 58, 153-174.
- Oliver, J. and M. Major (1960). Leaking modes and the PL phase, *Bull. Seism. Soc. Am.* 50, 165-180.
- O'Neill, M. E. and D. P. Hill (1979). Causal absorption: its effect on synthetic seismograms computed by the reflectivity method, *Bull. Seism. Soc. Am.* 69, 17-25.
- Ostrander, W. J. (1984). Plane-wave reflection coefficients for gas sands at nonnormal angles of incidence, *Geophysics* 49, 1637-1648.
- Outtrim, C. P. and R. G. Evans (1977). Alberta's oil sands reserves and their evaluation, in Redford, D. A. and Winestock, A. G., Eds., *The oil sands of Canada-Venezuela: Can. Inst. Min. Metallurg. Special Vol.* 17, 36-66.
- Panza, G. F. (1985). Synthetic seismograms: the Rayleigh waves modal summation, *J. Geophys.* 58, 125-145.

- Pekeris, C. L. (1940). A pathological case in the numerical solution of integral equations, *Proc. Natl. Acad. Sci. U.S.* 26, 433-437.
- Pekeris, C. L. (1948). Theory of propagation of explosive sound in shallow water, *Geol. Soc. Am., Mem.* 27, 53pp.
- Pekeris, C. L. (1960). Propagation of seismic pulses in layered liquids and solids: in Davids, N., Ed., *Intl. symp. on stress wave propagation in materials*, 45-57.
- Pekeris, C. L., Z. Alterman, F. Abramovici and H. Jarosh, (1965). Propagation of a compressional pulses in a layered solid, *Rev. Geophys.* 3, 25-47.
- Phinney, R. A. (1961). Propagation of leaking interface waves, *Bull. Seism. Soc. Am.* 51, 527-555.
- Phinney, R. A. (1965). Theoretical calculation of the spectrum of first arrivals in layered elastic medium, *J. Geophys. Res.* 70, 5107-5123.
- Phinney, R. A., R. I. Odom and G. J. Fryer (1987). Rapid generation of synthetic seismograms in layered media by vectorization of the algorithm, *Bull. Seism. Soc. Am.* 77, 2218-2226.
- Richards, P. G. (1979). Theoretical seismic wave propagation, *Rev. Geophys. Space Phys.* 17, 312-328.
- Richards, P. G. (1984). On wave fronts and interfaces in anelastic media, *Bull. Seism. Soc. Am.* 74, 2157-2165.
- Rosentbaum, J. H. (1960). The log-time response of a layered elastic medium to explosive sound, *J. Geophys. Res.* 65, 1577-1613.
- Schmidt, H. and G. Tango (1986). Efficient global matrix approach to the computation of synthetic seismograms, *Geophys. J. Roy. Astr. Soc.* 84, 331-359.
- Schwab, F. and L. Knopoff (1970). Surface-wave dispersion computations, *Bull. Seism. Soc. Am.* 60, 321-344.
- Sato, R. (1967). Attenuation of seismic waves, *J. Phys. Earth* 15, 32-61.

- Shanks, E. B. (1966). Solutions of differential equations by evaluations of functions, *Math. Comp.* 20, 21-38.
- Shuey, R. T. (1985). A simplification of the Zoeppritz equations, *Geophysics* 50, 609-614.
- Silva, W. (1976). Body waves in a layered anelastic solid, *Bull. Seism. Soc. Am.* 66, 1539-1554.
- Spencer, T. W. (1960). The method of generalized reflection and transmission coefficients, *Geophysics* 25, 625-641.
- Stephen, R. A. (1977). Synthetic seismograms for the case of the receiver within the reflectivity zone, *Geophys. J. Roy. Astr. Soc.* 51, 169-181.
- Stephen, R. A. and S. T. Bolmer (1985). The direct wave root in marine seismology, *Bull. Seism. Soc. Am.* 75, 57-67.
- Stephen, R. B. and P. Sheng (1985). Acoustic reflections from complex strata, *Geophysics* 50, 1100-1107.
- Takeuchi, H. and M. Saito (1972). Seismic surface waves, in Bolt, B. A., Eds., *Methods in Computational Physics*, Academic Press, Inc.
- Thomson, W.T. (1950). Transmission of elastic waves through a stratified solid, *J. Appl. Phys.* 21, 89-93.
- Tsingas, C. (1989). Seismic reflection imaging over a thermally enhanced oil recovery site, Ph. D. thesis, University of Alberta.
- Vered, M. and A. Ben-Menahem (1974). Application of synthetic seismograms to the study of low-magnitude earthquakes and crustal structure in the norther Red Sea region, *Bull. Seism. Soc. Am.* 64, 1221-1237.
- Wang, C. Y. and R. B. Herrmann (1980). A numerical study of P -, SV -, and SH -wave generation in a plane layered medium, *Bull. Seism. Soc. Am.* 64, 1221-1237.
- Watson, G. N. (1966). *A treatise on the theory of Bessel functions*, Cambridge University

Press, Cambridge.

Xu, P. C. and A. K. Mal (1985). An adaptive integration scheme for irregularly oscillation functions, *Wave Motion* 7, 235-243.